ABSTRACT

Title of dissertation: OPTICAL AND MAGNETIC MEASUREMENTS OF A LEVITATED, GYROSCOPICALLY STABILIZED GRAPHENE NANOPLATELET

Joyce Elizabeth Coppock, Doctor of Philosophy, 2017

Dissertation directed by: Dr. Bruce Kane
Laboratory for Physical Sciences

I discuss the design and operation of a system for levitating a charged, μm-scale, multilayer graphene nanoplatelet in a quadrupole electric field trap in high vacuum. Levitation decouples the platelet from its environment and enables sensitive mechanical and magnetic measurements.

First, I describe a method of generating and trapping the nanoplatelets. The platelets are generated via liquid exfoliation of graphite pellets and charged via electrospray ionization. Individual platelets are trapped at a pressure of several hundred mTorr and transferred to a trap in a second chamber, which is pumped to UHV pressures for further study. All measurements of the trapped platelet's motion are performed via optical scattering.

Second, I present a method of gyroscopically stabilizing the levitated platelet. The rotation frequency of the platelet is locked to an applied radio frequency (rf)

electric field $\boldsymbol{E}_{\mathrm{rf}}$. Over time, frequency-locking stabilizes the platelet so that its axis of rotation is normal to the platelet and perpendicular to $\boldsymbol{E}_{\mathrm{rf}}$.

Finally, I present optical data on the interaction of a multilayer graphene platelet with an applied magnetic field. The stabilized nanoplatelet is extremely sensitive to external torques, and its low-frequency dynamics are determined by an applied magnetic field. Two mechanisms of interaction are observed: a diamagnetic polarizability and a magnetic moment proportional to the frequency of rotation. A model is constructed to describe this data, and experimental values are compared to theory.

OPTICAL AND MAGNETIC MEASUREMENTS OF A LEVITATED, GYROSCOPICALLY STABILIZED GRAPHENE NANOPLATELET

by

Joyce Elizabeth Coppock

Dissertation submitted to the Faculty of the Graduate School of the
University of Maryland, College Park in partial fulfillment
of the requirements for the degree of
Doctor of Philosophy
2017

Advisory Committee:
Professor Frederick Wellstood, Chair
Professor Richard Greene
Dr. Bruce Kane, Advisor
Professor Christopher Lobb
Professor Ichiro Takeuchi

Acknowledgments

The work presented in this thesis would not have been possible without the support and guidance of my advisor, Dr. Bruce Kane, who dreamed up the idea of levitating graphene, demonstrated that it was possible, and patiently guided me through this project. Thanks to his example and advice, I feel that I have matured in my understanding of many aspects of research, including experiment design, apparatus building, and paper writing. I would also like to thank the other students who contributed to the work: graduate student alumnus Pavel Nagornykh, as well as current and former undergraduates Erik Estrada, Caroline Horsch, Saimouli Katragadda, Ian McAdams, and Jacob Murphy.

I would like to thank Prof. Bob Anderson and Dr. Bill Johnson for advising and supporting me from 2011-2014 in research on microwave Hall effect measurements. Although the project I worked on during those years lost funding before I was able to achieve thesis-worthy results, I gained a great deal of valuable experience in experimental research during this time.

The work in this thesis was performed at, and supported by, the Laboratory for Physical Sciences (LPS) in College Park, Maryland. The technicians and engineers in the clean room provided invaluable support and training throughout my time at LPS. They were always ready with a smile, a joke, and expert advice no matter how frustrated I was with my own progress. In addition, the experiment could not have been completed without the precision work of the machine shop staff. I am grateful to the rest of the staff who keep LPS running smoothly, as well as to Margaret

Lukomska for her help with finances and to Jane Hessing and Jessica Crosby for their patience in helping me navigate academic paperwork and deadlines.

I treasure the many friends I made at Maryland. It would be impossible to mention everyone who has brightened my days here, but to make an incomplete list: Barbara Brawn-Cinani, for being a great first-year labmate; Rashmish Mishra, for keeping me company as we pushed through classes; Jack Hellerstedt, Rob Hellauer, and Joffrey Peters for starting a qual study group that spawned lasting friendships; Rufus Phillips, for explaining field theory to me; Anita Roychowdhury, for being a staunch friend and planning the perfect camping trips; Neda Forouzani, for generous encouragement and advice; Quinn Fowler, for chats about writing and life; Rusko Ruskov, for enlightening discussions of physics, and of course all my officemates, for making LPS a welcoming place to work. My multi-talented brother, Keith Coppock, built me a computer, helped me troubleshoot bicycle problems, and kept me supplied with entertaining YouTube videos.

Finally, I am grateful to my mother, Evelyn Spanski, who demonstrated for me and encouraged in me a love of learning throughout my life, and who sacrificed to give me the best education possible. She has been an unbelievably solid rock throughout my time in grad school, even while struggling with her own health problems.

This thesis was written using the LaTex template and style files created by Dorothea Brosius.

Table of Contents

List of Tables

List of Figures

List of Abbreviations

V_{out}	Amplitude of oscillating voltage on outer electrode of trap (V_{peak})
Ω_t	Angular frequency of voltage on outer electrode of trap
$\omega_{x,y,z}$	Eigenfrequencies of motion of trapped particle
V_{dc}	Bias voltage applied to inner electrode of trap (V_{peak})
q	Electric charge on trapped particle
m	Mass of trapped particle
k_B	Boltzmann's constant, *i.e.* 1.38×10^{-23} J K^{-1}
T	The temperature associated with translational motion of the particle
HV	High voltage; refers to voltage on emitter needle
$\mathbf{E}_{\text{rf}}$	Electric field created by applying a radio frequency voltage to the inner trap electrode
E_0	The maximum amplitude of $\mathbf{E}_{\text{rf}}$
ω_0	The angular frequency of the rf electric field
$I_\perp$	The moment of inertia about the axis normal to the surface of a nanoplatelet (*i.e.* the axis of rotation)
$\mathbf{p}$	The electric dipole moment of a nanoplatelet
p_0	The magnitude of $\mathbf{p}$
N_i	The torque on a nanoplatelet about axis i
L_i	The angular momentum of a nanoplatelet about angle i
ω_n	The angular frequency of rotation of a nanoplatelet
ω_ψ	The angular frequency of the in-plane oscillations of a frequency locked nanoplatelet about its minimum energy orientation
Ω	$\equiv p_0 E_0 / (2I_\perp)$
θ	The angle from the vertical of the normal vector to the surface of a spinning nanoplatelet
$\tilde{\boldsymbol{k}}$	The wavevector difference between incident and scattered light
$k_\parallel$	The component of $\tilde{\boldsymbol{k}}$ in the plane of the nanoplatelet
τ_g	A relaxation time associated with the platelet's reorientation after frequency locking
ω_ϕ	The angular frequency of precession of a frequency locked nanoplatelet about $\mathbf{E}_{\text{rf}}$
$\mathbf{B}$	The applied magnetic field
μ	The magnetic moment of the frequency locked nanoplatelet
μ_{dia}	The contribution to μ from diamagnetic effects
μ_{rot}	The contribution to μ from the rotation of the platelet
α_{dia}	A magnetic polarizability arising from diamagnetic effects
α_{rot}	A coefficient relating the rotation frequency of the platelet to μ_{rot}
g	The g-factor of the spinning, frequency locked, charged platelet
Note:	In general, ω is used to represent angular frequency quantities, while ν represents frequencies in Hz.

LPS	Laboratory for Physical Sciences (where this work was performed) 8050 Greenmead Dr., College Park, MD, 20740
AFM	Atomic force microscope
CPL	Circularly polarized light
LPL	Linearly polarized light
FIB	Focused ion beam
NV	Nitrogen vacancy (point defect in diamond)
OTE	Optically transparent electrode
TEM	Transmission electron microscopy
rf	Radio frequency

Chapter 1: Introduction

1.1 Significance of graphene and other 2D materials

Scientists have long been aware of the existence of layered materials. In 1859, the chemist Benjamin Brodie dissolved graphite in strong acids, producing a suspension of extremely thin, flat crystals [1]. It was not until a century later that advances in microscopy allowed the thickness of these flakes to be accurately measured. In 1948, multilayer flakes a few nanometers in thickness were observed via transmission electron microscopy (TEM), and in 1962, atomic monolayers were observed [2]. They are now known to be planar sheets of carbon atoms covered in hydroxyl and epoxide groups and are called graphene oxide crystals.

Remarkably, in 2004, pristine monolayer graphene sheets large enough for transport measurements were isolated using mechanical cleavage, also known as the "Scotch tape method" [3]. The 2004 paper by Novoselov *et. al.* demonstrated several astonishing electronic properties of graphene: an extremely high mobility of 10^5 $\mathrm{cm^2\,V^{-1}\,s^{-1}}$ at room temperature, as well as a strong ambipolar electric field effect, in which the carrier concentration can be tuned from an electron-dominant state, through a few-carrier state, to a hole-dominant state.

Graphene has also been shown to have remarkable mechanical and thermal

properties. It has been shown to have an extremely high breaking strength of around 40 N/m and can reach a strain of 12% before failure [4]. It is flexible in the out-of-plane direction and free-floating sheets of graphene suspended in solution are often observed in folded configurations [5]. Measurements of its room temperature thermal conductivity have varied widely, ranging from 600 $\mathrm{W/m^{-1}\,K^{-1}}$ [6] to 5000 $\mathrm{W/m^{-1}\,K^{-1}}$ [7]. All of these values are fairly high compared to most materials; for example, copper has a room temperature thermal conductivity of 401 $\mathrm{W/m^{-1}\,K^{-1}}$ [8]. In 2015, graphene was theoretically predicted to have a melting temperature of approximately 4510 K, almost 250 K higher than graphite [9].

Graphite is far from the only layered material with the potential to be exfoliated into atomic monolayers. Some discussion of the history of layered materials is given in a review article by Nicolosi (2013) [10]. In 1824, Thomas Webb heated a particular silicate clay similar to mica and found that the material expanded into visibly layered stacks. While the thermally exfoliated material found extensive industrial use, it was not until 1967 that vermiculite clay was exfoliated in liquid and monolayer sheets were observed. In the following years, liquid exfoliation was used to produce monolayers of a few more layered materials, such as TaS_2, NbS_2, and MoS_2 [10]. After the 2004 discovery of the electronic properties of graphene, interest in 2D materials exploded. As discussed in a review article by Butler (2013), methods were developed to exfoliate h-BN, silicene, graphane, and germanane, as well as many transition metal dichalcogenides, copper oxides, and iron pnictides. Methods of sample preparation include mechanical exfoliation, liquid exfoliation, solution-phase crystal growth, epitaxial growth, and chemical vapor deposition [11].

1.2 Motivation for levitated study

Standard experiments on graphene and other 2D materials are performed with the material affixed to a substrate. This is sufficient for most electron transport measurements, although the substrate is known to affect the material properties and must be chosen carefully; for example, graphene mobility has been shown to be limited by scattering from charged impurities in the SiO_2 substrate [12]. Mechanical measurements, however, generally require at least partially isolating the graphene from the substrate. This may be done by etching away part of the substrate to leave the graphene suspended in a doubly-clamped fashion [13] or by depositing mechanically cleaved graphene onto a substrate with holes [4]. Doubly-clamped suspended graphene may be cut using a focused ion beam (FIB) to create a cantilever [14].

The mechanical properties of suspended graphene, such as its elastic modulus and intrinsic strength, may be tested by deforming it with an atomic force microscope (AFM) tip [4]; however, it is difficult to control the intrinsic strain in the suspended graphene. Alternatively, one may treat the suspended graphene as a resonator [13]. Some experiments have cooled graphene resonators until they are near their quantum ground state [15]; however, this requires cooling the entire system using a cryostat or dilution refrigerator. At room temperature, clamping losses make it infeasible to reach the ground state.

1.2.1 Introduction to current work

The goal of this thesis was to study graphene entirely detached from any substrate. This thesis describes an apparatus for levitating and measuring the dynamics of electrically charged μm-scale graphene platelets (and multilayer graphene-like platelets) in an electric field trap. An overview of the experimental apparatus is shown in Fig. 1.1, and a photo is shown in Fig. 1.2. The charge on the surface of the platelets serves two purposes: it enables them to be trapped by electric fields, and it reduces the likelihood of the platelet spontaneously folding or crumpling over on itself. The trap is enclosed in a vacuum chamber in order to further isolate the particle from its environment [16]. The platelet is caused to rotate using circularly polarized light. The rotation can be locked to a radio-frequency (rf) electric field, causing it to precess like a gyroscope. When the platelet is thus stabilized, its dynamics are extremely sensitive to external torques, *e.g.* from magnetic fields. I exploited this sensitivity to test the spinning platelet's response to applied static magnetic fields. I observed two mechanisms of interaction with the applied field: a diamagnetic polarizability and a magnetic moment proportional to the frequency of rotation, which I compared to theoretical predictions.

Many further experiments remain to be performed with this system. The rf locking method allows the rotation frequency of the platelet to be tuned. The current maximum achieved rotation frequency of $\sim$100 MHz can likely be surpassed in future trials. Such high rotation frequencies would be expected to exert enough strain to change the lattice constant significantly. It may be possible to detect

flexural (out-of-plane) phonons, which have been shown to limit graphene's thermal conductivity and intrinsic mobility [17][18].

In addition, there are many possibilities for thermodynamic studies of levitated materials. Since graphene's predicted melting temperature of 4510 K is higher than that of any other known material, there are obvious challenges to experimental confirmation of this prediction. Levitation of graphene platelets in vacuum could provide a good environment for melting-point studies, as graphene's high optical absorption means that it can be heated quickly with a laser.

It may be possible to chemically modify a trapped platelet by injecting gases into the vacuum chamber that then adsorb onto the surface. An alternative would be to expose the platelet to a molecular beam [16]. Similarly, the number of electrical charges attached to the platelet may be modified by bombarding the particle with an electron beam.

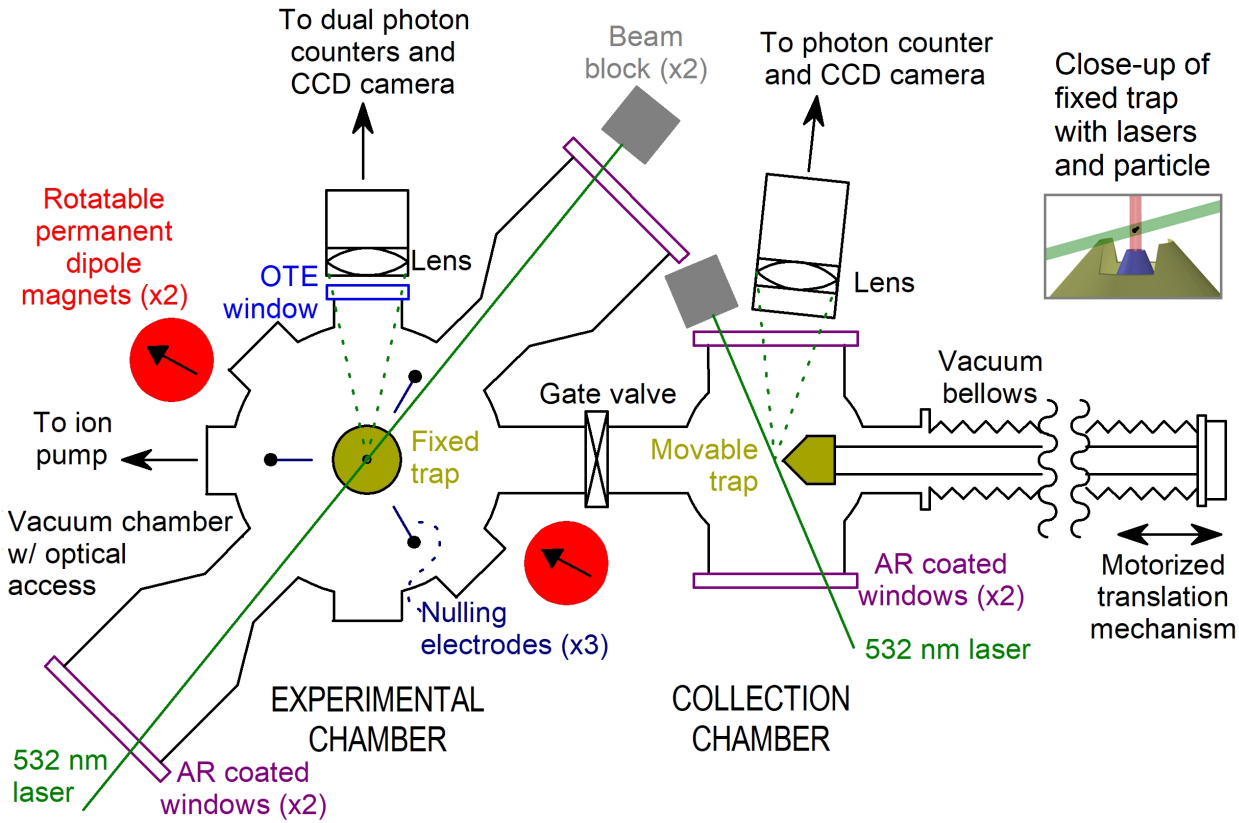

Figure 1.1: Top view of experimental apparatus. Quadrupole traps in vacuum chambers(see Ch. 2) are used to confine graphene nanoplatelets. Particle collection and experimentation are performed in separate chambers to avoid contamination (see Ch. 3,4). Particle is initially collected in a trap mounted on a motorized linear shift mechanism. With gate valve open, moving trap can be brought near fixed trap and particle can be transferred between traps (see Ch. 5).

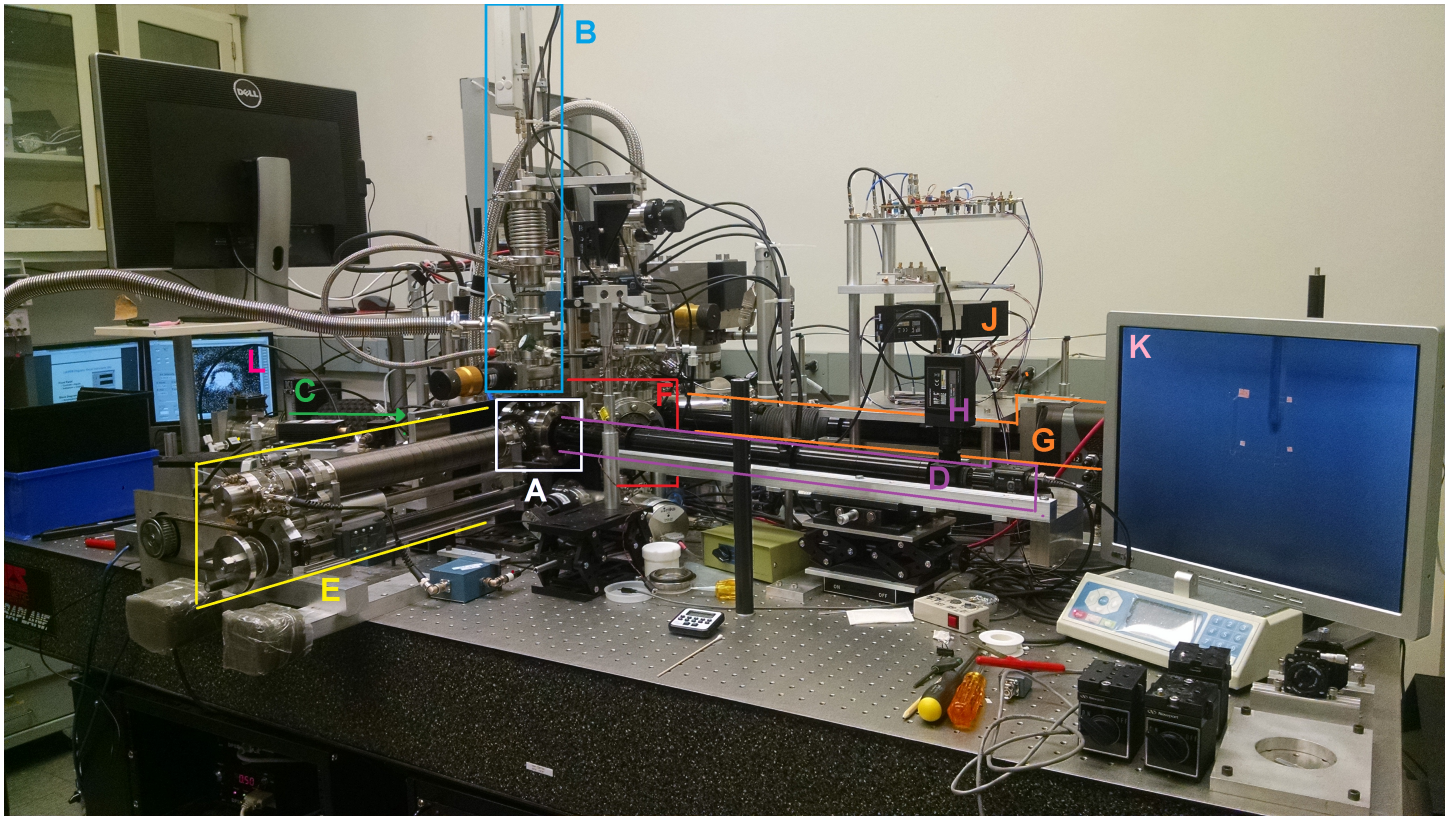

Figure 1.2: Annotated photo of experimental apparatus. (A) Collection chamber. (B) Electrospray apparatus (see Ch. 4), including dual syringe pumps, flexible vacuum bellows, window to view electrospray emitter, roughing pump inlet, and gate valve. (C) Collection chamber laser. (D) Collection chamber optics and CCD camera. (E) Motorized linear shift mechanism for particle transfer (see Ch. 5). (F) Experimental chamber (partially hidden in photo). Note: Experimental chamber laser is at rear of setup and is not visible in this photo.) (G) Experimental chamber optics and CCD camera. (H) Collection chamber photodetector. (J) Experimental chamber prism/photodetector assembly (see Ch. 2). (K) Camera showing electrospray emitter needle (currently idle; see Ch. 4). (L) CCD image showing particle in experimental chamber, illuminated with laser.

1.2.2 Previous work on levitated graphene

My work was built on the original apparatus for levitating graphene nanoplatelets, designed by B. E. Kane and described in a 2010 paper [16]. In this earlier work, it was demonstrated that a charged, μm-scale graphene platelet can be confined in an electric quadrupole trap in high vacuum and caused to rotate at high frequencies using circularly polarized light. The techniques for optical observation of the motion of the trapped platelet as well as for estimation of its mass were originated in this paper.

Numerous additions and upgrades to the system have since been implemented, most notably a method of cooling the translational motion of the trapped platelet using a parametric feedback applied to the trap electrodes. This work was performed by Pavel Nagornykh and is described in his dissertation [19] and Ref. [20].

1.3 Review of experiments on levitated nanoparticles

Optical and electric field traps offer the opportunity to study individual particles that are too small to manipulate by mechanical means. Prior to the beginning of the work in the Kane lab, graphene had not, to my knowledge, been successfully levitated in high vacuum. Levitation of other types of nanoscale and microscale particles, however, has been performed for decades.

The ability to apply highly controlled forces to individual trapped particles often enables tests of fundamental physics. For example, several groups have used trapped particles to test the theory of Brownian motion in various pressure regimes

and at various time scales [21][22][23], and quantum-limited position measurements have been proposed [24]. This section gives an overview of previous experiments on levitated nanoparticles in order to provide background on trapping technologies as well as perspective on experiments to which our graphene system could someday be adapted. Further reviews of experiments on the optomechanics of levitated nanoparticles can be found in Ref. [25].

1.3.1 Nanoparticles in electric field traps

In the 1950s, Wolfgang Paul and colleagues developed a linear quadrupole mass spectrometer, which confined charged particles in two dimensions using rf electric fields [26]. The geometry consisted of four electrodes with hyperbolic cross-sections. Soon after, Paul realized that particles could be confined in three dimensions by modifying the geometry to be cylindrically symmetric, with a ring-shaped electrode with a hyperbolic cross-section and two hyperbolic, rotationally-symmetric "end cap" electrodes [27]. Since then, quadrupole traps have been used to determine the mass and charge of various particles, including polystyrene microcrystals and diamond nanocrystals [28]. Interstellar dust grains have been trapped in order to study their mass, charge, diameter, optical properties, and condensation processes, with the goal of better understanding observations of planetary atmospheres and the interstellar medium [29].

Paul's ring-and-end-cap geometry for the quadrupole trap, although it is able to trap particles stably in three dimensions, has the disadvantage of restricting

access to the trapped particles, which are nearly completely surrounded by electrode material. Various alternative geometries have been proposed. In 2006, Pearson and colleagues succeeded in trapping charged, half-μm-sized particles using a planar trap geometry in which a linear array of particles floated above electrodes printed on a circuit board [30]. In 2009, Maiwald and colleagues developed an ion trap with a "stylus" geometry, in which the particle is confined just above the tip of two concentric cylindrical electrodes, the inner of which protrudes past the tip of the outer. Such a trap has excellent optical access, about 96% of the total 4π solid angle [31]. The conical electrode design of our trap builds on this concept.

1.3.2 Nanoparticles in optical traps

While optical manipulation of graphene has been achieved in liquid [22][32], it has not, to my knowledge, been done in air or vacuum. Optical trapping of graphene in vacuum is likely to be extremely difficult because the high optical absorption of graphene would cause extreme heating under the high laser powers needed for optical trapping. Optical trapping of other types of nanostructures, however, has a long and fruitful history [33], beginning with Ashkin's experiments in which he discovered that a dielectric particle is drawn to the axis of a focused laser beam. Initial experiments trapped particles suspended in a water-filled cell with two counter-propagating laser beams [34]. Ashkin later acheived trapping in high vacuum [35] and showed that a single laser beam, if focused strongly enough, could confine a dielectric particle in three dimensions [36]. Single-beam trapping was achieved in air at atmospheric

pressure by 1997 [37] and has since been performed in ultrahigh vacuum ($\sim 10^{-9}$ Torr) [38].

Since a levitated particle has no physical contact with its environment (aside from collisions with background gas molecules), its translational motion can in principle be cooled far below the temperature of its environment. Several groups have recently attempted to cool levitated nanoscale particles until they are near their quantum ground state. They aim to reach the strong coupling regime, in which the light-matter coupling strength is large compared to losses and quantum behavior can be observed. In one configuration, a particle was trapped in a standing-wave optical trap created by two counter-propagating beams, and its center-of-mass motion was cooled by three orthogonal laser beams, achieving a temperature of 1.5 K [39]. This represents a step toward ground state cooling.

Experiments in the group of Lukas Novotny used a single laser beam to both trap and cool a dielectric nanosphere in ultrahigh vacuum. An active parametric feedback scheme modulates the intensity of the trapping beam, achieving subkelvin cooling [40][41][42]. They used this setup to test fluctuation theorems by observing the relaxation of the particle from a non-equilibrium steady state [43]. The researchers have even observed the recoil of a nanoparticle due to scattering of a single photon [38].

Nanodiamonds are a popular material in vacuum trapping and cooling schemes. One reason is because they can contain nitrogen vacancy (NV) centers, point defects which display photoluminescence and long ground-state spin coherence times, suggesting applications in quantum information [44]. As a first step toward cooling

nanodiamonds in vacuum, they have been optically levitated at atmospheric pressure [45] and in low vacuum (down to 10 Torr) [46]. Additionally, NV centers have been proposed as magnetic field sensors, as the presence of a magnetic field causes Zeeman splitting, which affects the rate of photoluminescence [44]. Geiselmann and colleagues trapped a nanodiamond containing a single NV center in a fluidic chamber. They achieved control over its orientation, allowing them to perform vectorial magnetometry [47].

1.3.3 Nanoparticles in optical cavities

Rather than using a focused laser beam, a levitated nanoparticle may be cooled using an optical cavity [48]. Silicon nanoparticles [49] and nanorods [50] have been levitated in an optical cavity. The nanorods experience optical torque when exposed to elliptically polarized light. Full rotational and translational control of the nanorods opens up possibilities for experiments in rotational cooling and torsional optomechanics [51]. Other recent experiments have combined optical cavities and electric field traps to confine charged nanospheres [52][53][54][55]. It is possible that a graphene nanoplatelet levitated and gyroscopically stabilized by the method described in this thesis could be incorporated into cavity optomechanics experiments [48].

1.3.4 Force detection

Some work on levitated particles has been focused on ultrasensitive force detection. If a levitated nanoparticle is viewed as a mechanical oscillator, then a higher quality factor means a greater sensitivity to external forces. Its quality factor can be increased in two ways: by cooling its center-of-mass motion; and by reducing the damping effects of the surrounding gas by reducing the chamber pressure. Zeptonewton force sensitivities have been achieved by trapping a 300 nm silica sphere in high vacuum (5×10^{-6} Torr). The particle is trapped in a standing-wave optical trap created by two counter-propagating beams, and its center-of-mass motion is cooled by three orthogonal laser beams to temperatures of a few hundred millikelvin to a few kelvin [56].

Hoang and colleagues have proposed a nanoscale torsion balance consisting of a levitated nonspherical nanoparticle. In a linearly polarized beam, the particle's angular orientation is confined and the particle undergoes high-frequency torsional vibrations. These vibrations can be laser-cooled to achieve extreme torque sensitivities [57].

Other experiments have, instead of applying active feedback cooling, harnessed the coupling between rotational and translational degrees of freedom, using rapid rotation of the particle (up to 10 MHz) to effectively cool its translational motion to 40 K [58]. I describe a similar gyroscopic stabilization of our trapped graphene platelets in Ch. 7-9 (although the contribution of the rotation to the translational cooling is not quantitatively measured in the present work).

1.4 Summary of dissertation

This thesis can be roughly divided into two sections. The first half discusses the numerous technical challenges involved in achieving stable trapping at UHV pressures. Chapters 2-4 describe the characteristics and operation of the quadrupole trap, the optical detection system, and the process for preparing suspensions of graphene nanoplatelets and introducing a single platelet to the trap. Ch. 5 describes a method for transferring the trapped platelet between an initial collection trap and a second trap in a clean vacuum chamber for experimentation. Some material in Ch. 2-5 has been published in Ref. [59].

The second half of the thesis describes experiments performed on the platelet once it was successfully trapped at high vacuum and UHV pressures. Chapters 6-7 describe a technique for stabilizing the trapped platelet by causing it to rotate gyroscopically at megahertz frequencies and explore the platelet's dynamics, showing that they they agree with the expected dynamics of a thin, spinning disk. In Ch. 8, the platelet's dimensions are estimated from optical data. Ch. 9 presents data on the response of the platelet to applied magnetic fields. Finally, in Ch. 10, possible future experiments to be performed with the system are discussed. Some material in Ch. 7-9 has been published in Ref. [60].

Chapter 2: Description of trap

2.1 Overview

The experimental apparatus incorporates two traps: a movable trap for initial collection of the particle and a second, fixed trap in which experiments are performed. In this chapter, I focus on the fixed trap; the movable trap is of almost identical design. I describe the principle of the trap, the optics used to observe the motion of the trapped particle, and a method for estimating a trapped particle's mass. Some material in this chapter was published in Ref. [59].

Our trap is similar in principle to the Paul trap [27], which is commonly used for ion trapping but is suitable for trapping charged μm-sized particles as well. A stylus geometry [31] allows two traps to be brought very close together, facilitating the transfer of particles between traps.

A photo and diagram of the trap geometry are shown in Fig. 2.1. The trap consists of two coaxial conical electrodes made of stainless steel. The outer electrode has a radius of 0.8 mm at the tip. The inner electrode has a hole of radius 0.2 mm drilled along its axis to admit a laser beam which can be used to impart angular momentum to the particle. The tip of the inner electrode is recessed by 0.2 mm from the outer electrode tip. A slot of width 1.2 mm is cut across the tip of the outer

electrode in order to break the axial symmetry of the trap. The trap is surrounded by a grounded stainless steel plane and enclosed in a vacuum chamber whose walls are grounded. An oscillating voltage in the frequency range of tens of kHz, with an amplitude of approximately 300 V, is sourced from a waveform generator [61], amplified using an adjustable scaling amplifier [62] and a high voltage amplifier [63], and applied to the outer electrode of the trap.

2.2 Principles of trap operation

If a dc voltage of amplitude V_{out} is applied to the outer electrode, while the inner electrode is held at ground, the electric field $\mathbf{E}$ reaches a zero value at a point $\mathbf{r} = 0$ approximately 0.75 mm from the tip of the outer electrode, along the axis of the trap (see Fig. 2.2). Although $\mathbf{E}$ reaches zero, the electrostatic potential cannot have a local minimum in three dimensions, so a charged particle cannot be trapped in this configuration.

If, however, the potential applied to the outer electrode varies sinusoidally in time, with $V(t) = V_{\text{out}} \cos(\Omega_{\text{t}} t)$, a charged particle experiences a pseudopotential given by [16]:

$$\Psi(\mathbf{r}) = \frac{1}{4} \frac{q}{m} \frac{1}{\Omega_{\text{t}}^2} \mathbf{E}^2(\mathbf{r}), \tag{2.1}$$

where q is the charge on the particle, m is its mass, V_{out} is the amplitude of the voltage applied to the outer electrode, and Ω_{t} is the frequency of the voltage. In the above equation, the damping of the particle's motion due to background gas has been neglected because experiments are generally conducted at low pressures,

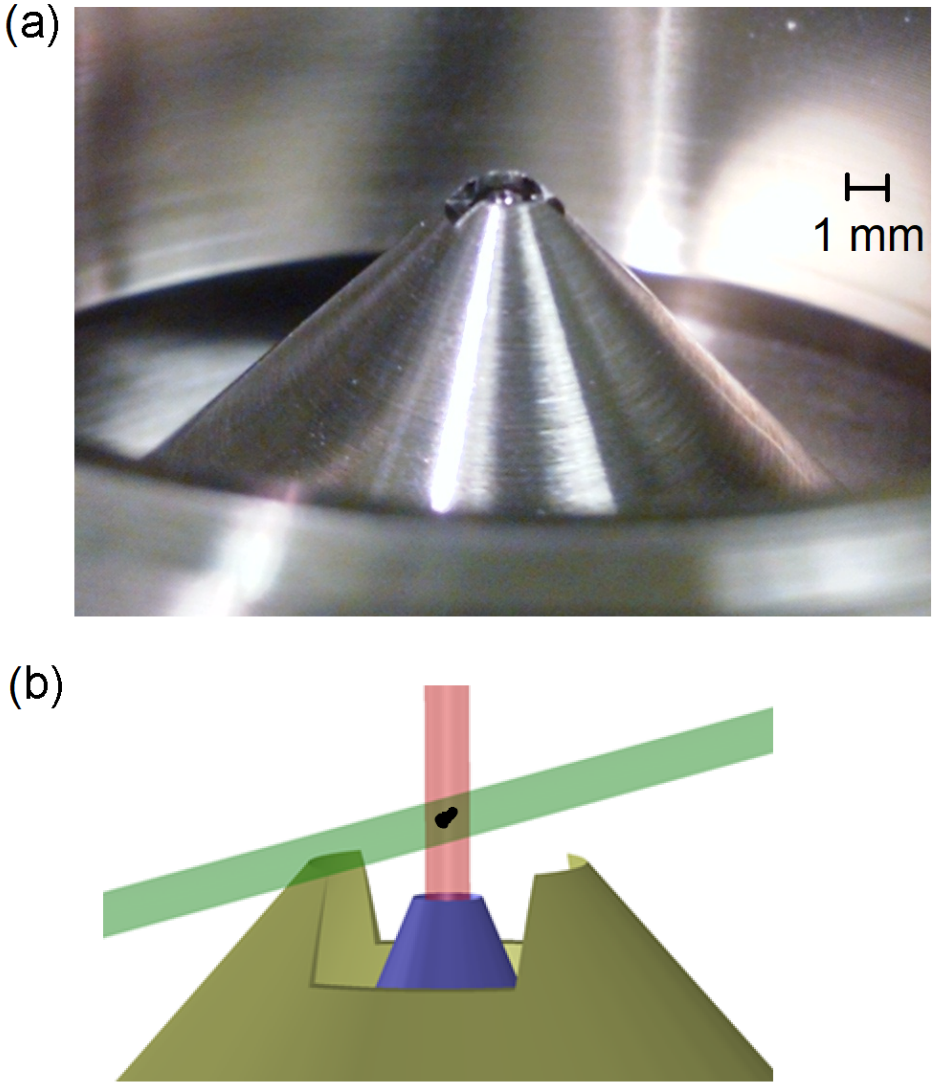

Figure 2.1: (a) Close-up photo of trap, removed from vacuum chamber. Conical electrodes are surrounded by a grounded stainless steel plane. (b) Diagram of tip of electrodes with laser beam and trapped particle. Outer electrode tip diameter: 1.6 mm. Slit width: 1.2 mm. Slit depth: 0.6 mm. Inner electrode tip is recessed 0.2 mm from outer tip. A hole is drilled through the axis of the inner electrode to admit a circularly polarized 671 nm laser beam (red), which may be used to impart angular momentum to the trapped graphene platelet. The platelet is imaged via scattering of a 532 nm laser beam (green), directed horizontally. Platelet (black) is drawn much larger than true scale.

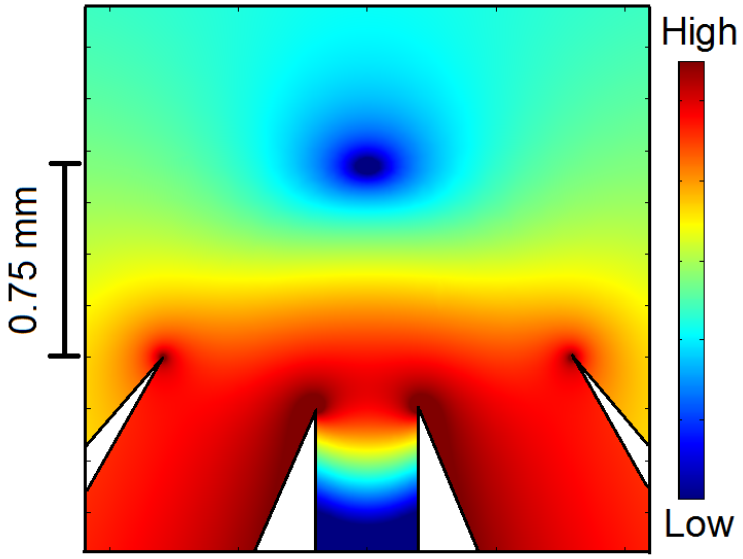

Figure 2.2: False-color cross sectional plot of simulated electric field magnitude $|\mathbf{E}|$ near the conical trap electrodes. Color corresponds to $\log(|\mathbf{E}|)$. A minimum is observed about 0.75 mm from the tip of the trap electrodes. The section plane is vertical and perpendicular to the slot across the tip of the outer electrode.

where the velocity damping rate is several orders of magnitude smaller than Ω_t. As the damping rate becomes comparable to Ω_t, the pseudopotential becomes smaller and the particle is more weakly confined. A color plot of $|\mathbf{E}|$ is shown in Fig. 2.2. The effective potential well is centered at the zero point of the electric field.

Near the point $\mathbf{r} = 0$ where $\mathbf{E}$=0, the electric pseudopotential may be approximated as a quadratic function:

$$\frac{V(x,y,z)}{V_{\text{out}}} = \frac{\alpha_x x^2 + \alpha_y y^2 + \alpha_z z^2}{2z_0^2}, \tag{2.2}$$

The z-axis lies along the axis of the trap electrodes, the x-axis lies perpendicular to the slot in the outer electrode, and the y-axis lies parallel to the slot. z_0 is a parameter that depends on the electrode configuration. In order to illustrate the shape of the trap, I plot the electric potential with the voltage on the outer electrode held constant at V_{out} in Fig. 2.3. Plots of the potential along the cartesian dimensions were obtained via electrostatic simulations (using COMSOL v4.3a). Quadratic fits give $\alpha_x/\alpha_z = 0.32$, $\alpha_y/\alpha_z = 0.60$, $z_0 = 1.7$ mm. The particle is less tightly confined in the direction parallel to the slot.

For small amplitudes of motion, the particle undergoes simple harmonic motion in the well, with characteristic frequencies of oscillation given by [16][20]:

$$\omega_{x,y,z} = |\alpha_{x,y,z}| \frac{1}{\sqrt{2}} \frac{q}{m} \frac{V_{\text{out}}}{\Omega_t z_0^2}, \tag{2.3}$$

The particle will remain trapped only when $\omega_{x,y,z} \ll \Omega_t$. The trap is designed with a slit across its tip to break the cylindrical symmetry, creating three easily distinguished vibrational frequencies. This allows us to resolve the translational

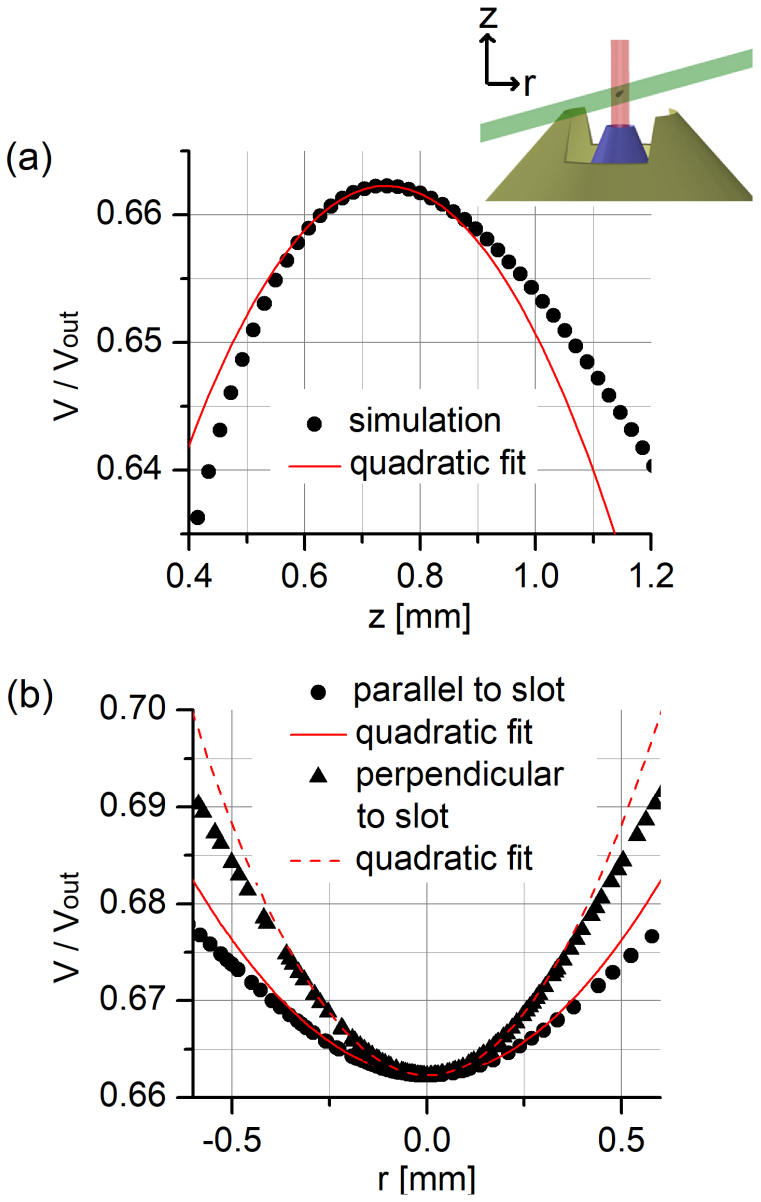

Figure 2.3: Plots of normalized electric potential V/V_{out} with *constant* voltage V_{out} on outer electrode. (During trap operation, trap voltage oscillates, but constant voltage is shown here to illustrate shape of potential near trap minimum.) (a) Plot of V/V_{out} along z-axis (coincident with axis of conical electrodes). Trap center lies at potential maximum, about 0.75 mm from tip of outer electrode. (b) Plot of V/V_{out} along radial axes parallel to slot (circles) and perpendicular to slot (triangles). Lines pass through trap center and lie in plane normal to z-axis.

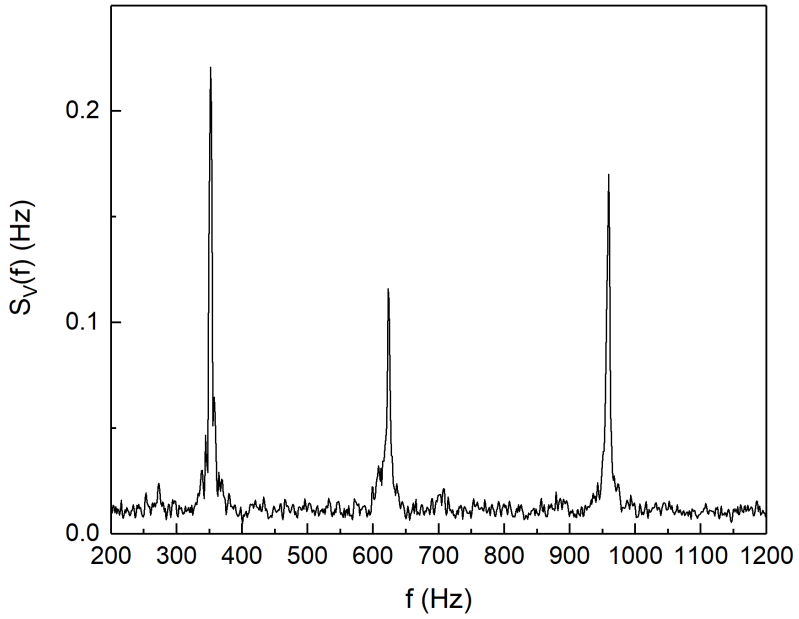

Figure 2.4: Voltage power spectrum $S_v\,(f)$ versus frequency f of the scattered light from a trapped particle. The peaks show the eigenfrequencies of motion in the x, y, and z directions. Chamber pressure is around 30 mTorr; the presence of background gas causes broadening of the peaks. Data taken on October 19, 2016 on sample 101816B.

motion of the particle in three dimensions using scattered light collected in a single lens[20]. A typical spectrum is shown in Fig. 2.4.

As an example, for one recently studied particle, I used a trap frequency of $\nu_{\mathrm{t}} = \Omega_{\mathrm{t}}/\,(2\pi) = 15$ kHz and observed a charge-to-mass ratio of 6.1 C/kg. The eigenfrequencies were $\nu_x = 300$ Hz, $\nu_y = 450$ Hz, and $\nu_z = 750$ Hz, where $\nu_{x,y,z} = \omega_{x,y,z}/\,(2\pi)$. The observed eigenfrequency ratios were $\nu_x/\nu_z = 0.4$ and $\nu_y/\nu_z = 0.6$. The disagreement between the simulated value of 0.32 and the observed value of 0.4 for the x direction may have been due to a small patch field or to a manufacturing

irregularity in the electrodes.

2.3 Vacuum chamber and optics

A view of the experimental chamber is shown in Fig. 2.5. The trap is enclosed in a vacuum chamber of diameter 15 cm. Windows with anti-reflective (AR) coatings permit a laser beam to enter and exit the chamber. Static electrical charge may build up on the insulating windows. To minimize the effects of these charges on the particle, where possible, extra flanges are used to set windows away from the particle. The window through which the scattered light exits could not be recessed due to the focal length of the lens; to minimize charge buildup on this window, it is coated with indium tin oxide (ITO) so that it acts as an optically transparent electrode (OTE).

The particle is detected by means of a vertically polarized 532 nm laser directed horizontally across the chamber. Light scattered from the particle is collected and focused by a lens outside the chamber. A non-polarizing beamsplitter divides the focused light equally (see Fig. 2.6). Half the light goes to a ccd camera [64]. The other half impinges on a knife-edge prism and is directed into dual high-speed photodetectors [65], labeled A and B.

The knife-edge prism is positioned at an angle such that the motion of the particle can be resolved in three dimensions. The sum $A + B$ is used to measure the intensity of the scattered light; the Fourier transform of this signal can be used to measure the rotation frequency of a spinning particle. All data in Ch. 6-9 is

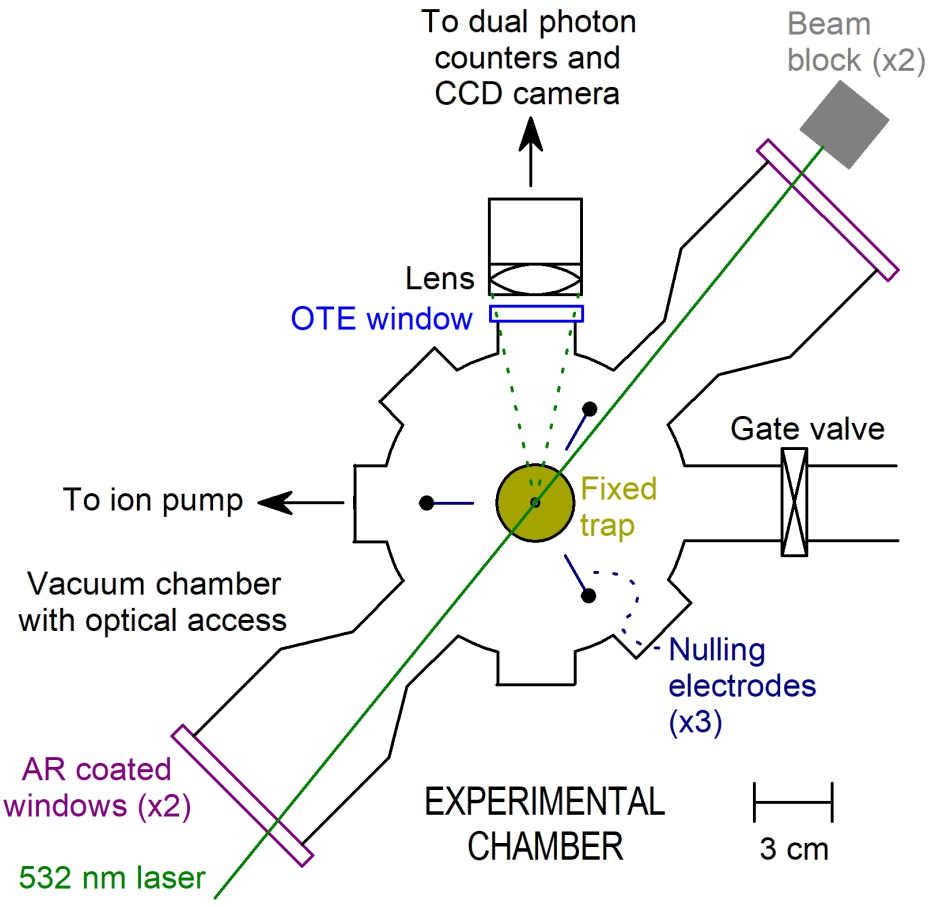

Figure 2.5: Cross-sectional view (from top) of experimental chamber. Approximately to scale.

derived from this optical signal. The normalized difference $(A - B)/(A + B)$ is used to detect the position of the image of the particle with respect to the edge of the prism, so as to track any slow translational drift of the particle. The lens that collects the scattered light is mounted on a 3-axis piezo stage which is continually adjusted by a feedback loop to keep the image of the particle centered on the prism. More information on the particle detection scheme is available in Pavel Nagornykh's dissertation [19].

The laser is mounted on a 3-axis translation stage for precise alignment with the trapped particle. The portion of the beam that is not scattered exits through another window and is collected in an anti-reflective beam dump.

2.4 Parametric feedback cooling method

At chamber pressures in the tens and hundreds of mTorr, the particle's motion is strongly damped by the surrounding gas, and spontaneous escape from the trap is rarely observed; particles have remained in the trap for months. Lower pressures are required, however, for high rotation frequencies and sensitive torque measurements. At $P < 10^{-7}$ Torr, trap lifetimes are much shorter, typically on the order of hours. To address this problem, a feedback cooling method (developed by Pavel Nagornykh [19][20]) was used to stabilize the translational motion of the particle, extending the trap lifetime to weeks.

Stray dc or quasi-static electric fields may develop in the vicinity of the trap [66][67]. They may arise from buildup of charged material on the electrodes or walls

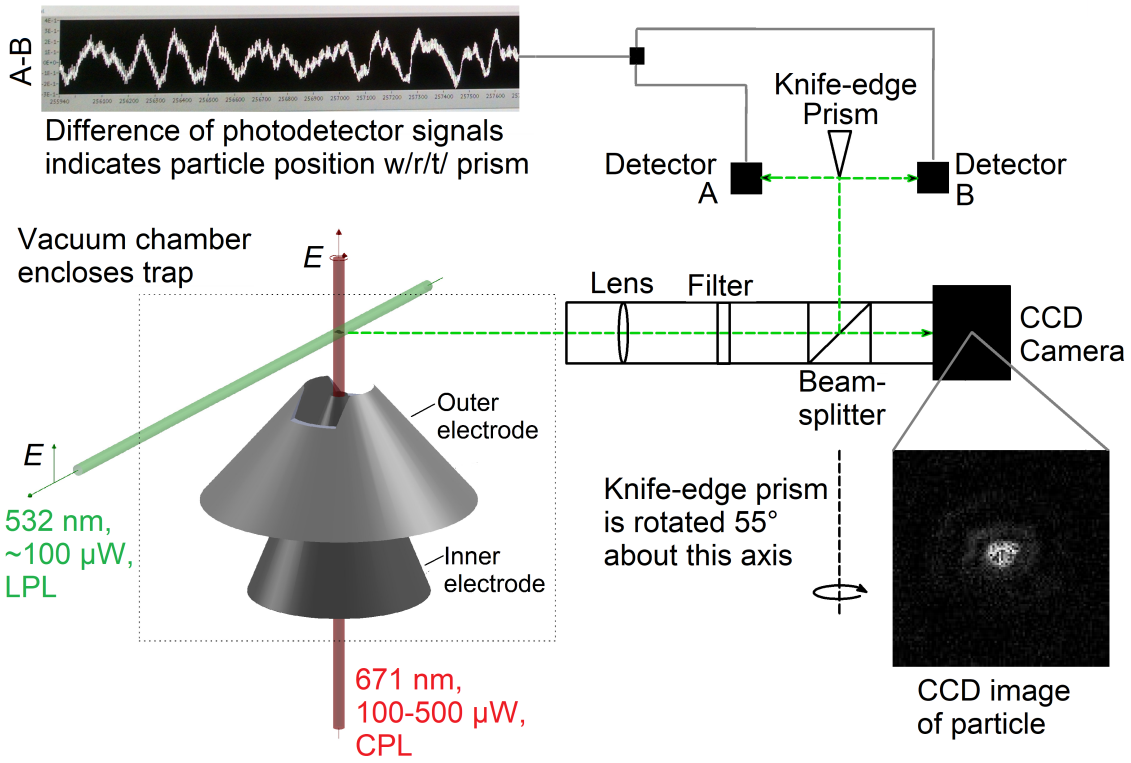

Figure 2.6: Diagram of trap and optics in experimental chamber (not to scale). Linearly polarized laser light at 532 nm is scattered from a trapped particle and collected in a lens. Collected light passes through a green-pass filter and a (non-polarizing) beamsplitter. Half the light goes to a CCD camera for visualization of the particle. The other half of the light impinges on a knife-edge prism which is rotated at an angle that allows resolution of particle motion in three dimensions. The difference of the photodetector signals (A-B) is used to detect the position of the image of the particle with respect to the edge of the prism. A piezo stage, controlled by a feedback loop, is used to adjust the lens position to keep the image of the particle centered on the prism. The sum (A+B) gives the total intensity of collected light and is used for most data (see Ch. 6-9). If desired, circularly polarized laser light may be directed through a hole in the trap axis to impart angular momentum to the particle.

of the vacuum chamber. The presence of such fields enhances the coupling of noise to the feedback cooling signal, limiting the achievable cooling efficiency [20]. In order to null the effects of stray fields, we apply dc voltages of up to 15 V on each of three nulling electrodes surrounding the trap (see Fig. 2.5). Details on the process of finding the optimal nulling voltages can be found in Pavel Nagornykh's thesis [19].

2.5 Measurement of particle mass

The particle undergoes Brownian motion in the trap [21][22]. The equipartition theorem can be written for motion in the z-direction as:

$$\frac{1}{2}k_B T = \frac{1}{2}m\omega_z^2\langle z^2\rangle, \tag{2.4}$$

where k_B is Boltzmann's constant, T is the temperature of the particle, and m is the particle's mass. The platelet's frequency of oscillation in the vertical direction, ω_z, can be measured from the frequency spectrum of the light scattered from the particle (see Fig. 2.4). Here $\langle z^2\rangle$ is the mean-square amplitude of the particle's motion, which can be estimated from the size of the particle's image on the CCD camera (the pixel size is approximately 2.7 μm). The value of $\langle z^2\rangle$ was calculated by fitting the intensity profile (along the vertical direction) of the particle's CCD image to a Gaussian function.

With the chamber pressure relatively high (around 30 mTorr), we may assume that the particle's motion is thermalized and T = 300 K. We keep the laser power low (around 100 μW) to avoid heating the particle significantly above room temperature.

To improve the precision of the measurement, I recorded data at several values of V_{out} (*i.e.*, several different trap stiffnesses) and fit a line to the resulting plot of ω_z^{-2} versus $\langle z^2 \rangle$ (see Fig. 2.7(a)). The slope of this line can be used to find the mass m.

As a check on this measurement, I also used the horizontal motion of the particle to estimate the mass. Since the plane of the CCD camera is oriented at an angle between the x and y axes, the particle's image shows a combination of its x and y motion. One can rewrite the equipartition theorem for horizontal motion as follows:

$$\frac{1}{2} k_B T = \frac{1}{2} m \omega_h^2 \langle h^2 \rangle, \tag{2.5}$$

where $\langle h^2 \rangle$ is calculated by fitting the intensity profile of the particle's CCD image along the *horizontal* direction, and the frequency of oscillation ω_h is a combination of the x and y eigenfrequencies, ω_x and ω_y:

$$\frac{1}{\omega_h^2} = \frac{(\sin 38^\circ)^2}{\omega_x^2} + \frac{(\cos 38^\circ)^2}{\omega_y^2}, \tag{2.6}$$

where the sine and cosine factors appear because the normal vector to the CCD camera plane is at an angle of 38° to the x-axis.

Figure 2.7 shows plots of ω_z^{-2} versus $\langle z^2 \rangle$ and ω_h^{-2} versus $\langle h^2 \rangle$ for the particle examined in Ch. 9.6. This data yielded a mass of $m \approx 3.7 \times 10^{-17}$ kg. For this particle, mass data from the vertical and horizontal motion differed by only 1.5%; however, for other particles, masses from the vertical and horizontal data have differed by up to 20%. The method has considerable uncertainty due to the imprecision in the measurement of the amplitude of motion.

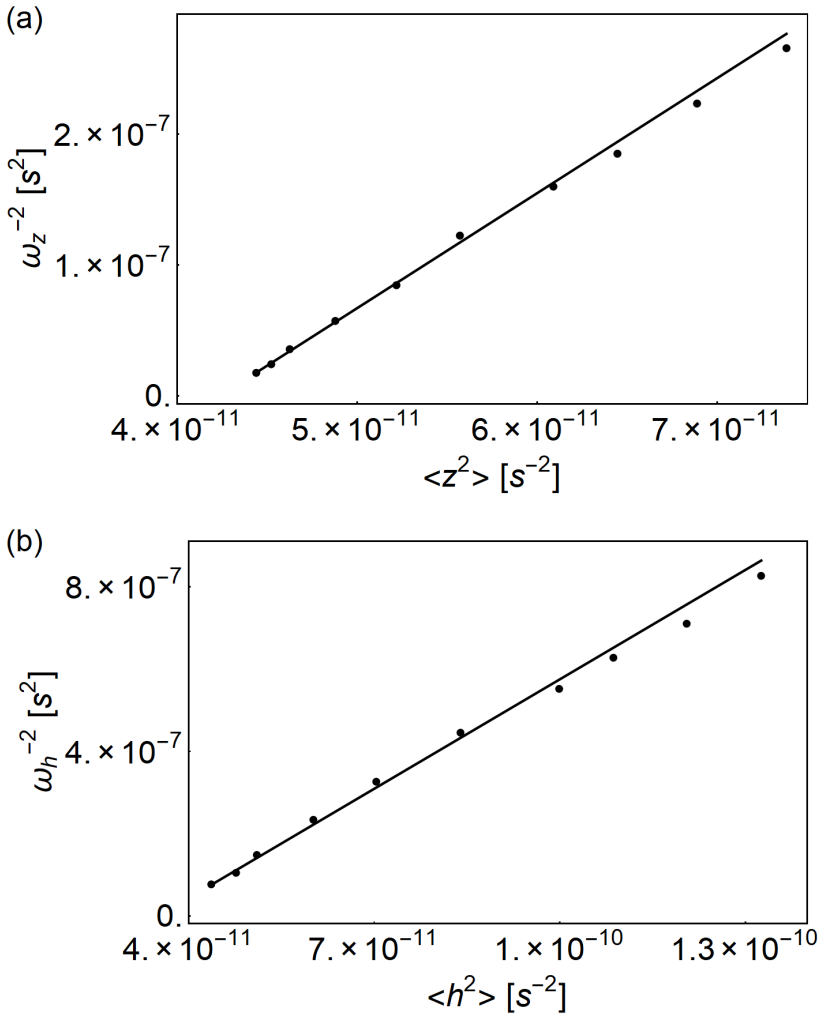

Figure 2.7: Data used to determine the mass of the trapped particle. From Eqs. 2.4-2.5, the slope of these plots are equal to m/k_BT, where m is the mass of the particle, k_B is Boltzmann's constant, and T is the temperature of the particle. (a) The vertical motion of the particle is analyzed, giving a mass of $m = 3.73 \times 10^{-17}$ kg. (b) The horizontal motion is analyzed, giving a mass of $m = 3.68 \times 10^{-17}$ kg. Data was taken Oct. 19, 2016 on sample 101816B.

2.5.1 Alternate method of mass measurement

Another method of measuring the mass (which was not used in this thesis) is described in the dissertation of Pavel Nagornykh [19]. Particles typically discharge over time, and their oscillation frequencies consequently change along with their net charge. By observing discrete steps in the oscillation frequency, one can pinpoint times at which a single electronic charge was lost or gained, and thus infer the mass of the particle [68]. The difficulty of this method lies in observing enough discharge events to conclude definitively which of the steps correspond to a change of a single electronic charge.

Chapter 3: Preparation of graphene nanoplatelets

3.1 Overview

For successful experiments on trapped graphene, it is necessary to have a reliable, relatively quick method of generating samples. This is especially important because the method of delivering the samples to the trap, which will be discussed in Ch. 4, involves a high rate of attrition: a suspension of platelets in liquid is sprayed toward the trap and a small fraction of platelets fall into the well. In this chapter, I describe the method I used to generate graphene nanoplatelet suspensions. Some material in this chapter was published in Ref. [59].

3.2 Liquid exfoliation

The graphene platelets used in these experiments were generated by liquid exfoliation, a process in which bulk layered materials are sonicated in a solvent to cause the layers to separate. Liquid exfoliation has been performed on a large variety of layered materials [10], any of which could in principle be studied in this system. While some research has found that the addition of a surfactant produces suspensions of higher concentration and greater stability [69][70], I avoided the use

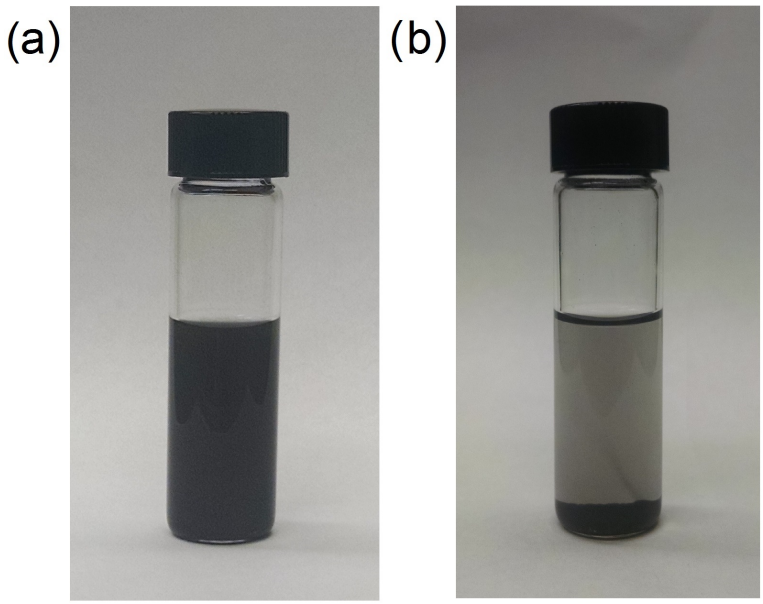

Figure 3.1: Graphene suspension in isopropyl alcohol water mixture. (a) After sonication. (b) After centrifugation.

of any additives because they may leave residue on the platelets after evaporation.

3.3 Method for exfoliation of graphite pellets

To begin the exfoliation process, 5 mg of graphite pellets were placed in a glass vial with 5 mL of a solution of 3 parts LC/MS grade isopropyl alcohol to 1 part deionized water. The vial has a volume of 8 mL and its cap is lined with polytetrafluoroethylene (PTFE). To minimize the introduction of contaminants, the graphite pellets were weighed in a covered balance and the steps involving liquids were performed in the LPS cleanroom. The mixture was sonicated in a bath sonicator for 30 minutes, resulting in a dark liquid containing particles of varying thicknesses, including some unexfoliated graphite chunks (see Fig. 3.1(a)). This liquid was cen-

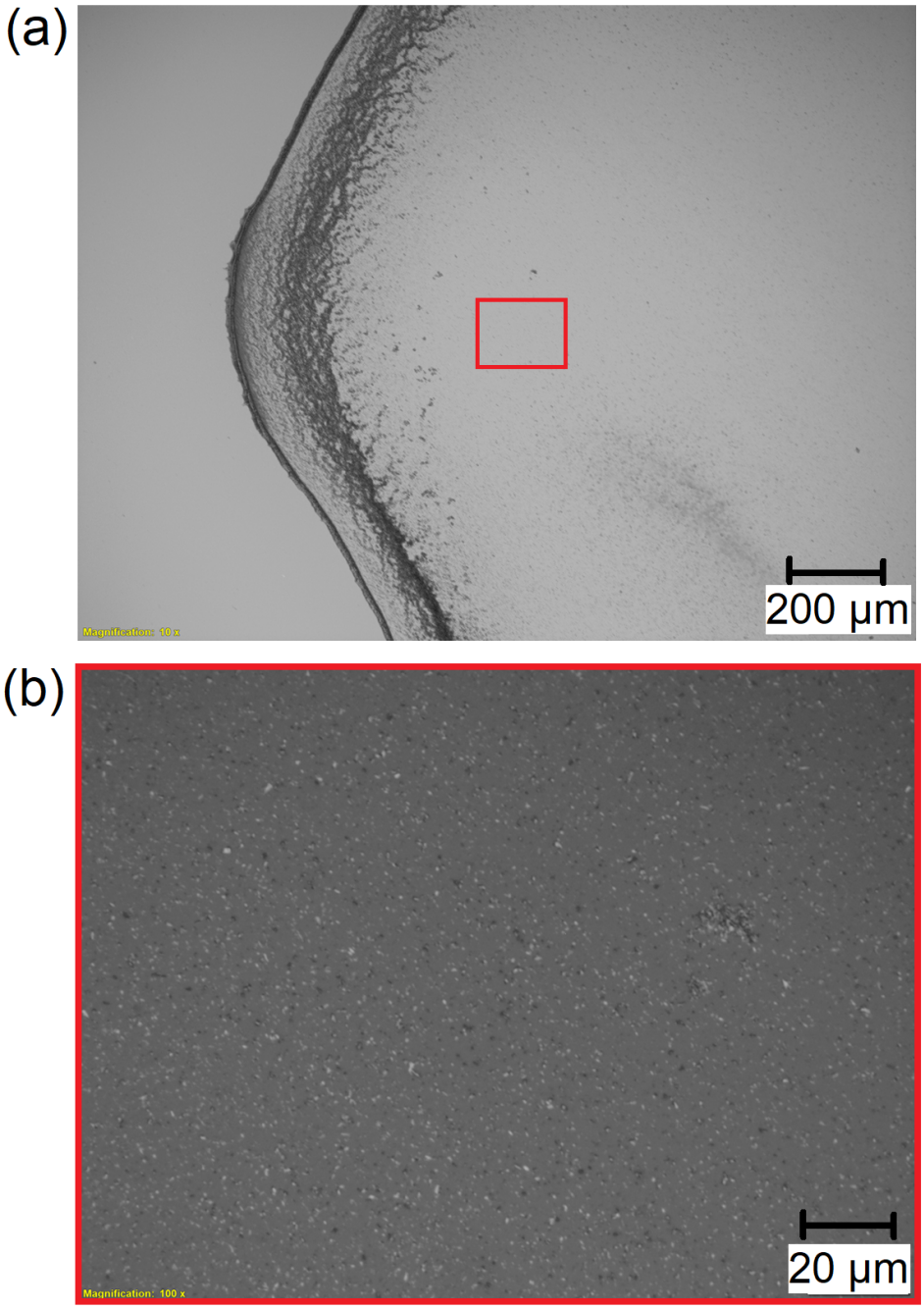

Figure 3.2: (a) Drop of graphene suspension on slide, examined at 10x. (b) Drop at 100x magnification using dark field illumination. Individual particles are visible.

trifuged at an acceleration of $880g$ for 30 minutes to bring the thickest particles to the bottom of the vial. The resulting suspension was shown in Fig. 3.1(b). Images of a drop of solution examined under a light microscope are shown in Fig. 3.2.

I characterized the initial suspension density and rate of settling by measuring the attenuation of a 532 nm laser beam directed through the middle of the vial. The average attenuation coefficient immediately after preparation was 138 m^{-1}, with a standard deviation of 33 m^{-1}. Hernandez [71] finds the relationship between concentration and attenuation for exfoliated graphene to be 2500 $\mathrm{L\,g^{-1}\,m^{-1}}$, which suggests that our suspensions have a concentration of 60 $\mathrm{mg\,L^{-1}}$. Hernandez' result was obtained for suspensions in the range of 1-8 $\mathrm{mg\,L^{-1}}$, while another paper [69] cites a coefficient of 6600 $\mathrm{L\,g^{-1}\,m^{-1}}$ for suspensions in the range of 25-200 $\mathrm{mg\,L^{-1}}$. Thus, our concentration may be slightly overestimated.

The suspensions settle over time, with the attenuation coefficient dropping approximately exponentially. The time constant of this settling is on the order of years and increases for suspensions created with fresher alcohol/water solutions, as shown in Fig. 3.3.

This process produces a suspension of flakes of varying diameter and thickness. Green and Hersam [72] have sorted exfoliated graphene flakes by thickness using density gradient ultracentrifugation. This method results in a fractionated dispersion, with one fraction containing around 80% single-layer graphene. I did not use their technique because it relies on the use of a surfactant and an additional dense solute.

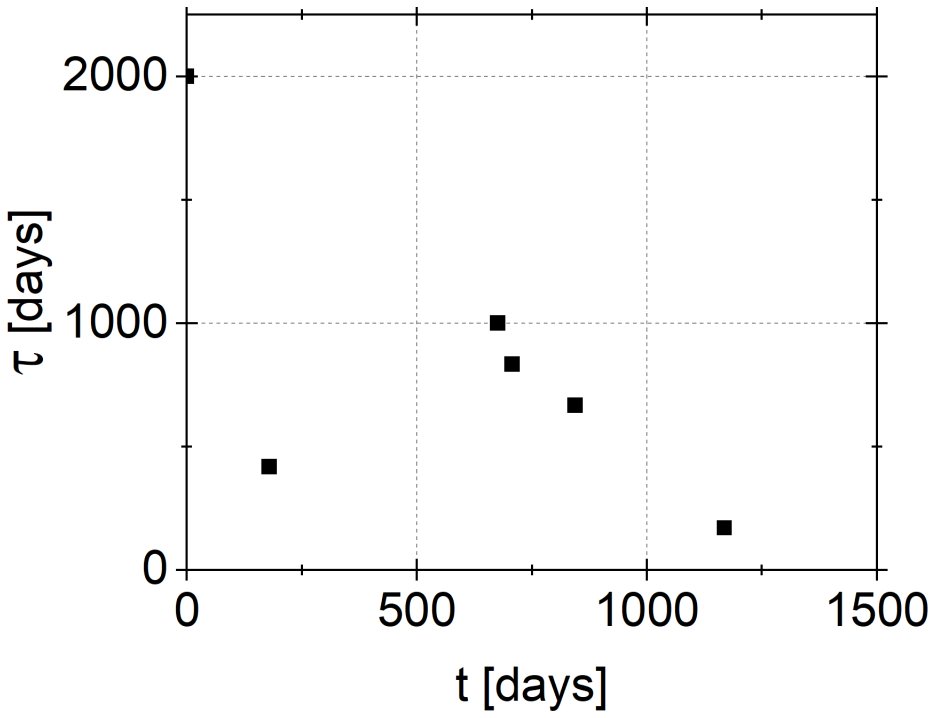

Figure 3.3: Settling times τ of sonicated graphite suspensions plotted versus the age t of the 3:1 alcohol solution at the time of sonication. There is a very rough trend in which suspensions made with fresher alcohol/water solutions last longer.

3.4 Attempts at suspending commercially-produced nanoplatelets

The ideal particle for the trapping experiments described in this thesis has a large area and few layers. I tried preparing suspensions of commercially-manufactured graphene nanoplatelets in the hope that they would provide larger, thinner particles than sonicated graphite pellets, but my attempts were not successful. I used two types of nanoplatelets: one had a nominal diameter of 5-7 μm, with 2-12 nm thickness [73]; the other had a nominal diameter of 1-2 μm, with claimed friability to < 4 layers [74]. We prepared solutions with varying initial masses of nanoplatelets, from 5-15 mg in 5 mL alcohol/water solution and sonicated the mixture for times varying from 30-90 minutes. All of the resulting suspensions were much less stable than those made by sonicating graphite pellets. Comparable levels of attenuation were reached after only about 10 minutes of centrifugation, rather than the usual 30 minutes. Post-centrifugation, the suspensions continued to settle at faster rates, with time constants of 200-300 days even when the suspension was prepared with a fresh alcohol/water solution. I was unable to trap platelets suitable for experiments using these suspensions; the experiments described in Ch. 5-9 were done using platelets prepared by sonicating graphite pellets, as described in Sec. 3.2-3.3. Although the details of manufacture for these nanoplatelets are proprietary, they are stated to contain up to 1% additives, which may affect the stability of the suspensions. As graphene grows in popularity for industrial applications, it is to be hoped that manufactured platelets without additives will become available for fundamental studies.

Chapter 4: Capture of graphene nanoplatelets

4.1 Overview

The next step in the process is to trap an individual platelet. In this chapter, I will describe the process used to deliver platelets from the liquid suspension to the movable trap. Some material in this chapter was published in Ref. [59].

I used the electrospray ionization technique [75][76][77] to charge the platelets and propel them toward the trap. Graphene has a significant probablity of folding when exposed to heat or mechanical forces [5][78]. Applying charge to the surface not only allows a platelet to be trapped, but also provides the additional advantage of reducing the likelihood of folding or crumpling.

4.2 Apparatus and procedure

The relevant section of the apparatus is shown in Fig. 4.1. Photos of the setup are shown in Fig. 4.3. The reader may also refer to Fig. 1.2 (parts A, B, K) to see the collection system in relation to the overall apparatus. The configuration is similar to that used by Cai *et. al.* [28] to inject charged particles into a quadrupole mass spectrometer. Graphene suspension is drawn from the preparation vial using a 22

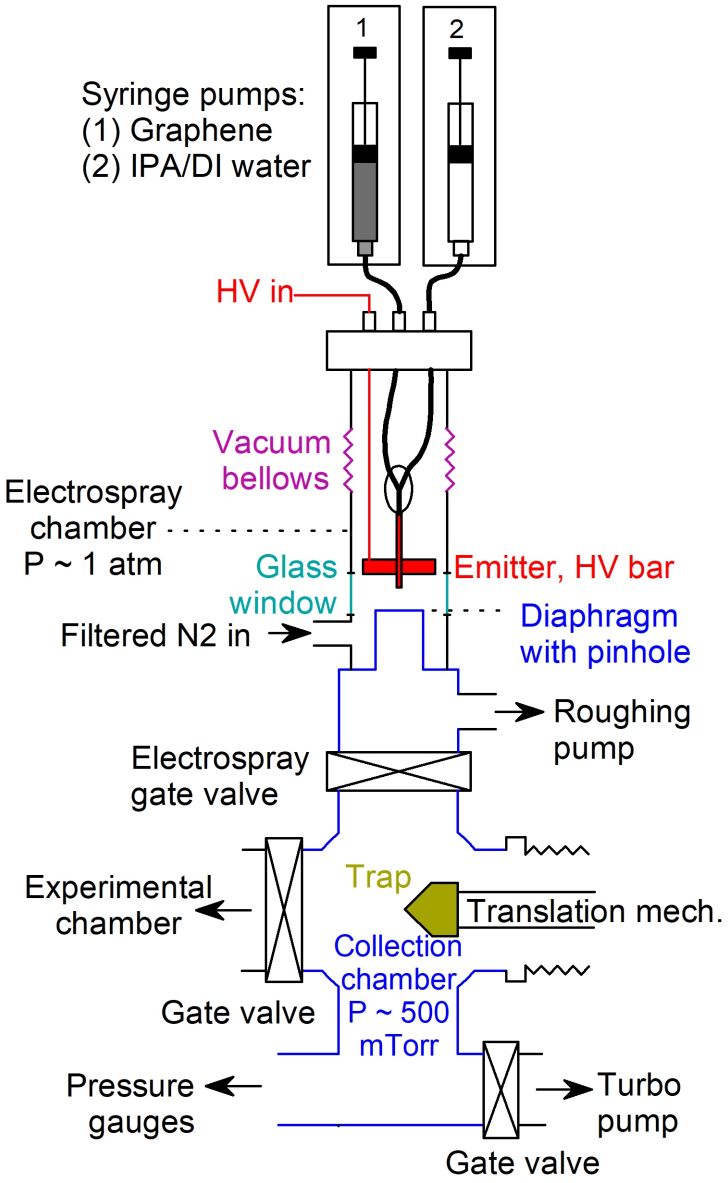

Figure 4.1: Side view of particle collection chamber. Drawing is not to scale. Syringe pumps are mounted on posts above the electrospray chamber. The HV bar and emitter are suspended within the electrospray chamber on insulating plastic posts. The electrospray chamber contains a section of exible vacuum bellows, which allows the emitter to be positioned precisely over the pinhole. The top section of the chamber is positioned using a 3-axis translation stage, while the remainder of the apparatus is fixed to the table.

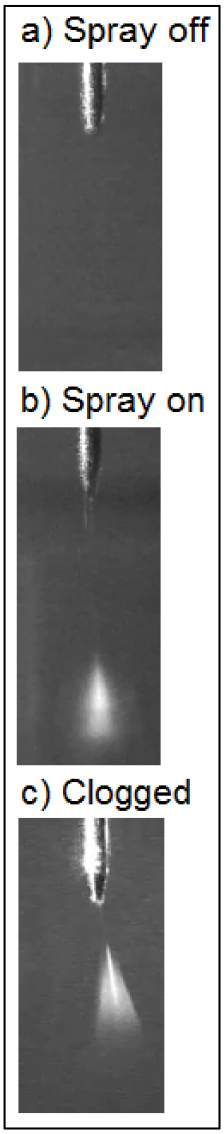

Figure 4.2: Close-up photos of the emitter needle illuminated with a laser pointer with the electrospray (a) off, (b) on, showing an ideal symmetrical cone, and (c) on, showing a skewed cone resulting from a partially clogged emitter.

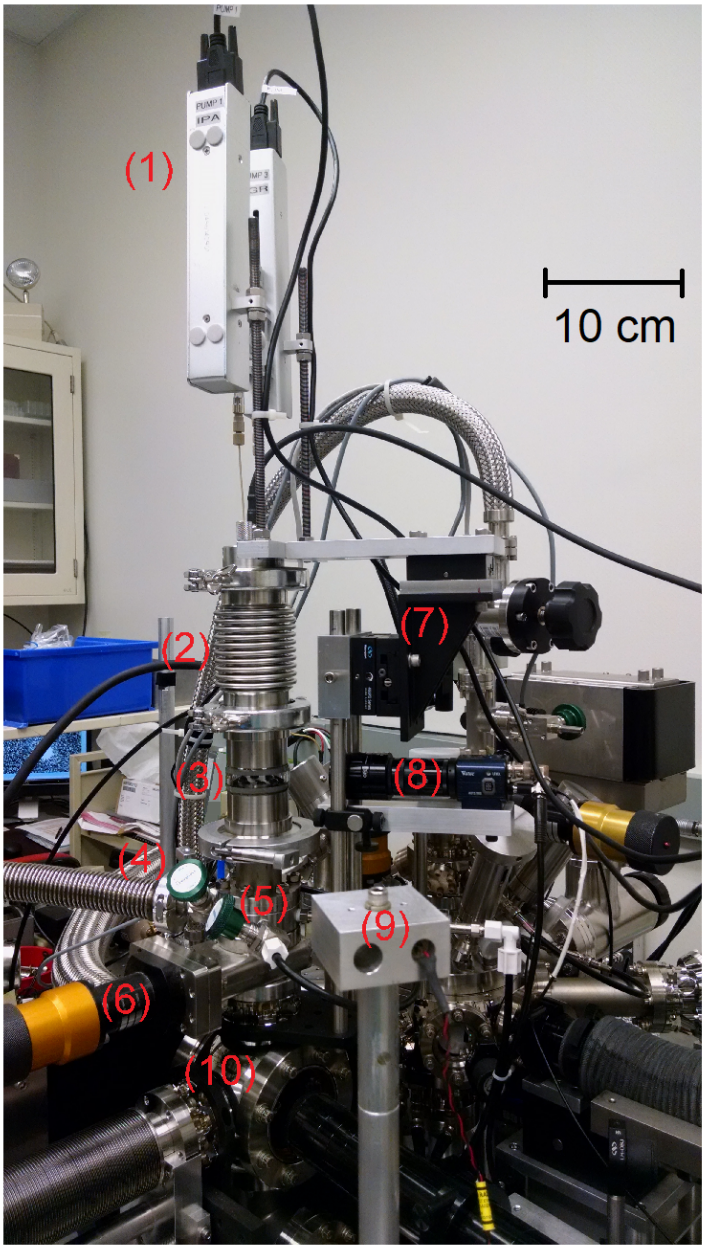

Figure 4.3: Photo showing outside of particle collection apparatus. Components are numbered in red, as follows: (1) Dual syringe pumps. (2) Flexible vacuum bellows. (3) Glass window for viewing electrospray chamber. (4) Roughing pump inlet valve (green). (5) Nitrogen gas inlet valve (green). (6) Gate valve separating electrospray chamber and collection chamber. (7) 3-axis stage for positioning of emitter needle with respect to pinhole. (8) Camera for viewing electrospray emission. (9) Small laser for illuminating electrospray cone through window. (10) Collection chamber.

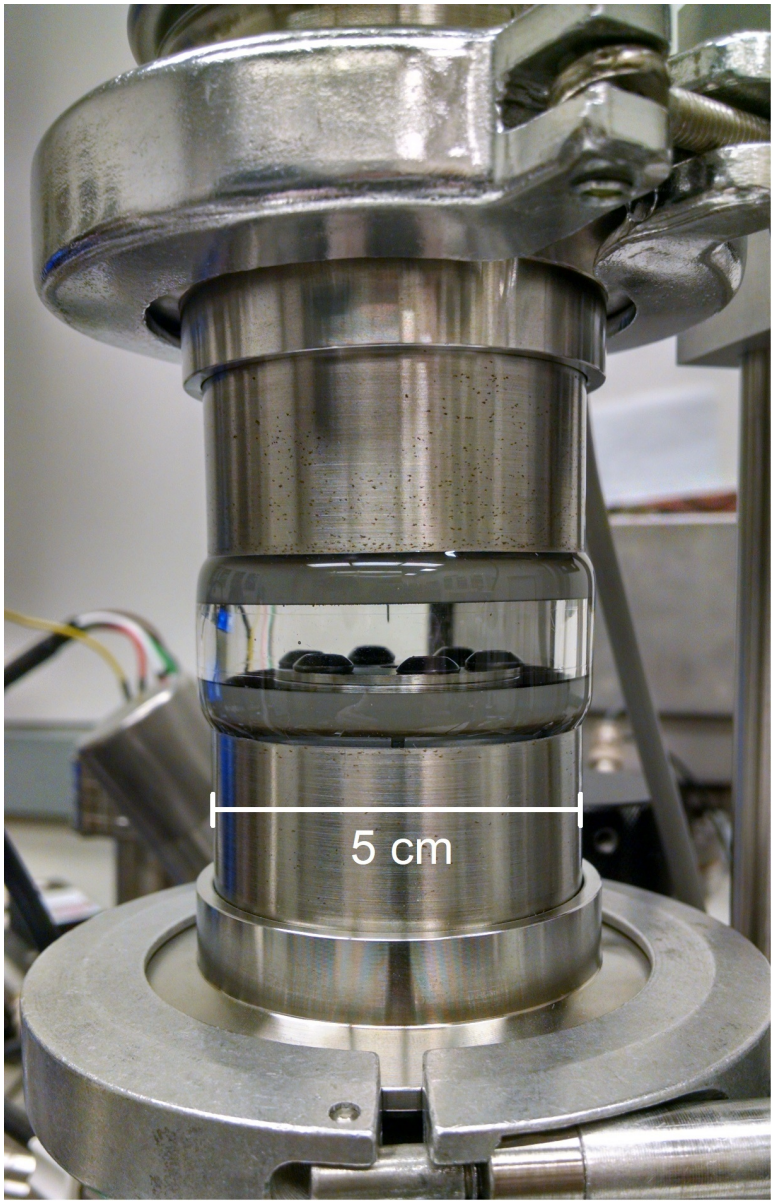

Figure 4.4: Close-up of electrospray viewing window, showing emitter at top of window (currently idle). Pinhole flange is barely visible at bottom of window.

gauge stainless steel needle on the end of a 500 μL syringe. Liquid is injected from the syringe into the system using a dual syringe pump system [79]. One pump holds the syringe of graphene suspension, while the other holds a syringe of pure alcohol/water solution. The alcohol/water syringe pump is used for cleaning purposes only; during normal particle collection, only the graphene suspension is pumped in. Tubing made of PEEK (polyether ether ketone, a polymer with good chemical resistance), with an inner diameter of 0.5 mm, is used to carry fluid from each syringe down into a cylindrical chamber (the "electrospray chamber" in Fig. 4.1). Within the chamber, the tubes empty into a 3-way fitting that directs the liquid flow into a stainless steel needle of inner diameter 100 μm and length 3.5 cm [80].

The emitter needle tip sits about 5 mm above a vacuum chamber (the "collection chamber" in Fig. 4.1) whose opening is covered by a stainless steel diaphragm with a 75 μm diameter pinhole [81]. The electrospray chamber column is made with a section of flexible vacuum bellows to allow the emitter needle to be precisely positioned with respect to the pinhole. The movable upper portion of the column is positioned with a 3-axis translation stage. The fixed portion of the column contains a glass window to allow viewing of the electrospray cone. A small laser is directed horizontally through the window to illuminate the cone, and a small camera is positioned outside the window to provide a close-up view on a nearby monitor (see Fig. 1.2).

The electrospray chamber is kept near atmospheric pressure and constantly purged with N_2 gas, while the collection chamber is evacuated by a roughing pump. The pressure in the collection chamber depends approximately linearly on the di-

ameter of the pinhole, as well as on the pumping rate, and for our system is approximately 540 mTorr for a clean 75 μm pinhole. The emitter needle is held at a voltage of several kV, while the diaphragm is grounded. A positive emitter voltage results in positively charged platelets, while a negative emitter voltage produces negatively charged platelets. The emitter passes through a metal bar with a hole just large enough for clearance; this serves both to keep the emitter vertical and make electrical contact via a wire soldered to the bar. Voltage is sourced from a high voltage power supply [82].

For liquid flow rates greater than 0.5 μL min^{-1} and emitter voltages of 2100-3000 V, the liquid exits the emitter in a cone of charged microdroplets, some of which contain charged graphene platelets. This cone can be seen with the naked eye when illuminated with a laser pointer through the glass wall of the electrospray chamber. Images of the emitter tip when idle and spraying are shown in Fig. 4.4(a,b).

The collection chamber holds a movable trap mounted with its axis horizontal. This trap is identical to the one described in Sec. 2, except that it is axially symmetric, lacking the slit cut across the outer electrode. It also lacks the hole through the axis of the inner electrode. Its tip is positioned below the pinhole. A gate valve (the "electrospray gate valve") lies between the roughing pump inlet and the trap, so that the lower part of the collection chamber can be closed off and evacuated with a turbo pump. When the gate valve is open, particles can continue their trajectory into the vicinity of the potential well.

I used the following set of system parameters to capture positively charged particles from a suspension prepared as described in Sec. 3 for the experiments

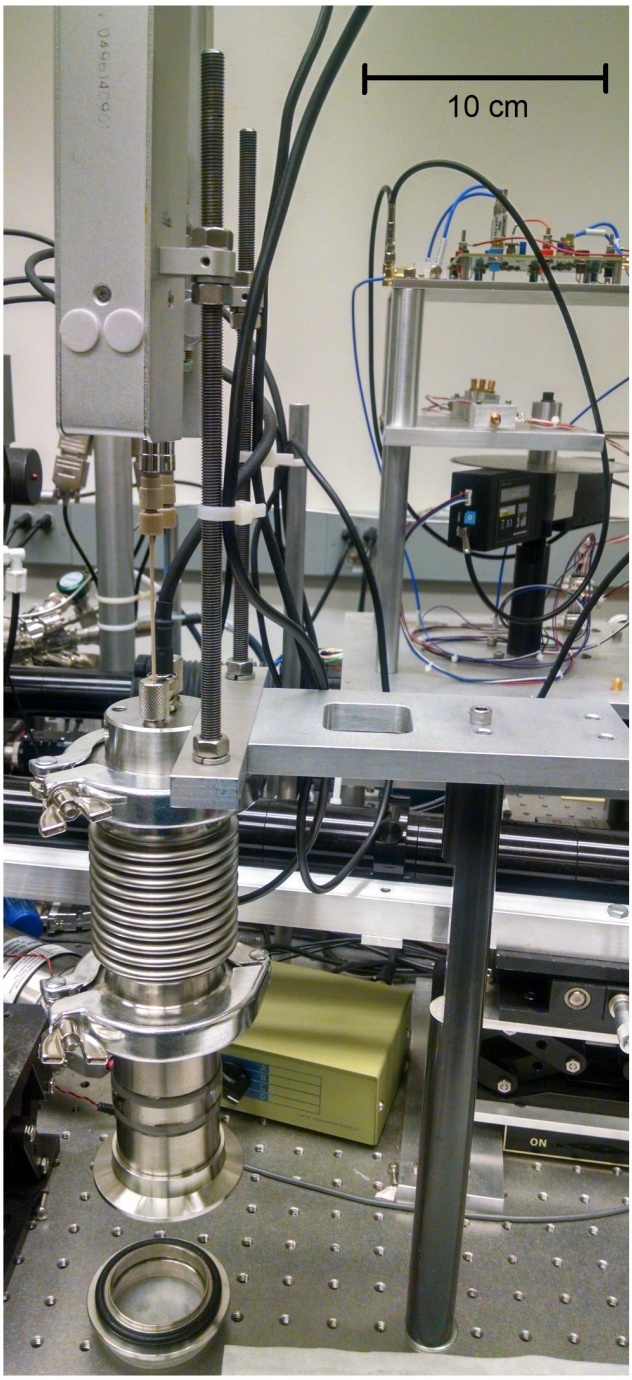

Figure 4.5: (a) The emitter assembly can be removed from the system and mounted on a post for maintenance.

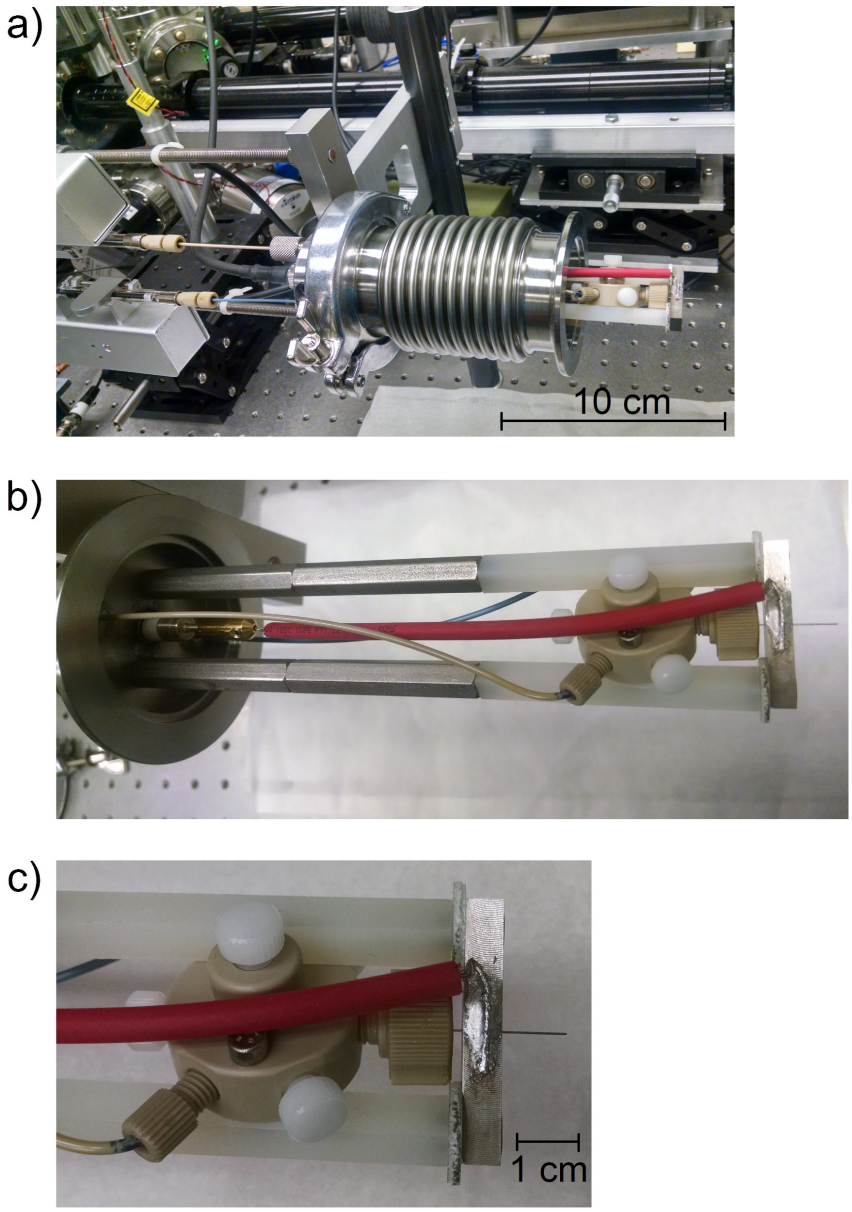

Figure 4.6: (a) The emitter assembly turned sideways for easier access, with the viewing window removed. (b) The emitter assembly with the vacuum bellows removed to show all components. PEEK tubing (tan colored) conducts liquid from the syringes to a 3-way fitting, where both liquids are directed into an emitter needle. The needle is threaded through a stainless steel bar (the HV bar) which is soldered to a wire connected to the high voltage power supply. The HV bar is mounted on non-conducting standoff posts to prevent shorting to the vacuum chamber walls. (c) Close-up of emitter tip.

described in subsequent chapters. A voltage of +2400 V is applied to the emitter tip, while liquid is expelled from the emitter at a rate of 1 μL min^{-1}. An oscillating voltage is applied to the outer electrode of the trap, with amplitude $V_{\text{out}} = 300$ V and frequency $\nu_{\text{t}} = 35$ kHz. A dc bias $V_{\text{dc}} = -3$ V is applied to the inner electrode. Negatively charged particles can be collected by simply reversing the polarities of the emitter voltage and the dc bias. The choice to use positively charged particles for the experiments was arbitrary; I do not have any particular reason to expect different results with negative particles, though if I had more time I would try them.

Particles in the collection chamber are detected in a similar manner to those in the experimental chamber: a 532 nm laser beam is directed through the center of the trap. The scattered light is collected by a lens outside the chamber and focused onto a CCD camera and photodetector [83] (see Fig. 1.1 and Fig. 1.2, parts C-D). Laser power is set to approximately 1 mW for particle visibility during collection, although smaller powers were used for most experiments. During electrospraying, particles can typically be seen on the CCD camera passing through the vicinity of the trap at a rate of approximately 1 per second. Over a few minutes, ten or more particles typically collect in the trap. Unwanted particles may be selectively expelled from the trap by adjusting the trap frequency ν_{t} or the inner electrode dc bias V_{dc}. Decreasing ν_{t} expels particles with higher charge-to-mass ratios, while increasing V_{dc} to a positive value of a few volts (or a negative value if collecting negatively charged particles), with ν_{t} at a relatively high value, expels particles with lower charge-to-mass ratios.

For my experiments, I found it easiest to work with particles of diameter

~ 1 μm and greater. After collection and analysis of many particles, I found that particles of this size usually scatter at least 3×10^6 counts/s at 1 mW total laser power. With a clean system, the median time to collection of such a particle is roughly 15 minutes of electrospraying, with standard deviation 10 minutes.

For a particle of a given charge-to-mass ratio, there is a minimum trap frequency ν_{min} below which the particle cannot be confined. As ν_{t} approaches ν_{min}, the potential well becomes shallow and the image o f the particle on the CCD camera changes shape. For transfer and subsequent study, ν_{t} is set to $1.5 \times \nu_{\mathrm{min}}$.

4.3 Collecting silica particles

In addition to graphene platelets, it is possible to capture silica nanoparticles. I prepared a solution of manufactured silica spheres of diameter 416 nm[84] in the same alcohol/water solution used for graphene suspensions. The spheres were dispersed in the solution by shaking the vial; they stayed suspended for a matter of hours. The spheres were readily captured using the same voltage and trap frequency settings as were used for graphene. Their relatively large size makes them useful for calibration of optics and testing of transfer procedures.

I also attempted to capture gold nanospheres of diameter 250 nm; however, no particles of expected brightness were observed in the trap. This may have been due to the high density of gold, giving the spheres a higher mass relative to their size, so that the drag force of the background gas was insufficient to keep them in the trap.

4.4 Cleaning of the system

With continued use of the particle collection system, graphene particles build up on the inside of the emitter needle. When the emitter is clean, the electrospray cone disappears within ten seconds after the syringe pump is turned off; however, as the needle becomes clogged, the stopping time increases. I have observed that stopping times in excess of 30 seconds are often associated with a decreased rate of trapping of large (~ 1 μm) particles, suggesting that the built up graphene material may be partially blocking the opening. Occasionally, long stopping times are also associated with a skewed electrospray cone, as seen in Fig. 4.1(c). In extreme cases, the electrospray may refuse to start at all.

I attempted to forestall graphene buildup by spraying alcohol/water mixture after each session of particle collection for at least 8 minutes, long enough for several flushes of the plumbing downstream of the 3-way fitting. If a particle is in the collection chamber trap, the electrospray gate valve can be closed during this process. (The roughing pump should be left on to evacuate vapor from the column above the gate valve.) Despite these precautions, the system still eventually showed signs of clogging, usually after several cumulative hours of electrospray. I found that the blockage can usually be cleared by removing the syringe pump and emitter assembly from the system and manually expelling 2000-5000 μL of alcohol/water mixture through the emitter at a fast flow rate. In some cases, the emitter could not be cleaned and had to be replaced. I have attempted to clean the emitter by sonicating it in a vial of 3:1 isopropyl alcohol:deionized water mixture, as well as in

pure alcohol, but this did not seem to reliably improve liquid flow.

Particles also build up around the edge of the pinhole as they pass through, reducing the effective pinhole diameter. This results in a gradual drop in pressure in the collection chamber with continued electrospraying, and usually also a drop in the rate of collection of large particles. For a 75 μm diameter pinhole, the system can be operated for approximately 2-3 cumulative hours of electrospraying before the pressure drops to around 350 mTorr, around which point particles large enough to be convenient for study (on the order of 1 μm in diameter) are no longer collected. Smaller pinholes become clogged even faster. The diaphragm can be cleaned by removing it from the system, placing it in a vial of 3:1 alcohol/water mixture, and sonicating for 30 minutes. The diaphragm should always be handled with clean tweezers. After approximately 3-5 cleanings, the efficiency of cleaning seems to decrease and the diaphragm must be replaced.

Chapter 5: Transfer of particle between two traps

5.1 Overview

Since the electrospray process used to deliver particles to the trap generates considerable water vapor and may introduce impurities into the vacuum chamber, particle collection and experimentation are performed in two separate vacuum chambers. In this chapter, I describe a method of transferring a particle from the collection chamber to the experimental chamber. Some material in this chapter was published in Ref. [59].

Particles are initially collected in a movable trap, which is located in the collection chamber and can be shifted through a gate valve into the experimental chamber. The particle can then be transferred to the fixed trap in the experimental chamber. A diagram of the setup, showing both traps, is shown in Fig. 5.1. The reader may refer back to the photo in Fig 1.2 to get a sense of the location of these components in the context of the entire apparatus; the collection and experimental chambers are labeled A (dark blue) and F (red) respectively, while the transfer mechanism is labeled E (yellow).

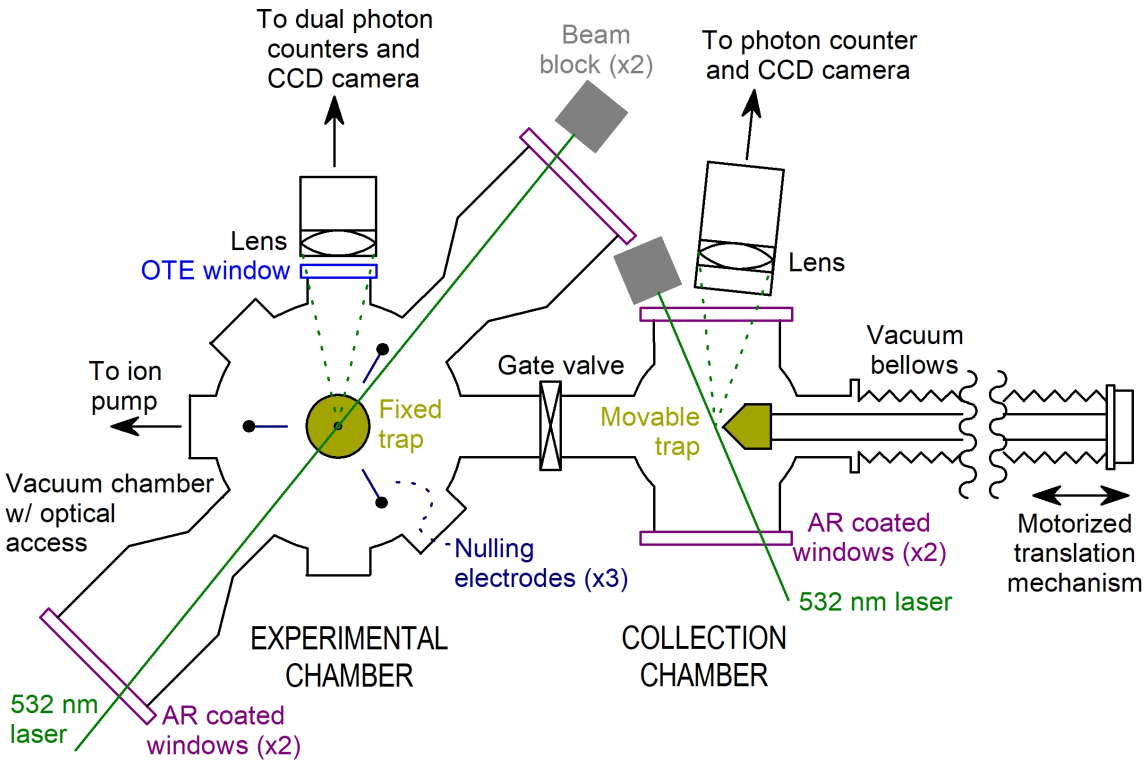

Figure 5.1: Top view of experimental apparatus. Particle collection and experimentation are performed in separate chambers to avoid contamination. A particle is initially collected in a trap mounted on a motorized linear translation mechanism. With the gate valve open, the movable trap can be brought near the fixed trap and the particle can be transferred between traps. The movable trap is shown fully retracted; in this position the distance between traps is 24.5 cm. The fixed trap is surrounded by three identical electrodes ("nulling electrodes") consisting of thin metal rods. DC voltages may be put on these electrodes to displace the particle slightly in order to ensure a successful transfer. Both chambers may be evacuated by a turbo pump (not shown) or an ion pump.

5.2 Apparatus and procedure

The trap in which the particle is collected (the"movable trap" in Fig. 5.1) is mounted with its axis of symmetry horizontal on a rod 200 mm in length. The trap is moved using a linear translation mechanism [85] (Fig. 5.2). The translation mechanism is controlled with the combination of a servo motor [86], and a planetary gear [87] with a ratio of 10:1. A micrometer is fitted to the translation mechanism to read out the position of the trap, which can be controlled to within 0.1 mm. The trap is moved with an acceleration of approximately 0.8 mm sec^{-2} and a maximum speed of 0.8 mm sec^{-1}. Gradual acceleration is used to avoid particle escape.

Initial particle capture is performed with the gate valve between the two chambers closed. Once a particle is captured, the collection chamber is pumped down to below 5×10^{-7} Torr in order to evacuate most of the water vapor residue. The gate valve is then opened to allow the movable trap to pass through. At μTorr pressures, the particle's motion is weakly damped, and it is likely that the particle will escape from the trap (as the potential well becomes shallower) during transfer. For this reason, pressure is increased to 30 mTorr using helium gas from a clean source [88]. The outer electrode voltages are set at maximum ($V_{\text{moving}} = 300$ V) for the movable trap and roughly 80% of maximum ($V_{\text{fixed}} = 250$ V) for the fixed trap. The movable trap moves along its own axis of symmetry, which is positioned about 1 mm above the tip of the fixed trap. The tip of the movable trap is brought to a distance of about 1 mm from the axis of the fixed trap. Optionally, the inner electrode dc bias may be set at $V_{\text{dc}} = -4V$ to pull the particle closer to the trap while it is moved.

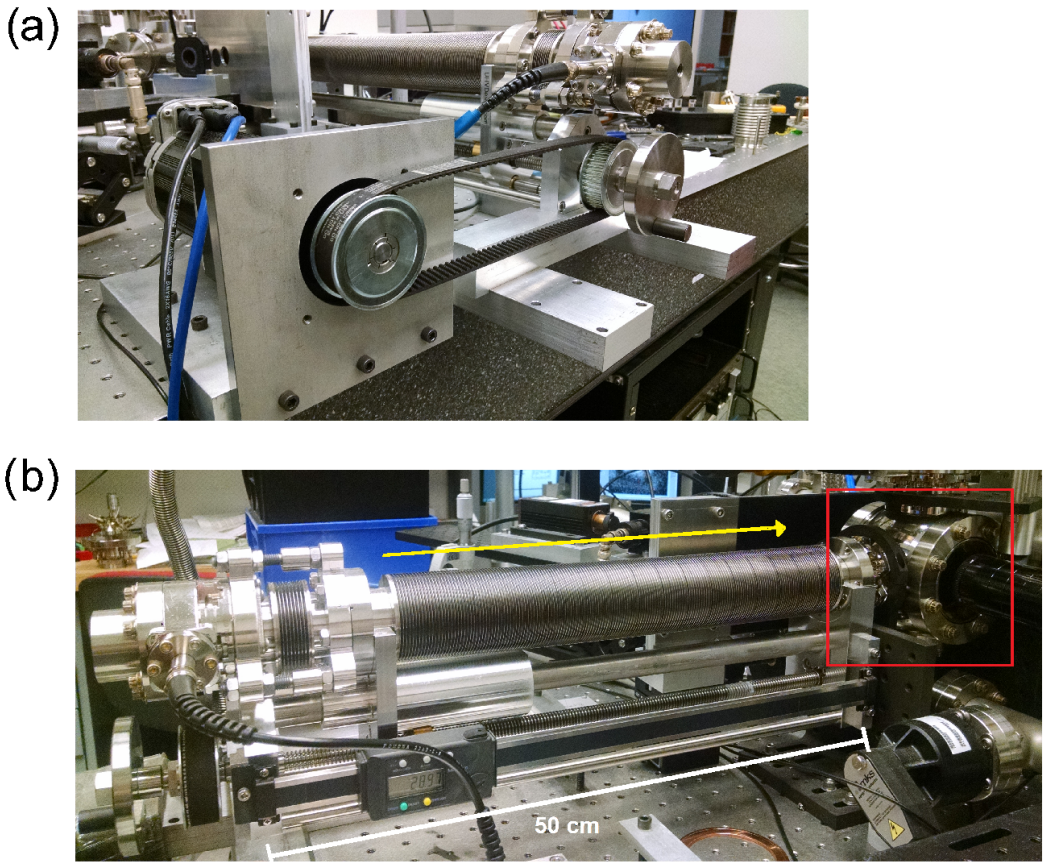

Figure 5.2: (a) Photo of motor/gear assembly that drives the linear translation mechanism. (View from left side of setup.) (b) Photo of linear shift mechanism with flexible vacuum bellows. (View from right side of setup.) The system is shown in the retracted position, with the movable trap in the collection chamber. The vacuum bellows can compress to allow the trap to be moved past the UHV gate valve into the experimental chamber. The direction of travel is shown by a yellow arrow. The collection chamber is highlighted by a red rectangle.

Especially for smaller particles, this seems to decrease the likelihood of particle loss. After movement of the trap, the bias is reset to zero. The potential landscape at this point in the transfer process is shown in Fig. 5.3(a). It is usually possible to see the particle on the CCD camera in the subsequent steps of the transfer process.

At this point in the transfer process, two potential wells are visible in the simulation images. The particle sits in the lower left well but has a chance of escaping to the upper right well as the potential barrier between the wells drops during transfer. With the traps stationary, the voltage on the fixed trap is increased to maximum ($V_{\text{fixed}} = 300$ V). The resulting potential landscape is shown in Fig. 5.3(b). The voltage on the movable trap is then decreased to $V_{\text{moving}} = 250$ V, causing the well containing the particle to move closer to the fixed trap and the empty well to move off to the upper left of the diagram (see Fig. 5.3(c)). The movable trap voltage is further decreased to $V_{\text{moving}} = 30$ V in small increments as the trap is retracted to a distance of 2.4 mm (see Fig. 5.3(d)). Finally, the movable trap is retracted to its initial position in the collection chamber. The experimental chamber can now be isolated by closing the gate valve. For a large particle (diameter ~ 1 μm) my transfer success rate at a pressure of 30 mTorr was nearly 100% when the traps were properly aligned.

5.3 Conditions for successful transfer

Both practice and simulations show that the ideal displacement of the tip of each trap from the axis of the other trap is 1 mm. Larger separation distances result

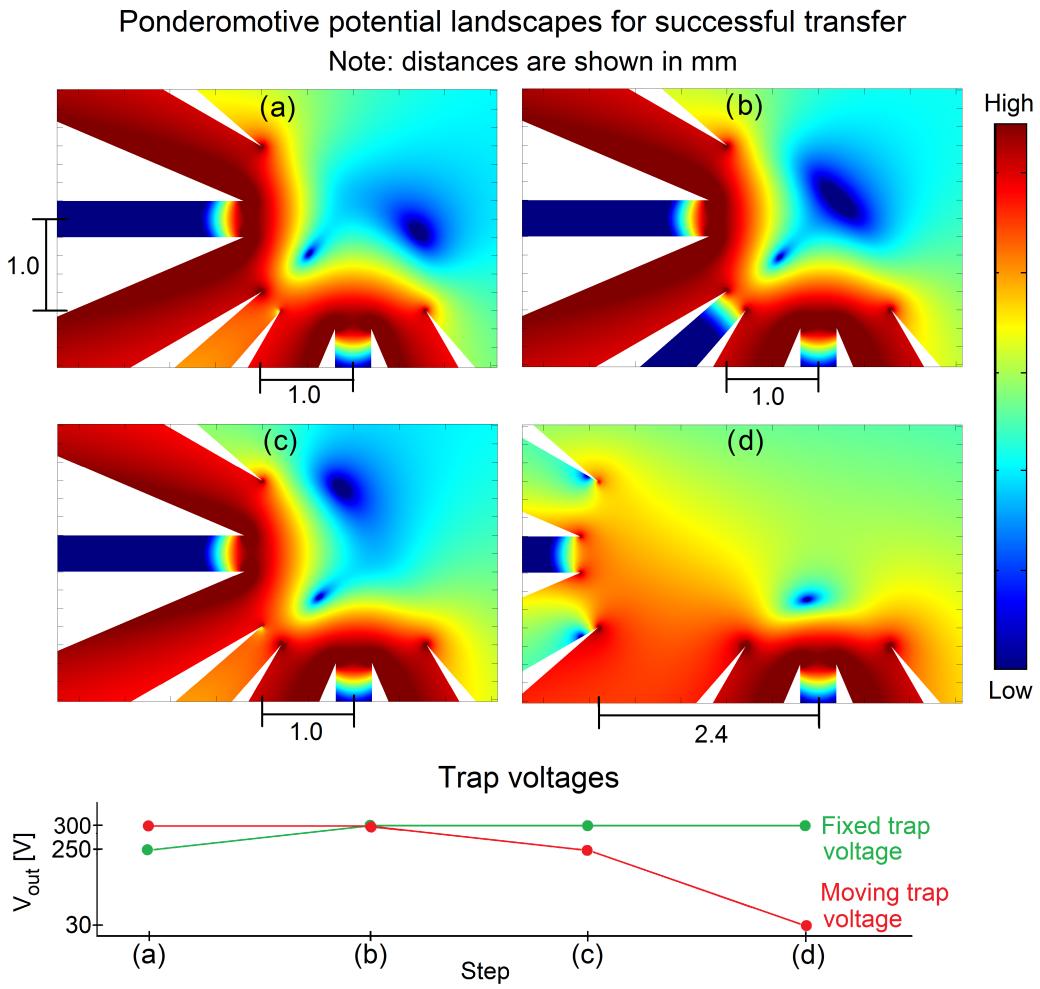

Figure 5.3: Cross-sectional view of ponderomotive potential landscape at four "snapshot" moments during transfer. The trapped particle is attracted to regions of lowest potential (blue). The section plane is vertical, so that the movable trap appears on the left and the fixed trap appears at the bottom. The slot in the fixed trap is neglected for simplicity. The trap voltages for each of the four snapshots are shown at the bottom. A successful transfer is shown in parts (a-d). (a) With $V_{\text{moving}} = 300$ V, $V_{\text{fixed}} = 250$ V, the traps are brought into proximity such that the tip of each trap is offset by 1 mm from the axis of the other trap. The particle lies in the lower left hand well. (b) V_{fixed} is increased to 300 V. (c) V_{moving} is decreased to 250 V. The empty well moves toward the upper left, while the well containing the particle moves toward the fixed trap. (d) The movable trap is retracted to about 2.4 mm from the axis of the fixed trap as V_{moving} is decreased to 30 V. The well containing the particle now lies above the fixed trap.

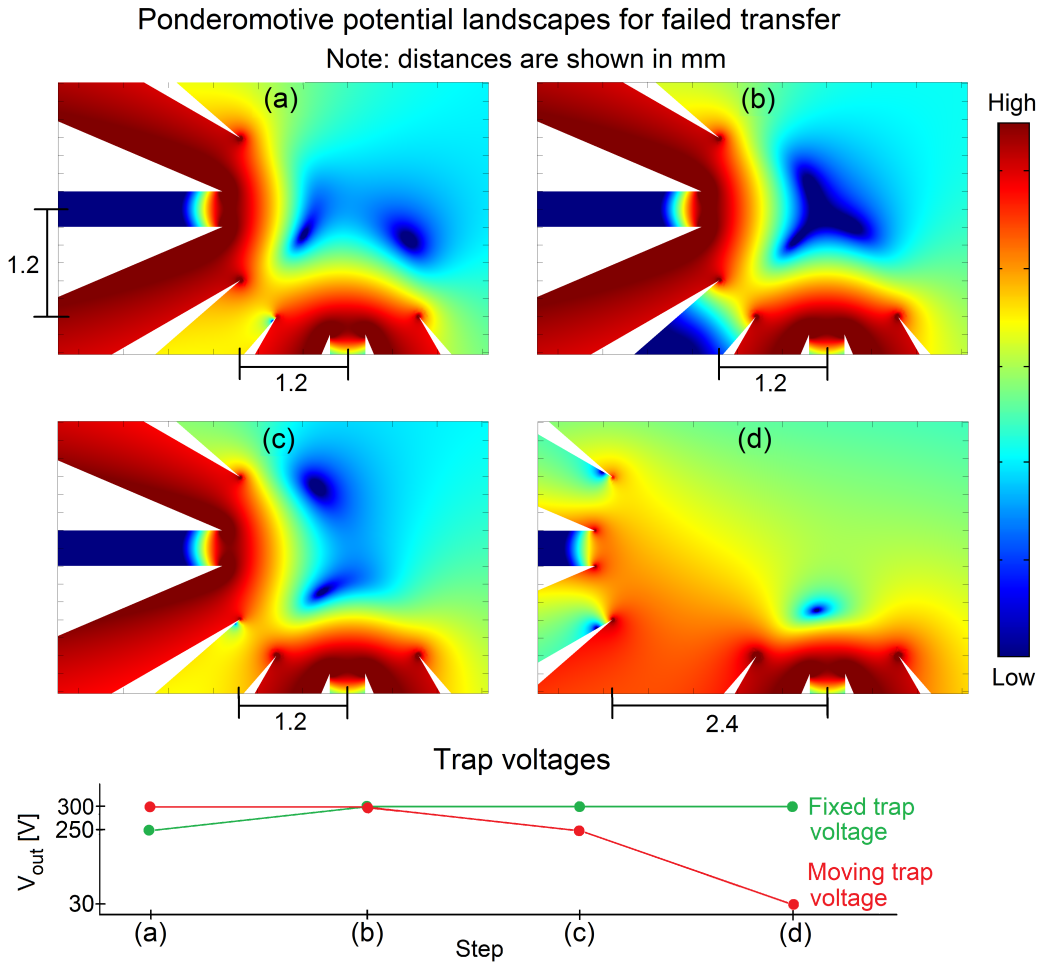

Figure 5.4: Cross-sectional view of ponderomotive potential landscape at four "snapshot" moments during transfer. The trapped particle is attracted to regions of lowest potential (blue). The section plane is vertical, so that the movable trap appears on the left and the fixed trap appears at the bottom. The slot in the fixed trap is neglected for simplicity. The trap voltages for each of the four snapshots are shown at the bottom. An unsuccessful transfer is shown in parts (a-d). (a) The tip of each trap is offset by 1.2 mm from the axis of the other trap. (b) As V_{fixed} is increased, the two wells combine. (c) When the wells separate as $V_{\text{moving}} \to 250$ V, the particle remains in the upper well unless a large dc voltage is applied to the auxiliary electrodes to draw the particle down toward the fixed trap. (d) As $V_{\text{moving}} \to 30$ V, the upper well disappears and the particle is lost.

in loss of the particle during transfer; I now examine an example of this failure.

A transfer simulation with each trap displaced by 1.2 mm is shown in Fig. 5.4(a-d). In this case, the two wells join together (see Fig. 5.4(b)) as the fixed trap voltage is increased to maximum. As the movable trap voltage is decreased and the wells separate and move apart, the particle is likely to remain in the upper well and fail to transfer to the fixed trap. With vertical and horizontal separations ranging from 1.2-1.4 mm, a successful transfer can still sometimes be achieved by applying a large voltage to all three auxiliary nulling electrodes (shown in Fig. 5.1) to pull the particle downwards to keep it in the correct well. For trap displacements of 1.6 mm or greater, the well containing the particle completely fails to transfer to the fixed trap.

In the configuration used for the experiments in this thesis, the trap voltages were sourced from a dual-channel signal generator and amplified using identical high-voltage amplifiers [63]. During transfer, the ac voltages on the two traps must be in phase with each other. I found that a phase difference of more than about 10 degrees resulted in an unsuccessful transfer.

5.4 Simultaneous operation of two traps

In order to increase throughput of particles for study, a second particle can be collected in the movable trap while the first particle is being studied in the experimental chamber. The movable trap voltages can be sourced from an alternate channel of the signal generator, so that the frequency of the movable trap can be

adjusted without affecting the operation of the fixed trap. With the UHV gate valve between the chambers closed, particle collection activity does not appear to affect the particle in the experimental chamber.

Chapter 6: Platelet rotation induced by circularly polarized light

6.1 Overview and apparatus

It is well known that light can carry angular momentum, which can be transferred to physical objects [89][90]. Due to graphene's high optical absorption, a trapped platelet can be easily made to rotate by exposing it to circularly polarized light (CPL). For a platelet with a small number of layers n, the optical absorption cross section σ_{abs} of a platelet oriented normal to the incident radiation scales linearly with n [16]:

$$\sigma_{abs} \cong 0.023 \times n\pi a^2, \tag{6.1}$$

where a is the radius of the platelet. Thus, a monolayer absorbs 2.3% of the light incident on it. Since CPL carries angular momentum, it will transfer torque to the platelet upon absorption.

The trap in the experimental chamber has a hole of radius 0.2 mm drilled through its axis to admit a circularly polarized laser beam (see Fig. 2.6). The light has a wavelength of 671 nm. Circular polarization is created with a Pockels cell set at half its maximum voltage. In most cases, exposing a platelet to a total power

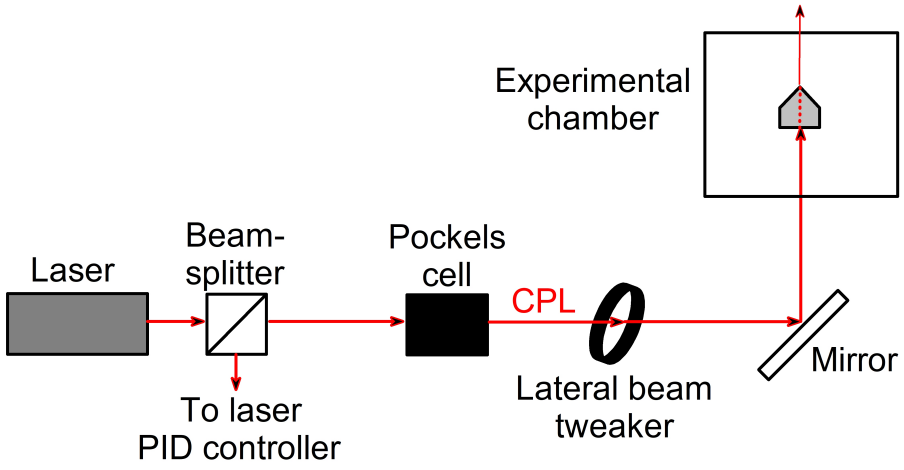

Figure 6.1: Diagram of optics used for application of circularly polarized light. 671 nm (red) laser light is sampled by a beam splitter to provide a measurement of the power to a PID controller, which stabilizes the laser power output. The light transmitted through the beamsplitter passes through a Pockels cell, which can be used to create circular polarization. Using a movable lens on a gimbal mount, the beam is aimed at a mirror and reflected up into the experimental chamber and through the hole in the axis of the trap.

of 100-300 μW is sufficient to induce rotation. As discussed in Ch. 2, the platelet's motion is probed entirely optically. A 532 nm linearly polarized laser is directed at the platelet and the scattered light is collected in a lens and focused onto a CCD camera and a pair of high-speed photodetectors. The sum of the photodetector signals provides information about the platelet's rotational motion.

6.2 Procedure for spinning up a platelet

After the platelet is captured and transferred to the experimental chamber, the chamber is pumped down with the turbo pump. To prevent the platelet from escaping the trap during pumpdown, a parametric feedback cooling signal [19][20] is

applied to the trap electrodes at a low gain level. In the experiments described here, the cooling strength used is just enough to keep the platelet in the trap; however, the temperature associated with its translational motion remains near 300 K.

The circularly polarized laser is unblocked after the pressure drops below about 1×10^{-6} Torr. After a period of illumination, a sharp peak develops in the power spectral density of the scattered light, indicating that the platelet is rapidly rotating. A typical plot of this frequency peak over time is shown in Fig. 6.2. As will be discussed in Ch. 7, the scattered light intensity is unchanged under a rotation of 180°. Thus, in Fig. 6.2, the lowest visible harmonic is actually twice the rotation frequency.

Figure 6.3 shows the scattered light signal for the same platelet. Before the platelet is exposed to CPL, its center-of-mass motion is constrained by the trapping fields, but its orientation is free, so it tumbles randomly as it is buffeted by background gas molecules. After exposure to CPL, the platelet orients into the horizontal plane, so that its surface is perpendicular to the circularly polarized laser. Since the detection laser is polarized in the vertical direction, the scattering intensity decreases. Since the platelet's orientation is now constrained by the torque imparted by the CPL, the fluctuations in the scattered light signal decrease dramatically.

6.3 Behavior of a spinning platelet

The time taken for a platelet to reorient upon exposure to CPL varies from under a minute to an hour. Data from two other platelets (labeled 101415B and

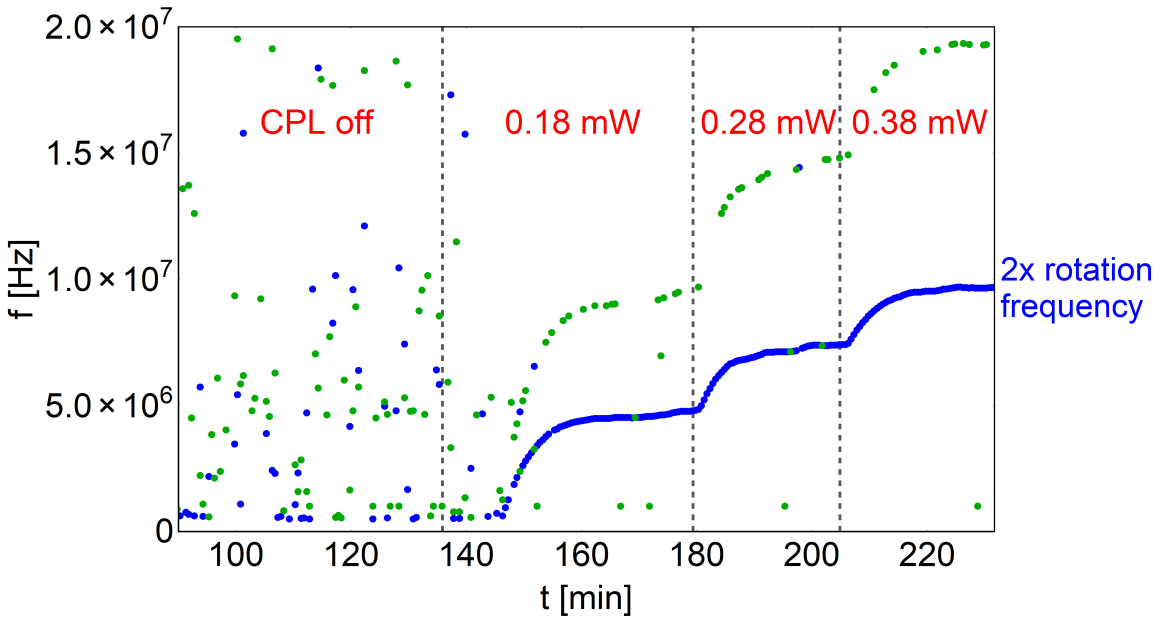

Figure 6.2: Frequency f of scattered light signal versus time t since beginning of chamber pump-down, showing spin-up of platelet. Chamber is being pumped by turbo pump. Pressure at first exposure to circularly polarized light is approximately 2×10^{-7} Torr. Approximately 10 min after first exposure to CPL, two peaks become evident. Note that the lower of the two harmonics shown (blue) is twice the actual spinning frequency. Spinning frequency approaches a terminal value after a few tens of minutes and increases when the laser power is increased. Data taken on July 7, 2016 with sample 070616D.

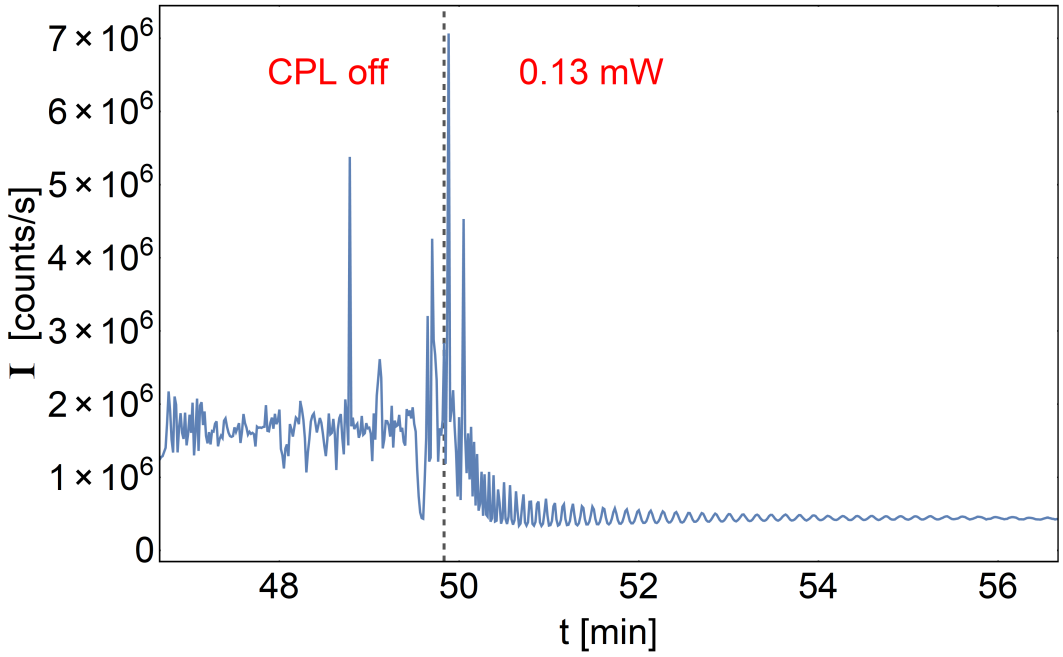

Figure 6.3: Plot of scattered light intensity I versus time t, showing the reorientation of a nanoplatelet upon exposure to circularly polarized laser. The intensity of the scattered light drops as the platelet begins to rotate and orients into the horizontal plane (perpendicular to the circularly polarized laser and to the direction of polarization of the detection laser). Fluctuations in the scattered light diminish as the platelet's orientation stabilizes. Data taken on April 15, 2016 with sample 041516B.

070616D) are shown in Fig. 6.4. Since graphene's optical absorption scales linearly with area and number of layers (for small n), it is likely that the platelets that take a longer time to reorient have fewer layers.

Figure 6.2 shows that the rotation frequency generally increases with larger CPL powers. CPL power is not a convenient control knob for rotation frequency, however, for two reasons. First, the terminal rotation frequency depends on frictional torques from the background gas and the laser power, meaning that small fluctuations in the chamber pressure can cause the frequency to vary. In practice, we have observed considerable drift in the frequency at constant laser power. Second, achieving high rotation frequencies requires continuous exposure to high laser power, which may heat the platelet enough to cause it to escape the trap. In the next chapter, I discuss a method of locking the rotation frequency of the platelet using radio frequency electric fields.

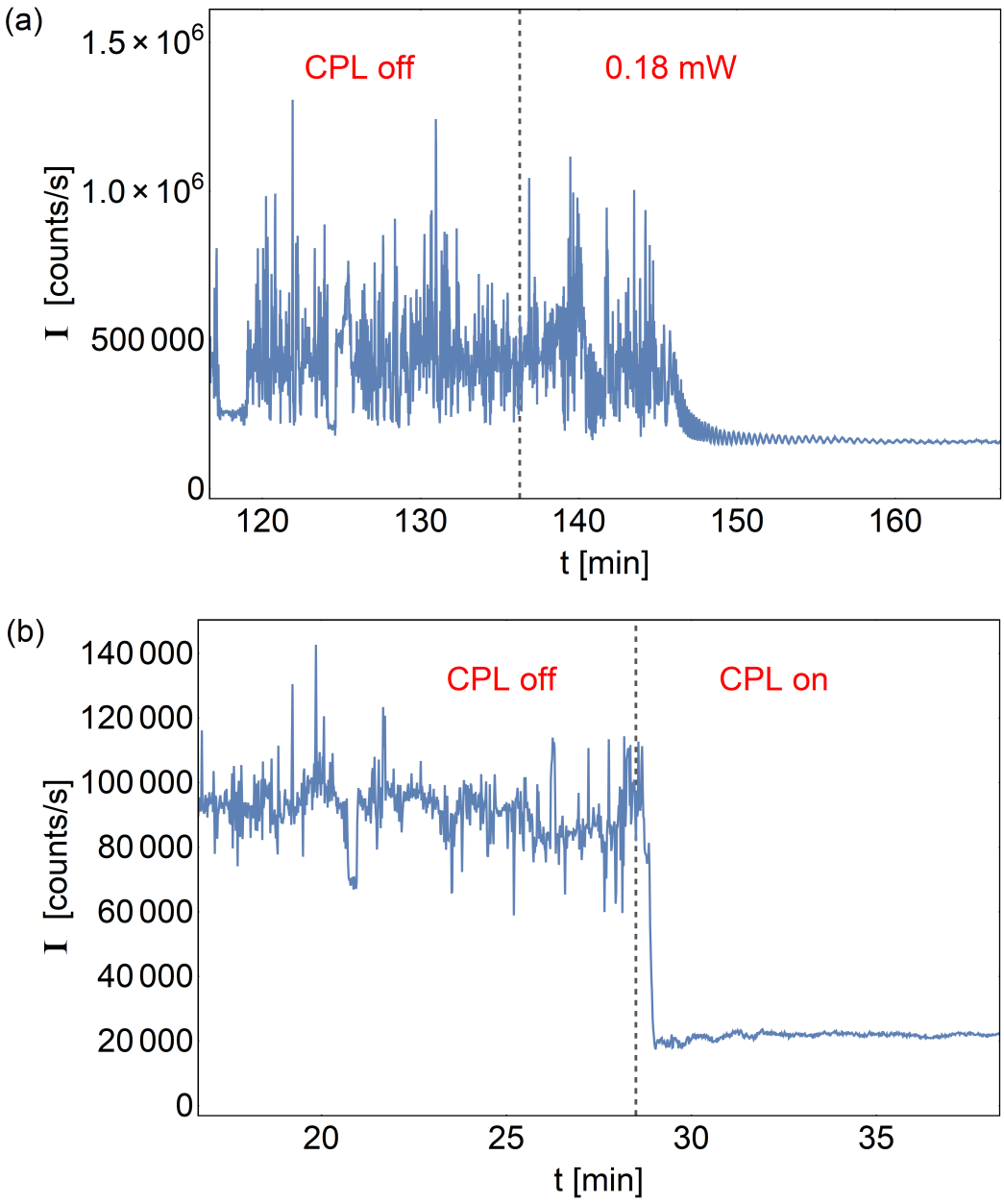

Figure 6.4: Additional examples of reorientation of a nanoplatelet upon exposure to circularly polarized laser. Time taken to reorient varies between samples, even when laser power is kept constant. (a) shows data taken October 15, 2015 on sample 101415B, which took about 1 minute to reorient. (b) shows data taken July 7, 2016 on sample 070616D, which took about 10 minutes to reorient.

Chapter 7: Gyroscopic stabilization using rf electric fields

7.1 Overview

Because a typical platelet used in these experiments is an irregularly shaped object with a fixed distribution of electric charge on its surface, it possesses an electric dipole moment. This dipole moment can couple to an applied electric field. If an oscillating electric field is applied at a frequency near the instantaneous rotation frequency of a platelet that has been spun up using circularly polarized light, its rotation frequency will become locked to the frequency of the applied field, and will subsequently behave like a gyroscope. In this chapter, I describe the implementation of this concept used in my experiments. Some material in this chapter was published in Ref. [60].

7.2 Frequency-locking apparatus and procedure

Frequency locking of the rotation is achieved by applying a large oscillating voltage on the inner electrode of the trap. The rf power is supplied by a 100 W amplifier and is routed into and out of the vacuum chamber on separate feedthroughs (see Fig. 7.2). Resonances and reflections of the rf are minimized by terminating the

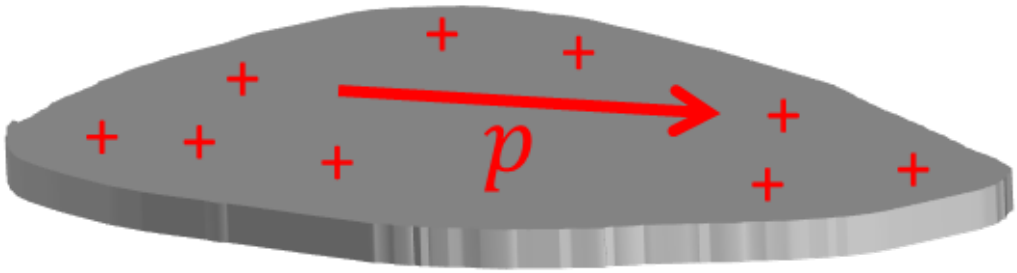

Figure 7.1: Cartoon of graphene nanoplatelet. A typical nanoplatelet is irregular in shape and has charge fixed to its surface, giving it a net electric dipole moment.

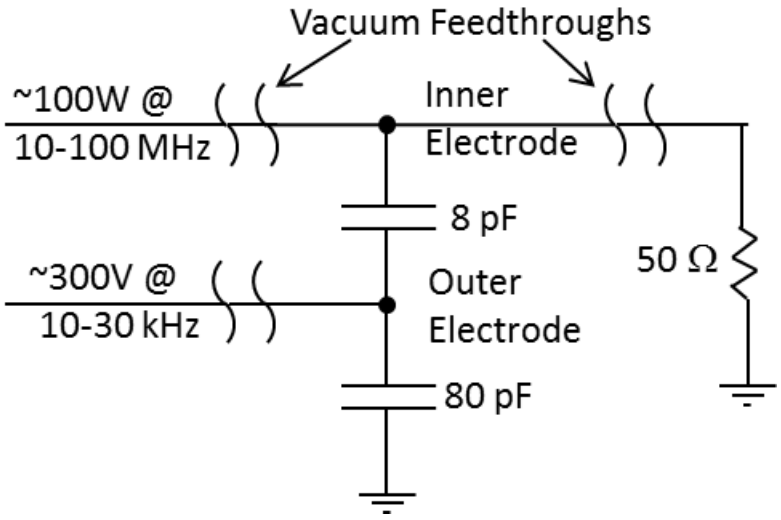

Figure 7.2: Circuit diagram showing application of trapping voltage and frequency-locking drive voltage to trap electrodes.

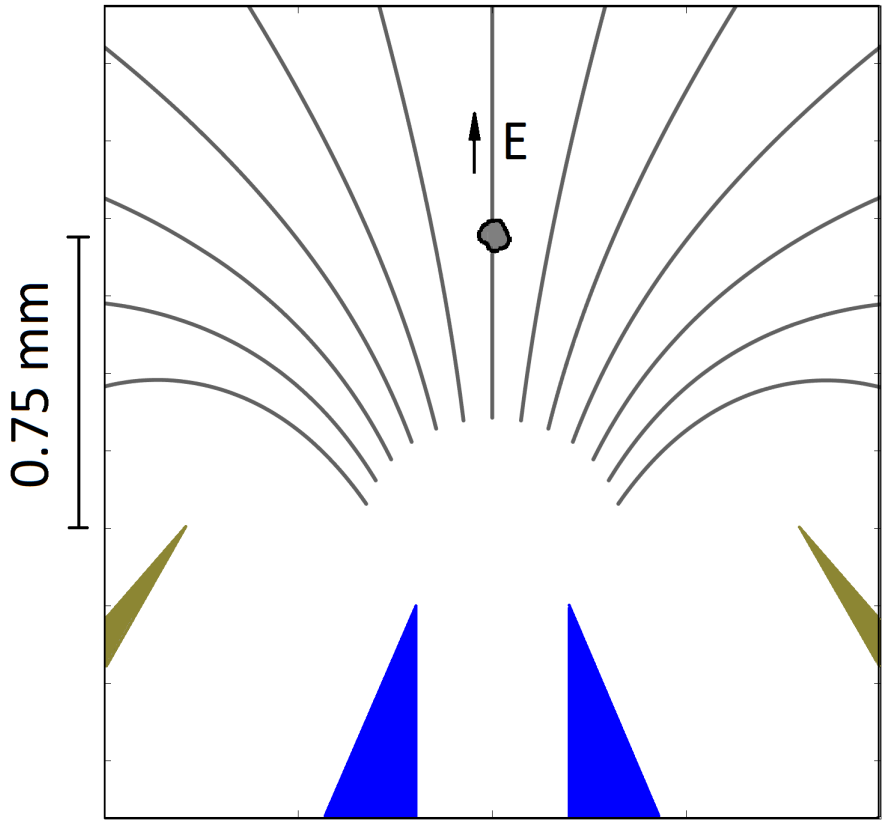

Figure 7.3: Cross-section of tip of trap electrodes showing electric field lines. The rf drive field is created by applying a voltage to the inner electrode of the trap. Platelet is shown (not to scale) at approximate trap center.

lines with 50 Ω. As a result, the rf frequency can be swept over a large range with minimal electric field amplitude variations at the location of the trapped platelet. Modeling of the trap indicates that the relationship between the inner electrode voltage V_{inner} and the resulting rf electric field amplitude E_0 is E_0 [kV m^{-1}] $\approx$ $100 \times V_{\text{inner}}$ [V_{pp}]. For most of my experiments, I used an inner electrode voltage of 160 V (peak-peak), so that the amplitude of the rf electric field at the trap center was approximately 16 kV m^{-1}.

Electric field lines in the vicinity of the trap center are shown in Fig. 7.3. The rf oscillations do not contribute to significant translational motion: for the typical charge to mass ratios of trapped platelets ($q/m \cong 10$ C kg^{-1}), the maximum rf field at 10 MHz leads to platelet motion of order 0.1 nm, which is far smaller than the thermally induced motion of the platelet in the trap.

Locking is established by applying an rf signal at one half the frequency (typically 10-20 MHz) of the peak observed in the PSD of the optical signal (see Fig. 7.4). (The factor of one half arises because, as will be explained in Sec. 7.3.2, the lowest visible harmonic is twice the actual rotation frequency.) In practice, I found that there is a moderate margin of error for mismatch of the rf signal and the instantaneous platelet rotation frequency; for locking to occur, the rf signal must be within about 100 kHz of the rotation frequency when it is turned on.

When locked, the PSD peak remains at a constant frequency and sidebands appear in the spectrum, located at a distance of order 10 kHz from the central peak. The platelet remains locked when the source of circularly polarized light is turned off, and the offset frequencies of the sidebands stabilize. Stable locking has been

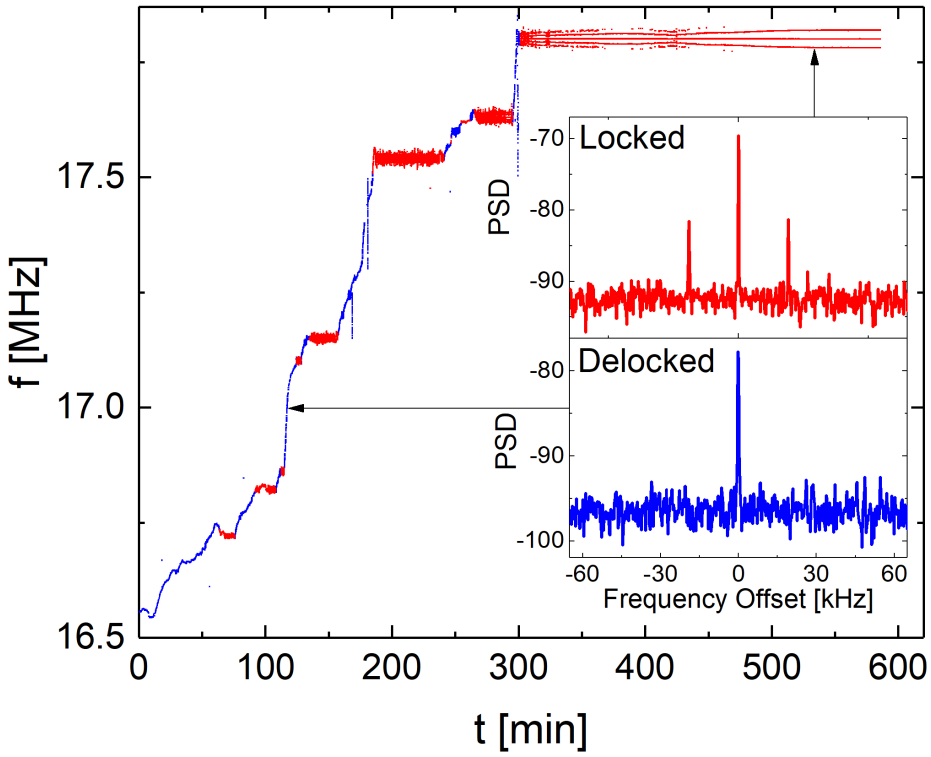

Figure 7.4: Plot of rotation frequency f of the platelet versus time t, showing locking of the rotation of the platelet to an external rf electric field. Blue regions indicate where the platelet is only experiencing torques from the circularly polarized laser, which spin the platelet up to MHz frequencies. In red regions $\boldsymbol{E}_{\mathrm{rf}}$ is turned on and the platelet becomes locked to the applied field. Insets show that sidebands appear on the optical signal only when locking occurs. Data taken December 19, 2015 by Pavel Nagornykh, on sample 121115E.

achieved for periods of several weeks on a few individual platelets in our laboratory.

7.3 Model of frequency-locked nanoplatelet

To gain insight into the behavior of a locked platelet, I now discuss a simple dynamical model with the following assumptions:

1. The platelet is an irregularly shaped rigid two dimensional object; *i.e.,* its

lateral dimensions greatly exceed its thickness.

2. The platelet possesses a permanent electric dipole moment $\boldsymbol{p}$ lying in the 2D plane of the platelet. $\boldsymbol{p}$ arises because the charge and mass distributions are distinct in charged conducting objects and consequently any such object lacking symmetry will experience a torque in an electric field.

3. The platelet always rotates around an axis perpendicular to the plane in which it lies.

The third assumption is certainly *not* valid in general; however, in systems where rotational energy exceeds the thermal energy, $k_{\mathrm{B}}T$, and where angular momentum is conserved, but where rotational energy can be rapidly exchanged with internal degrees of freedom, rotation tends to stabilize around the principle axis with the largest value of the moment of inertia tensor [91]. This axis for 2D objects is always perpendicular to the object's surface, with moment of inertia denoted by $I_{\perp}$.

It is possible that thermal effects could cause fluctuations in the instantaneous axis of rotation of the flake. In our system, however, thermal rotation frequencies are on the order of $\omega_{th} \cong \sqrt{k_{\mathrm{B}}T/I_{\perp}} \cong 10^4$ rad sec^{-1}, much less than the rotational angular velocities typically measured when the rotation is locked to $\boldsymbol{E}_{\mathrm{rf}}$, which are on the order of 10^6 rad sec^{-1} and higher. Also, the following analysis focuses on the low frequency response of the plane to external torques, and thus fluctuations in the instantaneous axis of rotation of the platelet are likely to be averaged out.

To model platelet dynamics, I assume an oscillatory electric field $\boldsymbol{E}_{\mathrm{rf}}$ is directed

along $\hat{\boldsymbol{z}}$, and the components of $\boldsymbol{E}_{\mathrm{rf}}$ in the local platelet frame (Fig. 7.5) are

$$E_\theta = E_0 \sin(\theta)\cos(\omega_0 t), \tag{7.1}$$

$$E_\phi = 0, \tag{7.2}$$

$$E_n = -E_0 \cos(\theta)\cos(\omega_0 t), \tag{7.3}$$

where E_0 and ω_0 are the amplitude and angular velocity of $\boldsymbol{E}_{\mathrm{rf}}$. The components of $\boldsymbol{p}$ are

$$p_\theta = p_0 \cos(\omega_0 t + \psi), \tag{7.4}$$

$$p_\phi = p_0 \sin(\omega_0 t + \psi), \tag{7.5}$$

$$p_n = 0, \tag{7.6}$$

where ψ is the phase deviation of the dipole from perfect synchrony with the applied field, and is assumed to vary slowly compared to ω_0. The torque, $\boldsymbol{N} = \boldsymbol{p} \times \boldsymbol{E}_{\mathrm{rf}}$, on the platelet is then:

$$\boldsymbol{N} = p_0 E_0 \begin{vmatrix} \hat{\boldsymbol{\theta}} & \hat{\boldsymbol{\phi}} & \hat{\boldsymbol{n}} \\ \cos(\omega_0 t + \psi) & \sin(\omega_0 t + \psi) & 0 \\ \sin(\theta)\cos(\omega_0 t) & 0 & -\cos(\theta)\cos(\omega_0 t) \end{vmatrix}. \tag{7.7}$$

Simplifying the above expression using sine and cosine formulas and retaining only the terms that are not rapidly oscillating, one finds the three components of the torque:

$$N_\theta = -\frac{1}{2} p_0 E_0 \cos(\theta)\sin(\psi), \tag{7.8}$$

$$N_\phi = +\frac{1}{2} p_0 E_0 \cos(\theta)\cos(\psi), \tag{7.9}$$

$$N_n = -\frac{1}{2} p_0 E_0 \sin(\theta)\sin(\psi). \tag{7.10}$$

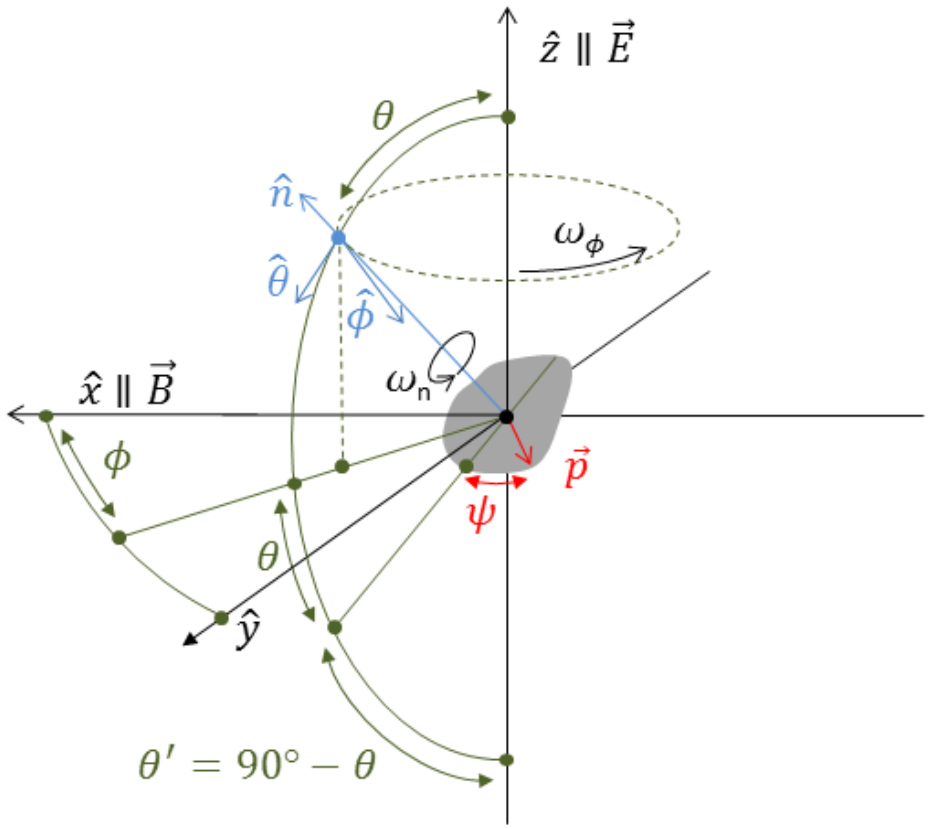

Figure 7.5: Diagram of a spinning graphene nanoplatelet. I assume that the platelet spins on an axis $\hat{\boldsymbol{n}}$ normal to its surface and that a permanent electric dipole moment $\boldsymbol{p}$ lies in the plane of the platelet. An oscillatory electric field is parallel to the z axis. A dc magnetic field will be applied along the x axis in later experiments (see Ch. 9). The local platelet-frame Cartesian coordinate system denoted by $[\hat{\boldsymbol{\theta}}, \hat{\boldsymbol{\phi}}, \hat{\boldsymbol{n}}]$, used in calculations, does *not* rotate with the platelet.

7.3.1 Oscillations in rate of axial rotation

First, I address the in-plane oscillations of the dipole around its minimum energy orientation. Rotations around the axis $\boldsymbol{n}$ normal to the plane of the platelet will obey:

$$N_n = \dot{L}_n = I_\perp \dot{\omega}_n = I_\perp \ddot{\psi} = -\frac{1}{2} p_0 E_0 \sin(\theta) \sin(\psi) \tag{7.11}$$

where $\boldsymbol{L}$ is angular momentum of the platelet. For small ψ, this equation yields simple harmonic oscillations with angular velocity:

$$\omega_\psi^2 = \frac{p_0 E_0}{2 I_\perp} \sin(\theta) \equiv \Omega^2 \sin(\theta). \tag{7.12}$$

These oscillations lead to deviations of ω_n, the instantaneous angular rotation velocity of the platelet, from ω_0. They are entirely analogous to the torsional oscillations observed recently in optically levitated non-spherical particles [57] and manifest themselves as sidebands to the measured frequency of rotation observed in the PSD of the scattered light. They are actually librations of the platelet viewed in a frame rotating synchronously with $\boldsymbol{E}_{\mathrm{rf}}$. Averaging over times longer than the period of the ω_ψ oscillations, one can make the approximation $\omega_n = \omega_0$.

7.3.2 Optical scattering from nanoplatelets and the appearance of sidebands

The nanoplatelets measured in the experiments are typically comparable to or larger than the 532 nm wavelength of the probing light, while the thickness of the platelet is much smaller than the wavelength. In the Rayleigh-Gans approximation

[92], where the scatterer has negligible effect on the incident radiation, the intensity of light scattering is dominated by the form factor:

$$F(\tilde{\boldsymbol{k}}) = \left| \int_S d\boldsymbol{r} e^{i\tilde{\boldsymbol{k}}\cdot\boldsymbol{r}} \right|^2, \tag{7.13}$$

where $\tilde{\boldsymbol{k}}$ is the wavevector difference between incident and scattered light and the integral is taken over the surface of the platelet. I neglect the polarization of the light, since the measurements are performed when the direction of the polarization is $\perp$ to $\tilde{\boldsymbol{k}}$. For a 2D plate-like object lying in the plane perpendicular to $\hat{\boldsymbol{n}}$:

$$F(\tilde{k}_\theta, \tilde{k}_\phi, \tilde{k}_n) = F(\tilde{k}_\theta, \tilde{k}_\phi, -\tilde{k}_n). \tag{7.14}$$

Additionally, time reversal symmetry implies that $F(\tilde{\boldsymbol{k}}) = F(-\tilde{\boldsymbol{k}})$. Thus:

$$F(\tilde{k}_\theta, \tilde{k}_\phi, \tilde{k}_n) = F(-\tilde{k}_\theta, -\tilde{k}_\phi, \tilde{k}_n). \tag{7.15}$$

This result implies that the form factor is unchanged when the nanoplatelet is rotated 180° around an axis perpendicular to its surface. An ellipse-shaped nanoplatelet with a smooth, flat surface rotating at angular velocity ω_n around $\hat{\boldsymbol{n}}$ will thus only have optical modulation at even harmonics. This is, in fact, what I have observed in these experiments, as discussed in Sec. 7.2. In general, when a platelet is rf-locked, the strongest peak in the power spectrum of the scattered light appears at twice the drive frequency, although odd harmonics with significantly smaller magnitude are observable for some platelets. These odd harmonics likely result from an irregularity in shape; for example, they may occur if a multilayer platelet has more layers at one end than the other.

The intensity of the scattered light must be modulated with a frequency twice that of the drive frequency ω_0, with a phase deviation related to the small in-plane oscillations discussed in Sec. 7.3.1. If these oscillations obey

$$\psi(t) = \psi_o \sin(\omega_\psi t), \tag{7.16}$$

then the optical signal will be:

$$I(t) = \sum_n A_{2n} e^{2ni(\omega_0 t + \psi_0 \sin(\omega_\psi t))}, \tag{7.17}$$

where ψ_0 is the amplitude of the small in-plane oscillations discussed in Sec. 7.3.1, A_{2n} is a coefficient related to the strength of the $2n$-th harmonic, and n runs from 1 to infinity. The sum includes only even harmonics, as discussed above. When ψ_0 is small, the following approximation is valid:

$$e^{2ni\psi_0 \sin(\omega_\psi t)} \cong 1 + 2ni\psi_0 \sin(\omega_\psi t) = 1 + n\psi_0(e^{i\omega_\psi t} - e^{-i\omega_\psi t}). \tag{7.18}$$

Thus:

$$I(t) = \sum_n A_{2n}[e^{2ni\omega_0 t} + n\psi_0(e^{i(2n\omega_0+\omega_\psi)t} - e^{i(2n\omega_0-\omega_\psi)t})]. \tag{7.19}$$

The sidebands are displaced from all harmonics by $\pm\omega_\psi$. The ratio R of the power in the sidebands to the power in the harmonics can be used to determine ψ_0:

$$R = \frac{P(2n\omega_0 \pm \omega_\psi)}{P(2n\omega_0)} = n^2\psi_0^2. \tag{7.20}$$

The ratio R can be determined experimentally by measuring the spectral density of the total $(A + B)$ photodetector signal with a high-speed oscilloscope. (See Ch. 2 for a description of the photodetector setup.)

If rotational motion of the locked flake is thermal, then, from the equipartition theorem:

$$k_B T \approx \frac{1}{2} p_0 E_0 \sin(\theta) \left\langle \psi^2 \right\rangle , \tag{7.21}$$

Averaging over a full cycle, the mean square amplitude is one-half the square of the maximum amplitude: $\langle \psi^2 \rangle = (1/2)\psi_0^2$. Using $n = 1$ because I study the signal at the second harmonic, Eqs. 7.20 and 7.21 simplify to:

$$R = \frac{P(2\omega_0 \pm \omega_\psi)}{P(2\omega_0)} = \frac{4 k_B T}{p_0 E_0 \sin(\theta)}. \tag{7.22}$$

The electric dipole moment p_0 can now be determined if the orientation angle θ is known. It is likely that axial oscillations are rapidly thermalized with internal degrees of freedom of the flake and that $T \approx$ 300 K. Although substantial heating of the illuminated particle is possible in a high vacuum environment, the low laser powers used in the present experiments would not be expected to raise the internal temperature significantly above 300 K, even if the flake were a perfectly absorbing blackbody.

It is likely that axial oscillations are rapidly thermalized with internal degrees of freedom of the platelet and that $T \approx$ 300 K. Although substantial heating of the illuminated platelet is possible in a high vacuum environment, the low laser powers used in the present experiments would not be expected to raise the internal temperature significantly above 300 K, even if the platelet were a perfectly absorbing blackbody.

The moment of inertia $I_\perp$ can now be determined using Eq. 7.12 with the value

of p_0 extracted from Eq. 7.22. One can then infer the size of the platelet using

$$I_\perp = \int da\, r^2 \rho = m \frac{\int da\, r^2 \rho}{\int da\, \rho} = m \left\langle r_m^2 \right\rangle, \tag{7.23}$$

where ρ is the local two-dimensional mass density of the platelet, $\langle r_m^2 \rangle$ is the mean square size of the platelet weighted by its mass density, and the integrals are over the surface of the platelet.

7.3.3 Reorientation of platelet due to gas friction

Because $\hat{\boldsymbol{z}} \| \boldsymbol{E}_{\mathrm{rf}}$, the z-component of the torque satisfies $N_z = 0$. This simple fact has important consequences for platelet orientation after locking, since torques from the applied electric field cannot counteract torques along $\hat{\boldsymbol{z}}$ arising from friction with residual gas in the vacuum chamber, and consequently the platelet is driven to a state in which $L_z = 0$.

To model this effect I assume:

$$\boldsymbol{N}_g = -\boldsymbol{L}/\tau_g = -\left|L\right| \hat{\boldsymbol{n}}/\tau_g, \tag{7.24}$$

where τ_g is a phenomenological relaxation time. If the platelet is to remain locked in the steady state, however, this torque must be partially counteracted by a torque from the applied rf electric field:

$$-\left|L\right|/\tau_g + N_n = 0. \tag{7.25}$$

Using Eqs. 7.8 and 7.9, one finds:

$$N_\theta = N_n \cot(\theta). \tag{7.26}$$

Because the platelet is locked, only the orientation of $\boldsymbol{L}$, but not its magnitude, can change. Thus:

$$N_\theta = \dot{L}_\theta = |L|\,\dot{\theta} = \frac{1}{\tau_g}\cot(\theta)\,|L|\,. \tag{7.27}$$

This equation has the solution

$$\theta(t) = \cos^{-1}(e^{-t/\tau_g}). \tag{7.28}$$

Thus, in the presence of background gas, one expects the locked platelet to reorient towards $\theta = 90°$, where $\boldsymbol{\omega_n}$ lies in the x-y plane.

7.3.4 Precession of platelet's normal vector about electric field

Equation 7.9 implies that when $\theta \neq 90°$, $N_\phi \neq 0$ and consequently the axis of rotation of the platelet must precess around $\hat{\boldsymbol{z}}$. I assume that this precession is slow compared to the ω_ψ oscillations but rapid compared to the decay in time of θ due to friction. Using Eq. 7.9 with a constant value for θ and an averaged value for $\cos(\psi)$ gives:

$$N_\phi = +\frac{1}{2}p_0 E_0 \cos(\theta)\langle\cos(\psi)\rangle = \dot{L}_\phi = I_\perp \omega_n \dot{\phi}\sin(\theta), \tag{7.29}$$

This equation of motion suggests that the platelet precesses with a characteristic frequency given by:

$$\omega_\phi \equiv \dot{\phi} = \frac{\Omega^2}{\omega_n}\langle\cos(\psi)\rangle\cot(\theta). \tag{7.30}$$

Precession ceases when $\theta \to 90°$ or when the platelet loses lock and $\langle\cos(\psi)\rangle \to 0$. When thermal fluctuations of ψ are small, $\langle\cos(\psi)\rangle \approx 1$ and

$$\omega_\phi \approx \frac{\Omega^2}{\omega_n}\cot(\theta). \tag{7.31}$$

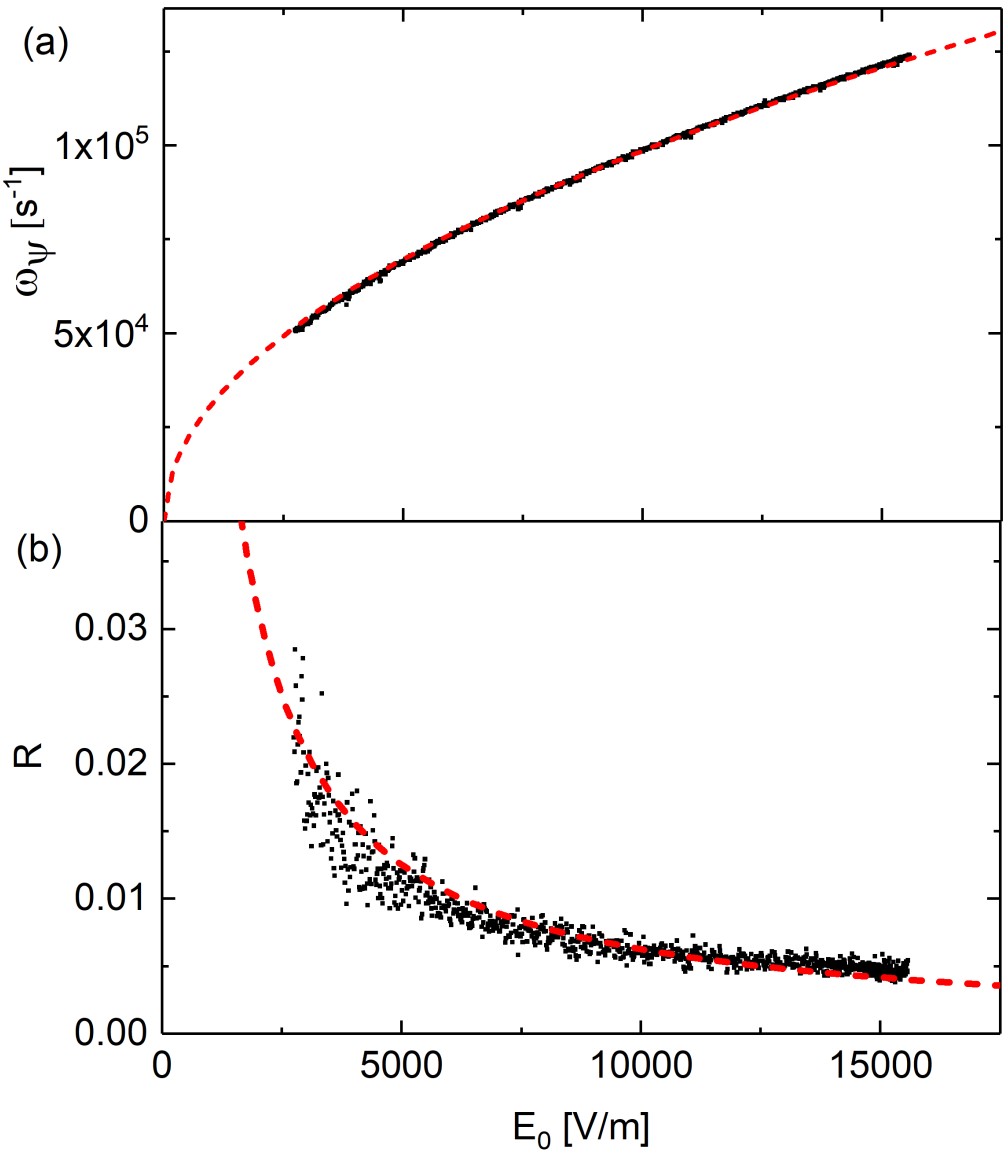

Figure 7.6: (a) Sideband separation frequency ω_ψ as a function of rf electric field E_0, measured after the platelet is locked and oriented at $\theta \cong 90°$. The rf electric field strength is varied slowly (over the course of 3 hours) to keep the platelet stably locked. The square root dependence shows that E_0 is coupling to a permanent electric dipole on the platelet. (b) Sideband power ratio R as a function of E_0 in the same conditions. From this data, the electric dipole moment is $p_0 = 2.6 \times 10^{-22}$ C m (using Eq. 7.22) and the platelet moment of inertia is $I_\perp = 1.4 \times 10^{-28}$ kg m^2 (using Eq. 7.12). Data taken November 14, 2016 on sample 101816B.

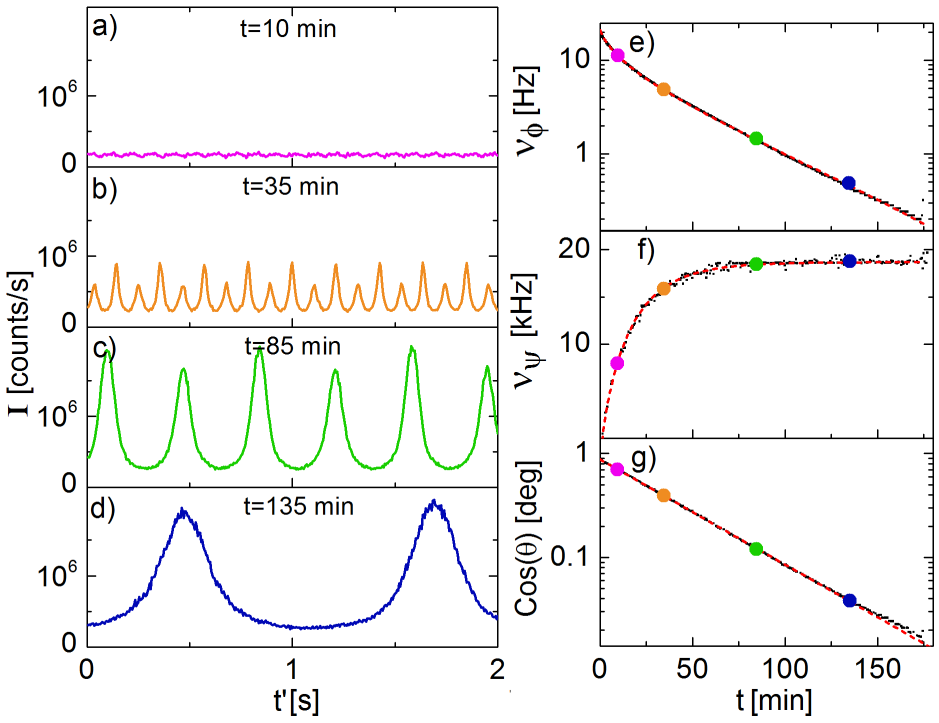

Figure 7.7: (a-d) Time evolution of low frequency light scattering from the platelet versus time t, after locking at time t'=0. Fluctuations in the signal increase in magnitude and become regularly spaced peaks whose period increases with time. Plot colors correspond to colored dots on plots (e-g). (e) Precession frequency ($\nu_\phi = \omega_\phi/(2\pi)$) determined from the lowest Fourier component of the optical data. (f) Sideband frequency ($\nu_\psi = \omega_\psi/(2\pi)$) measured as a function of time after locking. (g) Orientation of the platelet, inferred from measurements of ω_ψ and ω_ϕ and calculated using Eqs. 7.12 and 7.31. Red dashed line is behavior expected from Eq. 7.28. Note log scales in (e) and (g). Data taken May 19, 2016 on sample 051616B. Although the data in this figure is from a different sample than the data in Fig. 8.2, the dynamics are qualitatively similar.

7.4 Comparing the model to observations

I have observed stable locking behavior in 20 individual platelets. Data in Figs. 7.6, 8.2, 9.6(b), and 9.8, as well as in Table 9.6, are from a single platelet (Sample 101816B) on which I collected the most complete set of data, while data in Figs. 7.4, 7.7, and 9.6(a) are from three other platelets (Samples 121115E, 051616B, and 0813116G, respectively).

Figure 7.6 shows data on platelet 101816B taken several hours after locking, when it had completely stabilized. The sideband spacing ω_ψ (see Fig. 7.6(a)) clearly has the square root dependence on E_0 predicted from Eq. 7.12, and it is consequently possible to estimate $p_0 = 2.6 \times 10^{-22}$ C m from the data. Also, the power in the sidebands relative to the harmonics (Fig. 7.6(b)) shows the behavior expected from Eq. 7.22, although thermal fluctuations are likely significant. From this data, I can estimate the moment of inertia $I_\perp = 1.4 \times 10^{-28}$ kg m^2 from Eq. 7.22.

From Eq. 7.23, I can estimate the size of platelet 101816B. The mass of the platelet can be estimated (as in Sec. 2.5) from the Brownian motion of platelet in the trap at relatively high pressure (30 mTorr), assuming its motion is thermalized and T $\approx$ 300 K [8]. For this sample, $m = 3.7 \times 10^{-17}$ kg, which gives $\langle r_m^2 \rangle = 3.7 \times 10^{-12}$ m^2. The actual shape of the platelet is unknown and may be quite irregular. However, if I make the assumption that it is a circular disc of uniform thickness, then its area is $2\pi \langle r_m^2 \rangle = 2.3 \times 10^{-11}$ m^2. Taking the areal density of single-layer graphene to be 7.4×10^{-7}kg m^{-2}, this area is consistent with a platelet of about 2 layers.

The low frequency behavior of the scattered light intensity for platelet 051616B

is shown in Fig. 7.7(a-d). After the platelet is locked and the circularly polarized laser is turned off, regular oscillations appear whose intensity increases and frequency decreases with time. As the predominate frequency of these oscillations approaches ∼1 Hz, the intensity of the signal stabilizes and appears as two peaks with slightly different amplitudes (see Fig. 7.7(b-d)). I interpret this behavior as a consequence of slow precession. The evolution of the precession frequency over time, determined from the frequency of the lowest Fourier component of the intensity data, is plotted in Fig. 7.7(e). Also plotted (see Fig. 7.7(f)) is the data taken simultaneously for the sideband spacing. Using these experimental values of ω_ψ and ω_ϕ, and using Eqs. 7.12 and 7.31, one can determine $\cos(\theta)$ (see Fig. 7.7(g)). The fit to the behavior expected from Eq. 7.28 is excellent.

7.5 Frequency control of locked platelet

While a platelet is frequency-locked, the rotation frequency $\nu_n = \omega_n/(2\pi)$ is equal to the rf drive frequency $\nu_0 = \omega_0/(2\pi)$ (over times longer than the ∼0.1 ms period of the ω_ψ oscillations), so one can directly vary ν_n by varying ν_0.

The rf drive signal is generated by a lock-in amplifier [93], which has the ability to vary the frequency of the output signal with excellent phase continuity. I have found that if I ramp the frequency slowly enough, the platelet will stay locked. In most cases, changing the frequency in steps of 100 Hz with a 250 ms settling time between steps is sufficient to maintain lock. Occasionally a platelet will spontaneously delock when the frequency is first changed. The reason for this

remains to be found. If the platelet is re-locked and the ramp is repeated, it usually succeeds, suggesting that the delocking is not due to some inherent characteristic of the platelet.

The rotation frequency can be varied over more than an order of magnitude. With some samples, I have succeeded in increasing the rotation frequency up to 100 MHz. I have observed the abrupt disappearance of samples spinning at high frequencies (between 20 and 100 MHz), which may be due to decomposition from centrifugal forces. I have not yet undertaken systematic observations of this behavior. I have decreased the frequency to a minimum of about 8 MHz. Particles tend to delock at lower frequencies because the power output of the particular rf amplifier used becomes too low around 4 MHz. With a different amplifier one could likely maintain lock down to 1 MHz. Below 1 MHz, however, the trapping frequency ($\sim$ 10 kHz) applied to the outer trap electrode and the locking drive frequency applied to the inner electrode would likely begin to interfere with each other.

Chapter 8: Estimating nanoplatelet dimensions from optical measurements

8.1 Overview

In Sec. 7.4, I discussed a method of inferring the dimensions of a trapped platelet from its measured mass and moment of inertia. There is considerable uncertainty in these measurements, so it is helpful to have an independent measurement of the dimensions. In this chapter, I describe a way to estimate the platelet's dimensions from the shape of the optical signal seen during low frequency precession. Some material in this chapter was published in Ref. [60].

8.2 Apparatus and theory of scattering

Fig. 7.7 shows an example of the precession signal from platelet 051616B. The double peak behavior observed when $\theta \rightarrow 90°$ is a consequence of the platelet behaving as a slowly precessing mirror that reflects the light from the source to the detector twice each full precession cycle. The intensity peaks occur when the platelet is oriented parallel to the mirroring plane (see Fig. 8.1). The width of the peaks is finite because the size of the platelet is comparable to the wavelength of the light.

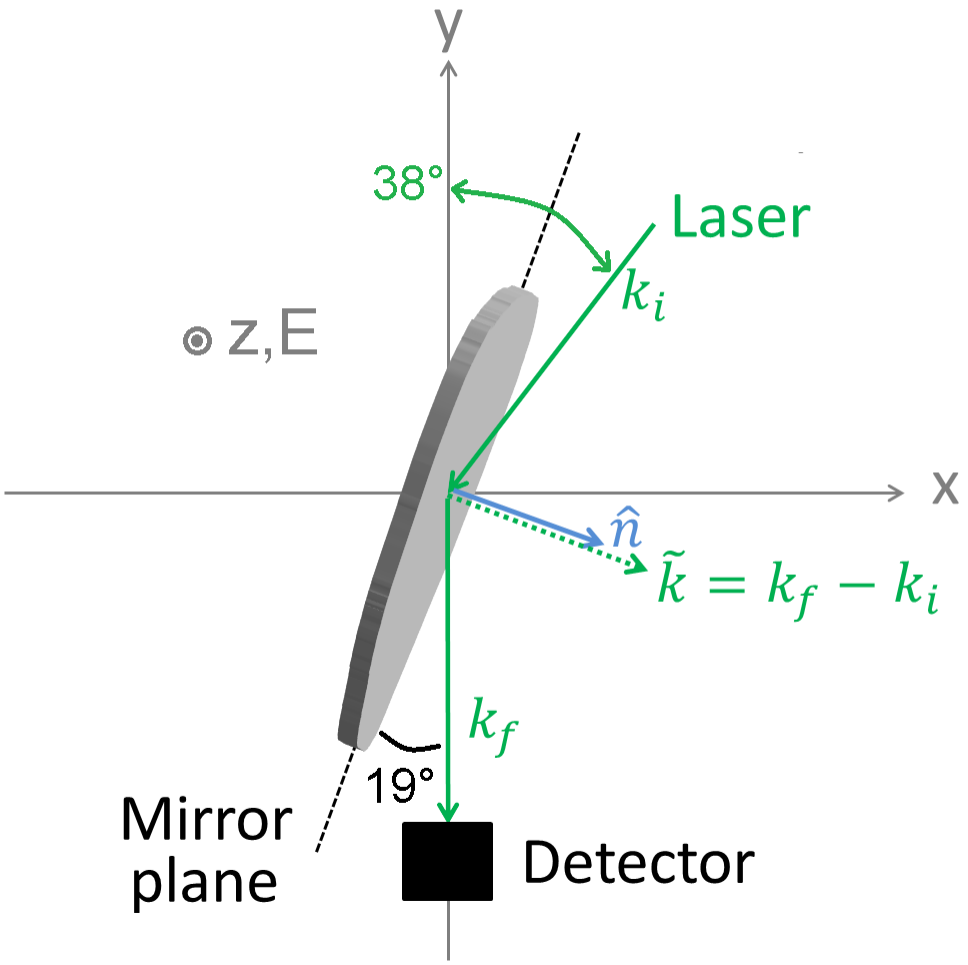

Figure 8.1: Illustration of frequency locked platelet lying in "mirror plane." Top view; z-axis is out of the page. The platelet is shown after it has reoriented so that its normal vector points 90° from the z-axis. The platelet can now rotate with its normal vector sweeping through the xy-plane. When the platelet lies in a particular plane, termed the "mirror plane," scatters the maximum amount of light. This plane is defined by the incident angle of the laser and lies 19° from the y-axis.

As discussed in Sec. 7.3.2, the intensity of light scattered from a typical platelet is dominated by the form factor:

$$F(\tilde{\boldsymbol{k}}) = \left| \int_S d\boldsymbol{r} e^{i\tilde{\boldsymbol{k}}\cdot\boldsymbol{r}} \right|^2, \tag{8.1}$$

where $\tilde{\boldsymbol{k}}$ is the wavevector difference between incident and scattered light and the integral is taken over the surface of the platelet. Low frequency precession occurs around the direction of $\boldsymbol{E}_{\mathrm{rf}}$, assumed to be along the z axis. Assuming perfect alignment of the trap electrodes, $\tilde{\boldsymbol{k}} \perp \hat{\boldsymbol{z}}$, and thus $\tilde{k}_z = 0$. As a consequence of time reversal symmetry, the form factor $F(\tilde{\boldsymbol{k}})$ obeys $F(\tilde{\boldsymbol{k}}) = F(-\tilde{\boldsymbol{k}})$, so 180° rotations of the platelet around the z-axis leave the form factor unchanged. This symmetry is not exact in the data shown in Fig. 8.2 (the intensity peaks are not of equal amplitudes), probably because of small deviations from orthogonality of $\tilde{\boldsymbol{k}}$ and $\boldsymbol{E}_{\mathrm{rf}}$.

For low frequency data, the rapid time dependence of $I(t)$ due to rotation around $\hat{\boldsymbol{n}}$ is averaged out, and the observed intensity only depends on the angle ζ between $\hat{\boldsymbol{n}}$ and $\tilde{\boldsymbol{k}}$. (As usual, $\hat{\boldsymbol{n}}$ is the normal to the platelet.) While the nanoplatelet is likely to be irregularly shaped, measurement of the angular dependence of scattering provides an estimate of its size [92][94][95]. If I assume that the nanoplatelet is a circular disk with diameter $2r_0$, then [96]:

$$F(k_\parallel, r_0) = (\pi r_0^2)^2 \left\{ \frac{2J_1(k_\parallel r_0)}{k_\parallel r_0} \right\}^2, \tag{8.2}$$

where J_1 is the first order Bessel function, and $k_\parallel = |\tilde{\boldsymbol{k}}_\parallel|$ is the component of $\tilde{\boldsymbol{k}}$ in the plane of the disk:

$$k_\parallel = \frac{4\pi}{\lambda_0} \sin\left(\frac{\gamma}{2}\right) \sin(\zeta). \tag{8.3}$$

$\lambda_0 = 532$ nm is the wavelength of the incident light and γ is the angle through which the light scatters, which is 38° in the experiments (see Figs. 2.5 and 8.1).

Since the platelets used in these experiments are likely not circular, I consider the form factor for elliptical nanoplatelets, which can be readily obtained from the result for circular disks via a coordinate transformation. For an ellipse with semiminor and semimajor axes a and b, the following substitutions into Eq. 8.2 yield the appropriate expression:

$$r_0^2 \to ab \tag{8.4}$$

and:

$$k_\parallel r_0 \to k_\parallel \sqrt{\frac{1}{2}(a^2+b^2) + \frac{1}{2}(a^2-b^2)\cos(2\Phi)}, \tag{8.5}$$

where Φ is the angle between $\tilde{\boldsymbol{k}}_\parallel$ and the major axis of the ellipse. Because of the rapid rotation, averaging over Φ yields the appropriate result for interpreting the low frequency optical signal.

8.3 Experimental measurement of dimensions

Using this elliptical approximation, I fit the experimental peak amplitudes in Fig. 8.2 to determine dimensions of the platelet. I performed a fit, using *Mathematica*, of Eq. 8.2, with the substitution for r_0 as shown in Eq. 8.5. The function is averaged over one full in-plane rotation of the platelet (*i.e.* $0 < \Phi < 2\pi$) during each iteration of the fitting algorithm. Due to the small asymmetry of the peaks, I fit only half the period of precession. From the best fit curve, I found $a = 290$ nm and $b = 790$ nm for the semiminor and semimajor axes, respectively.

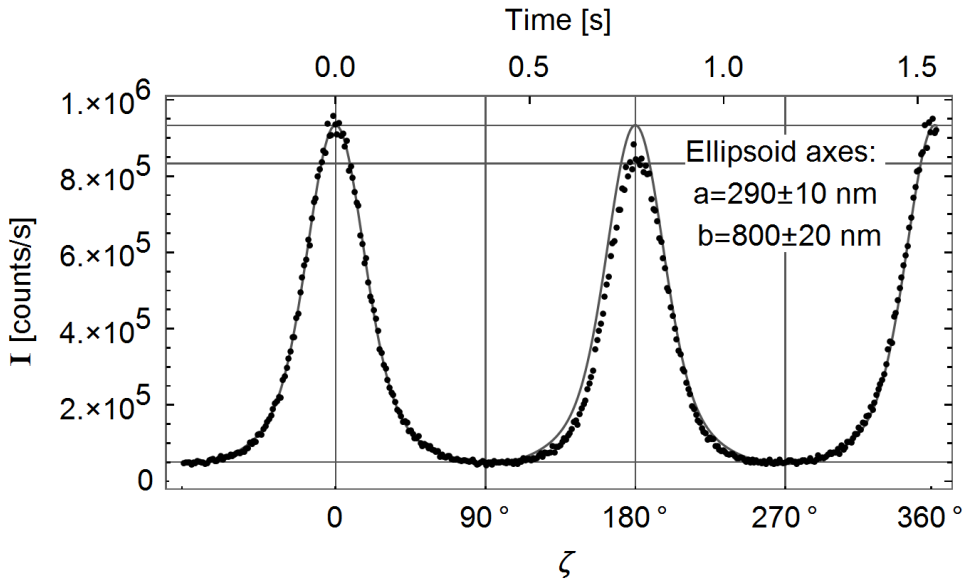

Figure 8.2: Scattered light signal I versus angle ζ for one period of precession. $\zeta = 0$ corresponds to the orientation where the platelet is in the mirroring plane and the signal is maximized. Data for one half-period ($-90° < \zeta < 90°$) is fit to Eqs. 8.2 and 8.5 in order to approximate the dimensions of the platelet. The best-fit curve and derived values of the semiminor and semimajor axes a and b are shown. The fit is excellent over the first half-period but shows the small asymmetry in the second peak. Data taken Nov. 10, 2016 on sample 101816B.

These dimensions give a platelet area of approximately $\pi ab = 7.2 \times 10^{-13}$ m^2, which implies that the platelet has about 70 layers. This area is significantly smaller than that obtained using the measured moment of inertia in Sec. 7.4, and the likely uncertainty of around 30% in the mass does not account for the discrepancy. One possible cause of the discrepancy is that I have thus far assumed that only the size of the platelet contributes to the width of the scattered light peaks. In fact, there are two likely sources of systematic error that could cause added broadening of the peaks, leading to underestimation of the areal dimensions of the platelet. First, the above calculation assumed that the acceptance angle of the lens is infinitely small. I estimate that accounting for the acceptance angle will increase the semimajor axis b by a factor of approximately 1.3. A second, and probably more important, potential source of error in the above calculations is that any high frequency precession of the instantaneous axis of rotation was neglected, as were flexural modes of the membrane. Rapid wobbling or bending of the membrane in this manner would broaden the peaks and lead to an underestimation of its dimensions in the previous calculation.

Chapter 9: Measurements of magnetism in levitated nanoplatelets

9.1 Overview

After the frequency-locked platelet has reoriented so that its normal vector lies in the horizontal plane, it is extremely sensitive to applied torques. I found that the residual slow dynamics of the platelet's normal vector are controlled by an applied magnetic field, providing an excellent opportunity to study magnetism in graphene. In this chapter, I present data on the platelet's interaction with a magnetic field, as well as a simple model that describes these observations. From the data and model, I infer both a diamagnetic polarizability and a magnetic moment proportional to the frequency of rotation, which I compare to theoretical values. Some material in this chapter was published in Ref. [60].

9.2 Observation of orientational trapping

In the course of establishing the frequency lock (see Ch. 6, 7), the platelet is exposed to circularly polarized light (CPL), causing its normal vector to tilt toward the vertical. Upon locking, the platelet begins to precess about the vertical rf electric field. The CPL is blocked and the platelet's precession frequency slows

while its normal vector tilts toward the horizontal plane; *i.e.*, $\theta \to 90°$. This process is described in detail and analyzed mathematically in Ch. 7.

Fig. 9.1 shows the scattered light signal at several points during this process. At this point, no external magnetic field has been applied to the system, although an ambient magnetic field (see Sec. 9.3) is present in the lab. The reader may recall from Ch. 7 that the platelet will scatter a maximum amount of light when it lies in a particular plane that I refer to as the "mirror plane". Parts (a) and (b) show the characteristic dual-peaked signal as the platelet precesses, passing through the mirror plane twice per revolution. The slight height difference in the peaks may be due to one side of the likely-multilayer platelet being rougher than the other; it may also be due to a deviation from orthogonality between the electric field and the plane of propagation of the laser, so that the platelet is not quite precessing around the "vertical".

Comparing Fig. 9.1(b-c), however, one can see that the signal changes and can no longer be interpreted as precession; instead, it implies that the platelet is oscillating about a fixed orientation. In (c), the period of oscillation is approximately 4 seconds. The "M" shaped double peak represents the platelet passing through one of its two "mirror planes", reversing direction, and passing through the same mirror plane again. The two remaining peaks represent the platelet passing through the second mirror plane 180° away, rotating approximately 90° further, to a point of minimum reflection, then reversing direction and passing through the second mirror plane again.

In Fig. 9.1(d-e), the amplitude of the platelet's slow oscillation decreases and

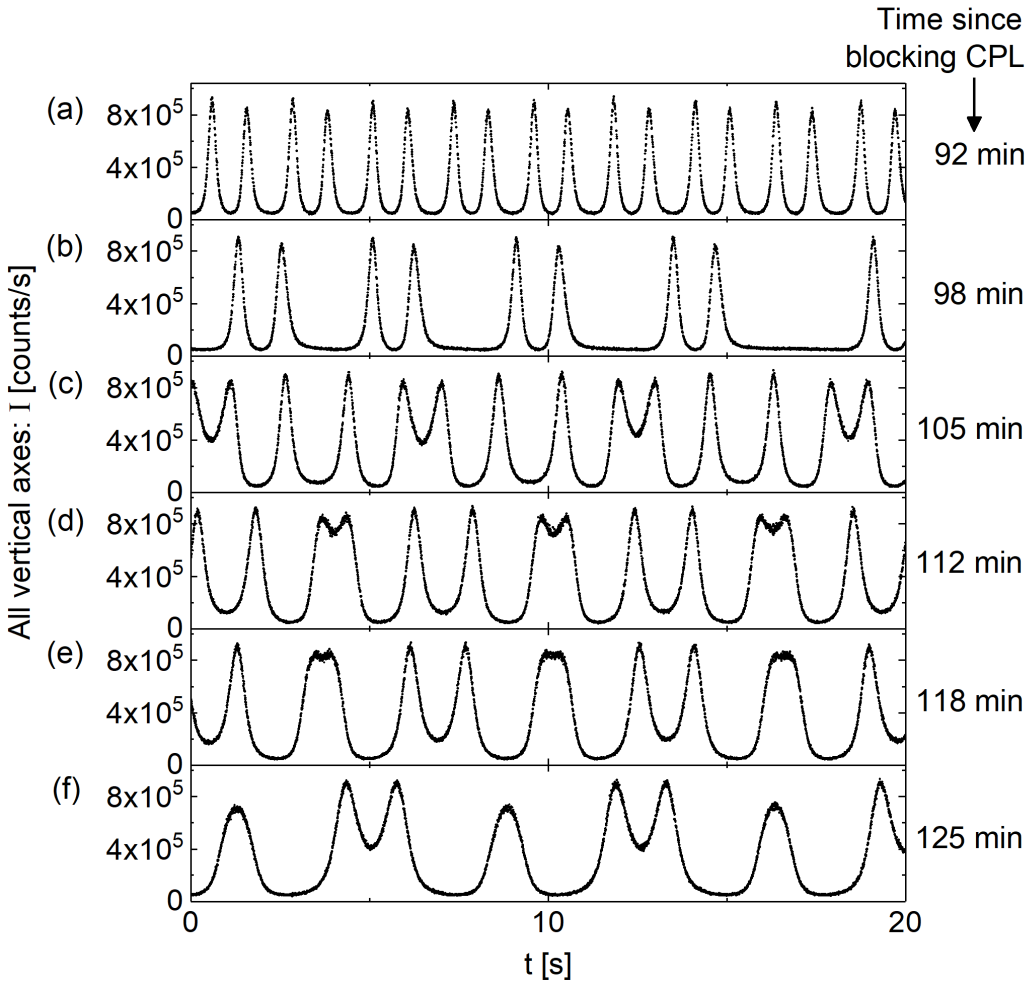

Figure 9.1: Scattered light signal I versus time t showing "angle-trapping" of a frequency-locked graphene platelet. (a-b) show the platelet precessing, while in (c-f) the platelet has stopped precessing and its angle of orientation is oscillating about a fixed point. Dotted lines are aligned with the maximum and minimum scattering intensities. The two sides of the platelet have slightly different maximum intensities. Data taken Oct. 31, 2016 on sample 101816B.

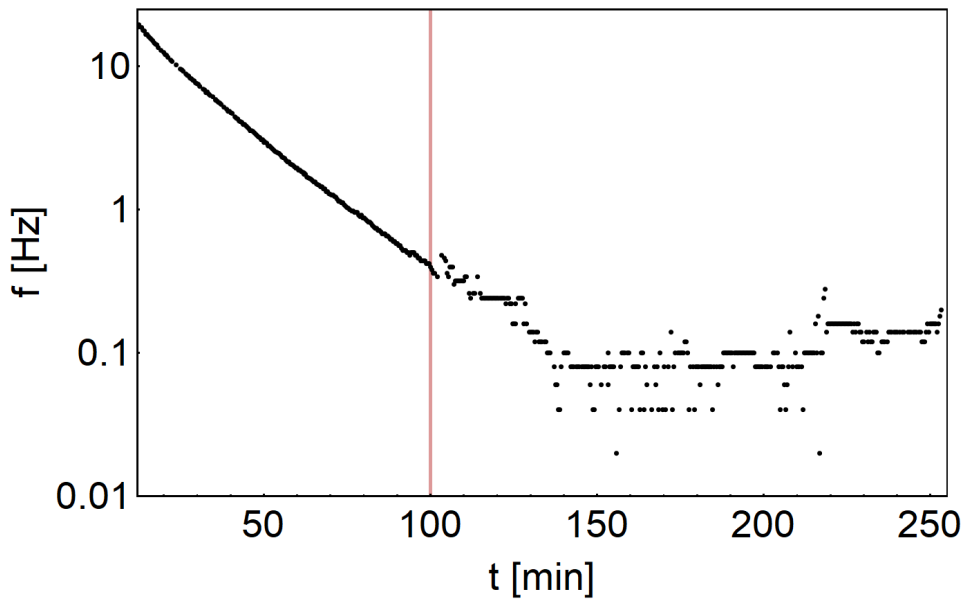

Figure 9.2: Frequency f of the scattered light signal as a function of time t after CPL is blocked. The frequency is calculated from the data shown in the previous figure. The red line shows the time when the platelet ceases precession and becomes "angle-trapped." The oscillation frequency eventually stabilizes around 0.6 Hz. Data taken Oct. 31, 2016 on sample 101816B.

its period lengthens. In (f), the period of oscillation is approximately 7 seconds. The two tall peaks represent the platelet passing through one of its two "mirror planes", reversing direction, and passing through the same mirror plane again. The shorter single peak represents the particle approaching the second mirror plane but reversing direction before it reaches that plane.

If left for several hours after becoming angle-trapped, the frequency of oscillations eventually approaches a fairly constant value. The frequency of the oscillations for sample 101816B, depicted in Fig. 9.1, is plotted in Fig. 9.2. For this sample, the frequency stabilized around 0.6 Hz. Typical terminal frequencies (for zero applied

magnetic field) range from 0.1 to 1 Hz.

As the platelet appears to be behaving as a circular pendulum, a logical conclusion is that it is confined by an external field; an obvious candidate is the ambient magnetic field.

9.3 Apparatus for application of magnetic field

There are several possible sources of ambient magnetic field, including a cathode gauge and an ion pump on the same table as the experiment, as well as the Earth's field. Rough measurements of the ambient magnetic field surrounding the trap, using a handheld gaussmeter, yielded a net magnetic field of no more than 0.2 mT in any direction. To test the hypothesis that the angle-trapping was caused by a magnetic field, I constructed an apparatus to apply a magnetic field of variable direction and magnitude.

Two identical magnet posts are placed on rotation stages on either side of the vacuum chamber, about 9 cm from the trap center (Fig. 9.3). Each post contains four neodymium magnets, disk-shaped with diameter 38 mm and thickness 12 mm, with their magnetic moments oriented horizontally (see Fig. 9.3(a)). Each individual magnet creates a field of about 2.8 mT at a distance of 9 cm.

The posts can be rotated to make the field point in any direction in the horizontal plane. The field at the trap center can be calculated (see Fig. 9.4). Jacob Murphy, an undergraduate student, confirmed this prediction by moving the posts away from the system and measuring the field at the location where the trap center

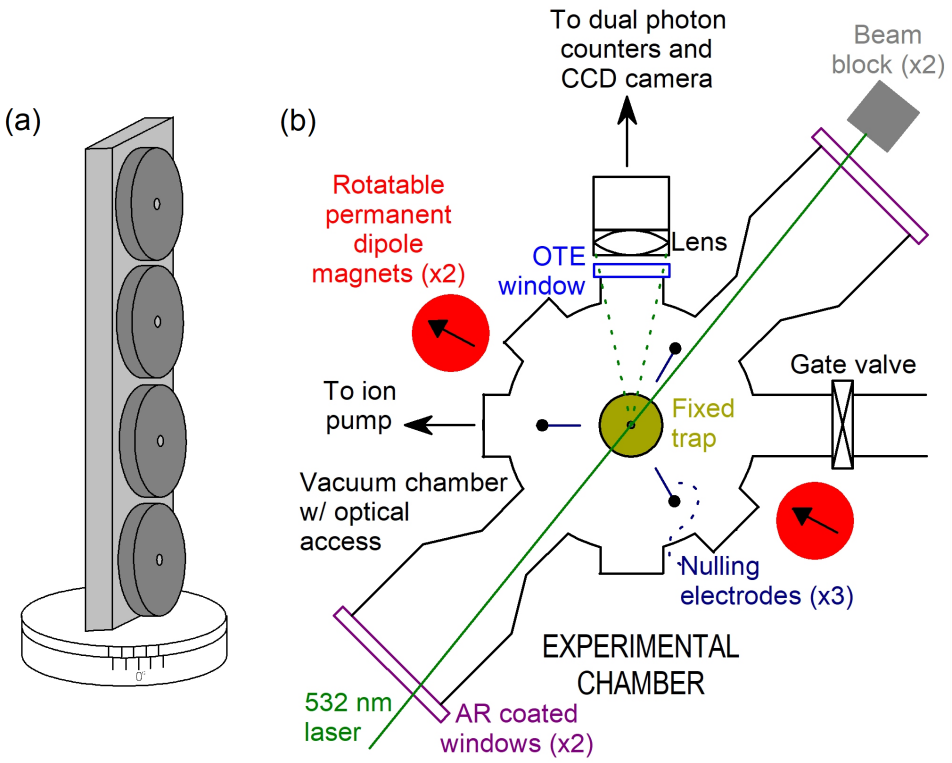

Figure 9.3: (a) Diagram of a single magnet post. An aluminum bar, mounted on a 360° rotation stage, holds four permanent magnets. Two identical posts are placed on opposite sides of the vacuum chamber, about 9 cm from the trap center. (b) Experimental chamber with magnet posts placed outside, each about 9 cm from trap center.

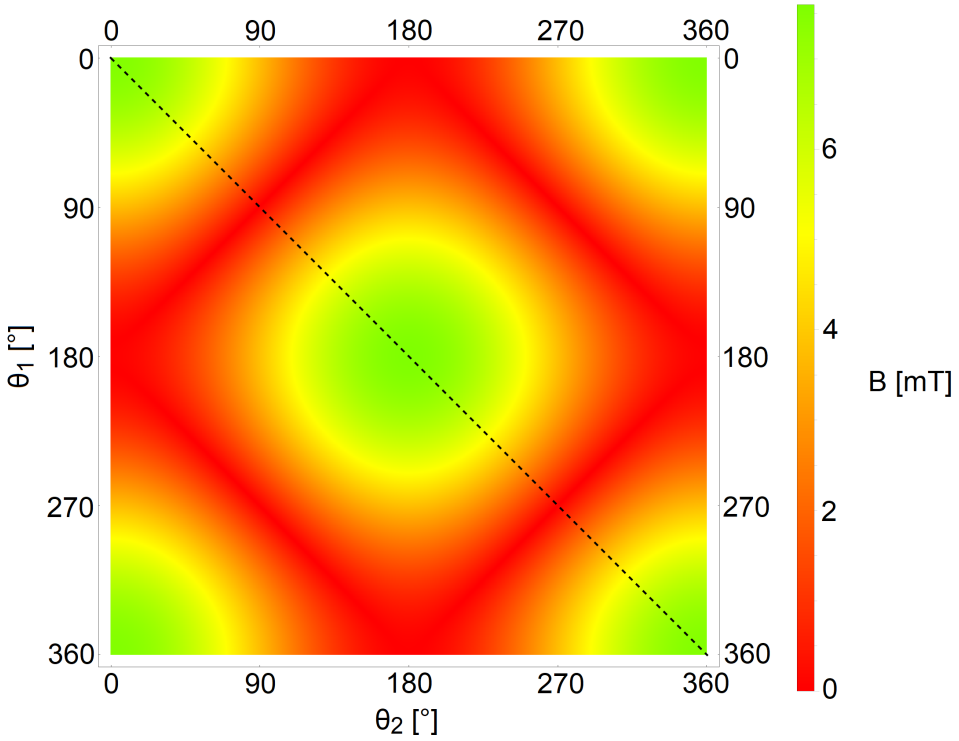

Figure 9.4: False color plot of magnetic field B versus Θ_1 and Θ_2, the angles of rotation of each of the two magnet posts. The color legend shows the field magnitude in mT. The smooth color plot was produced by fitting a discrete set of data points. Maximum field strength is achieved with both magnets pointed in the same direction. If the magnets are rotated in tandem (following the dotted line in the figure), the field magnitude varies from 4.2-7.5 mT. Data taken by Jacob Murphy.

would be. The field is zero (with a margin of error of about 0.1 mT due to slight differences in strength of the eight permanent magnets) when the posts are turned so that the magnetic moments point in opposite directions. The field reaches a maximum when the magnets are pointed in the same direction. If the magnets are rotated in tandem, the field magnitude varies from 4.2-7.5 mT (see Fig. 9.4).

9.4 Observations of platelet interaction with magnetic field

In this section, I examine the orientation of the platelet's normal vector in the xy-plane as a function of the direction of the magnetic field $\boldsymbol{B}$ created by the magnet posts. As the net magnetic field is increased, the frequency of oscillation of the scattered light signal shown in Fig. 9.1 increases, suggesting that the magnetic field is indeed providing a confining potential for the platelet.

To deduce the orientation of the platelet with respect to the magnetic field, I slowly rotated the magnetic field through a full 360° horizontal rotation, after the platelet has been frequency-locked and its normal vector has been allowed to reorient fully into the xy-plane. I recorded the average intensity of scattered light during the rotation.

In Fig. 9.5, the average intensity of light scattered from a trapped platelet (Sample 081316G) is plotted as a function of the direction of $\boldsymbol{B}$ in the xy-plane. For this data, the rf drive frequency was set at $\nu_0 = 20$ MHz. A single data point represents the intensity averaged over 10 minutes, while the error bars represent the standard deviation of the intensity during this period. Two maxima occur during

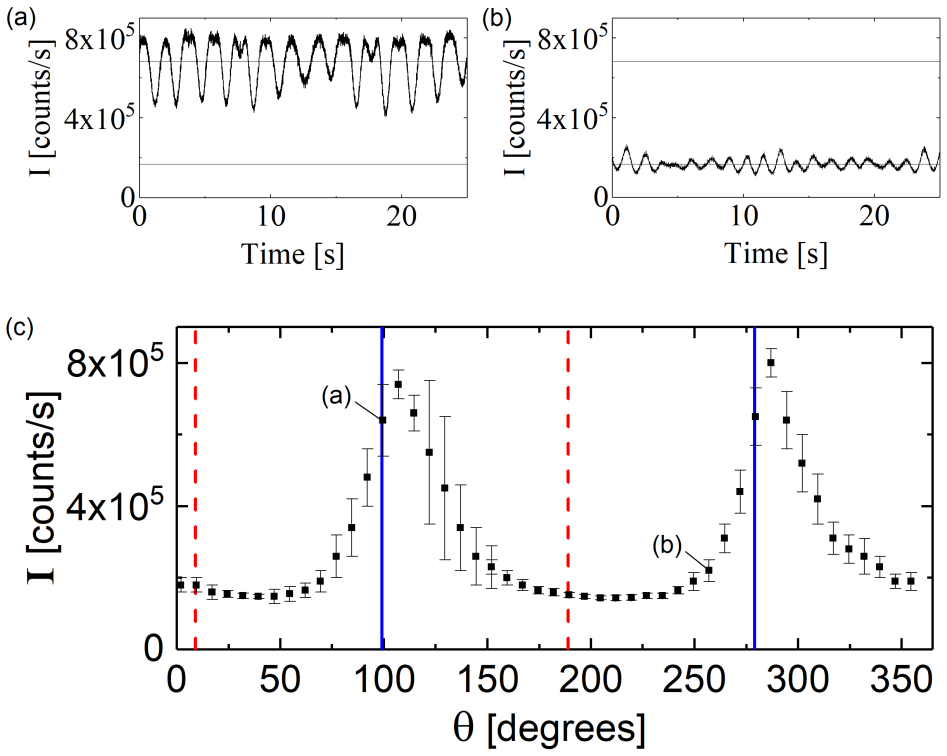

Figure 9.5: (a) Intensity of scattered light I versus time t, over about 25 s, with magnet angle $\theta = 100°$. (b) Intensity of scattered light I versus time t, over about 25 s, with magnet angle $\theta = 280°$. (c) I versus θ, showing control of trapped platelet orientation by rotating the direction of the applied magnetic field. A single data point represents I averaged over 10 minutes, while the error bars represent the standard deviation of the intensity during this period. Drive frequency was set at $\nu_0 = \nu_n = \omega_n/(2\pi) = 20$ MHz. Field magnitude at the trap center varied from 4.5-7.2 mT as the dipole magnets were rotated. The zero of the magnetic field angle is defined such that the magnets are pointing collinearly (as shown in Fig. 9.3(b). As the magnets are rotated clockwise in tandem, the magnetic field rotates *counter*-clockwise. Orientations with a maximum intensity occur when B is parallel to the mirroring plane (solid vertical lines). Data taken August 2016 on sample 081316G.

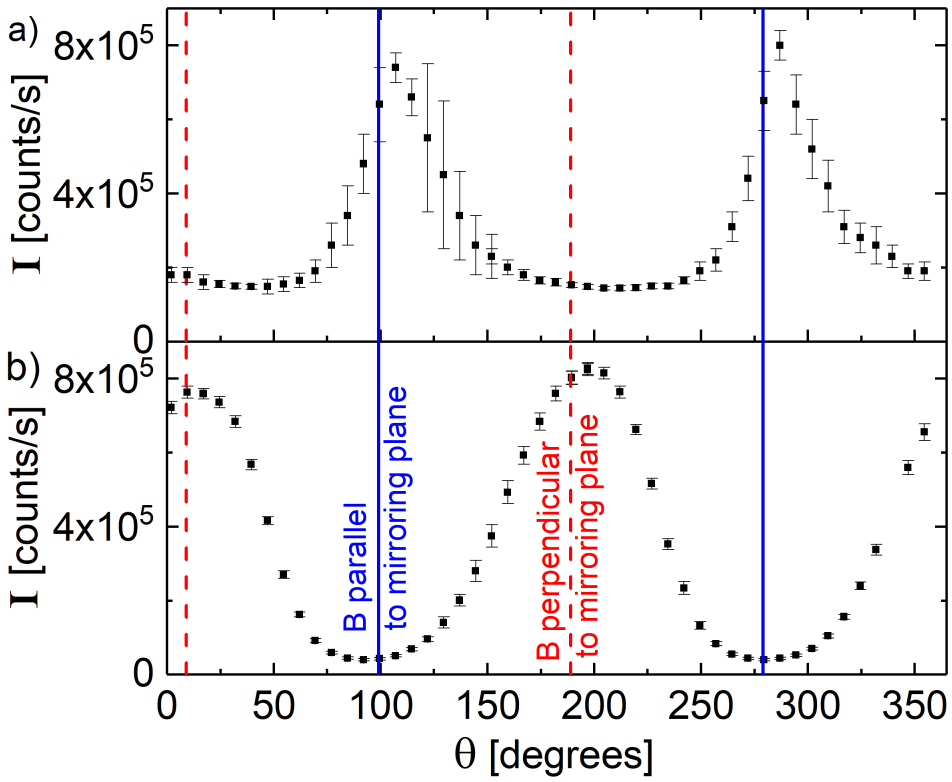

Figure 9.6: Plot of scattered light signal I versus magnetic field angle θ demonstrating control of the orientation of the trapped platelet. (a) Data reproduced from Fig. 9.5. (b) Data from Sample 101816B, with $\nu_0 = 40$ MHz. Maximum intensity occurs when B is perpendicular to the mirroring plane (dashed vertical lines). Data in plots (a) and (b) is taken from different samples; however, I have observed the transition from parallel to perpendicular alignment in a single platelet. Data taken Nov. 9, 2016 on sample 101816B.

a full 360° rotation of the magnets, indicating that the platelet has also rotated 360°. Large error bars on some data points indicate that the amplitude of the platelet's oscillations is large. The variation in size of the error bars is related to the variation in magnetic field strength as the magnets are rotated; a weaker magnetic field provides weaker confinement, resulting in larger oscillations. Fig. 9.6 compares the above data with an analogous data set taken at a higher rf drive frequency ($\nu_0 = 40$ MHz) on Sample 101816B.

The platelet assumes two distinct orientations with respect to the direction of $\boldsymbol{B}$, depending on its rotation frequency. Fig. 9.6(a) shows that at relatively low ν_n, two intensity maxima occur when $\boldsymbol{B}$ is in the mirroring plane (see Fig. 9.3(b)), implying that the platelet is aligned such that $\boldsymbol{B}$ lies in the plane of the platelet. This behavior is consistent with a diamagnetic response of a 2D platelet[97][98].

Fig. 9.6(b) shows that at higher ν_n, the two intensity maxima appear when $\boldsymbol{B}$ is *normal* to the mirroring plane, implying that the platelet is aligning normal to $\boldsymbol{B}$. This behavior is to be expected if the platelet's magnetic moment arises not from diamagnetism but from its rapid rotation or a magnetic moment perpendicular to the flake.

9.5 Model of nanoplatelet interactions with magnetic field

In order to explain these observations, I present a model to account for the two distinct responses of the platelet to the magnetic field. First, I consider the diamagnetic response of a 2D platelet. The platelet can experience a torque from a

magnetic field if it has an anisotropic magnetic polarizability. For a thin platelet, I assume that the induced dipole is perpendicular to the platelet plane and proportional to the component of $\boldsymbol{B}$ perpendicular to the plane:

$$\boldsymbol{\mu}_{dia} = \alpha_{dia}\hat{\boldsymbol{n}}\left(\hat{\boldsymbol{n}} \cdot \boldsymbol{B}\right), \tag{9.1}$$

where α_{dia} is a magnetic polarizability. Note that if $\alpha_{dia} < 0$, the induced dipole points away from $\boldsymbol{B}$ as would be expected for diamagnetic materials [98][99].

Second, I consider the magnetic moment $\boldsymbol{\mu}_{rot}$ created by the charged nanoplatelet's rapid rotation. If the magnetic moment arises from the current created by the charge fixed on the spinning platelet, then:

$$\boldsymbol{\mu}_{rot} = \alpha_{rot}\boldsymbol{\omega} = \alpha_{rot}\omega_n\hat{\boldsymbol{n}}. \tag{9.2}$$

where α_{rot} is a coefficient related to the rotation of the platelet. Assuming that $\theta \cong 90°$ and $\boldsymbol{B} = B_0\hat{\boldsymbol{x}}$ gives:

$$\boldsymbol{N} = \boldsymbol{\mu} \times \boldsymbol{B} = B_0 \begin{vmatrix} \hat{\boldsymbol{\theta}} & \hat{\boldsymbol{\phi}} & \hat{\boldsymbol{n}} \\ 0 & 0 & \alpha_{dia}B_0\cos(\phi) + \alpha_{rot}\omega_n \\ 0 & -\sin(\phi) & \cos(\phi) \end{vmatrix}, \tag{9.3}$$

with $\boldsymbol{\mu} = \boldsymbol{\mu}_{dia} + \boldsymbol{\mu}_{rot}$. Thus:

$$N_\theta = -I_\perp\omega_n\dot{\theta}' = \alpha_{dia}B_0^2\sin(\phi)\cos(\phi) + \alpha_{rot}B_0\omega_n\sin(\phi), \tag{9.4}$$

where $\theta' = 90° - \theta$. For small θ' I use Eq. 7.30 with $\langle\cos(\psi)\rangle \cong 1$ to get:

$$\dot{\phi} = \frac{\Omega^2}{\omega_n}\theta'. \tag{9.5}$$

Consequently:

$$\ddot{\phi} = -\frac{\Omega^2}{I_\perp \omega_n^2}\left\{B_0^2 \alpha_{dia}\sin(\phi)\cos(\phi) + B_0 \omega_n \alpha_{rot}\sin(\phi)\right\}. \tag{9.6}$$

When the second term in Eq. 9.6 is neglected, the locations of stable points of oscillation depend on the sign of α_{dia}. When $\alpha_{dia} < 0$, they are at $\phi = \pm 90°$, and for small amplitudes the oscillations have angular velocity:

$$\omega_{dia} = \sqrt{\frac{\Omega^2 B_0^2 \left|\alpha_{dia}\right|}{I_\perp \omega_n^2}}. \tag{9.7}$$

When the first term is neglected, stable oscillations occur near $\phi = 0$. For small ϕ, the oscillations have angular velocity:

$$\omega_{rot} = \sqrt{\frac{\Omega^2 B_0 \alpha_{rot}}{I_\perp \omega_n}}. \tag{9.8}$$

The expected oscillation frequencies given in Eqs. 9.7 and 9.8 have different functional dependences on B_0 and ω_n which allow us to distinguish the mechanisms with data. Another mechanism that can introduce torque and trap the orientation of the flake comes from the rotation of the Earth. For this mechanism trapping oscillation angular velocities will be approximately equal to $\Omega\sqrt{2\pi/\omega_n D}$, where D is the period of the Earth's rotation. For my experiments, this would lead to periods of order 100 sec., much slower than what arises from magnetic fields.

When both terms in Eq. 9.6 are comparable, one must solve:

$$\frac{\ddot{\phi}}{\omega_{dia}^2} = f(\phi) = \sin(\phi)\cos(\phi) - \beta\sin(\phi), \tag{9.9}$$

where $\beta \equiv \omega_{rot}^2/\omega_{dia}^2$. Solutions are stationary when the right hand side is zero, which implies:

$$\sin(\phi) = 0 \quad \text{or} \quad \cos(\phi) = \beta. \tag{9.10}$$

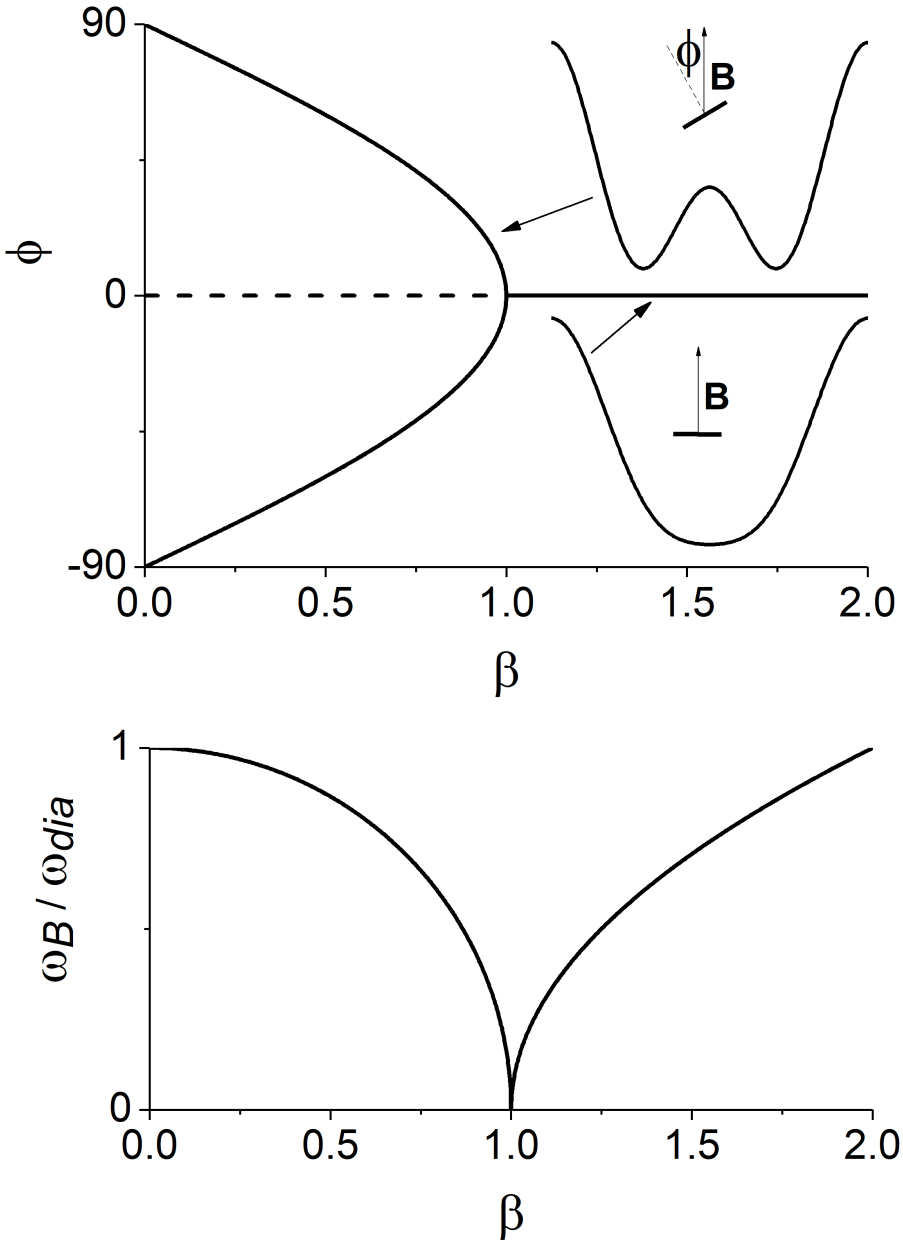

Figure 9.7: (a) Predicted orientation angles ϕ of the platelet in diamagnetism-dominant ($\beta < 1$) and rotation-dominant ($\beta > 1$) regimes. (b) Predicted dependence of the ratio ω_B/ω_{dia} in each regime (see Eqs. 9.12 and 9.13).

The frequency of small oscillations can be found from the first derivative of $f(\phi)$ at the stationary angles:

$$f'\left(\sin(\theta)=0\right)=1\pm\beta \qquad \text{and}: \qquad f'\left(\cos(\phi)=\beta\right)=\beta^2-1. \tag{9.11}$$

Thus, the angular velocities for small oscillations, ω_B, are

$$\omega_B=\omega_{dia}\sqrt{1-\beta^2} \qquad (\beta<1) \tag{9.12}$$

and

$$\omega_B=\omega_{dia}\sqrt{\beta-1} \qquad (\beta\geq 1)\,. \tag{9.13}$$

These solutions are plotted in Fig. 9.7(a). Since the confining potential is not simple harmonic, deviations from Eqs. 9.12 and 9.13 may be substantial, especially near $\beta=1$.

9.6 Estimates of the nanoplatelet magnetic properties

I tested the above model, using Sample 101816B, by varying the rf drive frequency ν_0 (slowly enough so that the platelet remained locked and $\nu_0=\nu_n$) and observing the oscillation frequency $\nu_B=\omega_B/(2\pi)$. The external magnetic field was held constant at $B_0=7$ mT. In Fig. 9.8, I plot the product $\nu_B\nu_0$. In the range 10 MHz $<\nu_0<$ 25 MHz, the data can be fit fairly well by Eq. 9.12, while some significant discrepancies are obvious at higher ν_0.

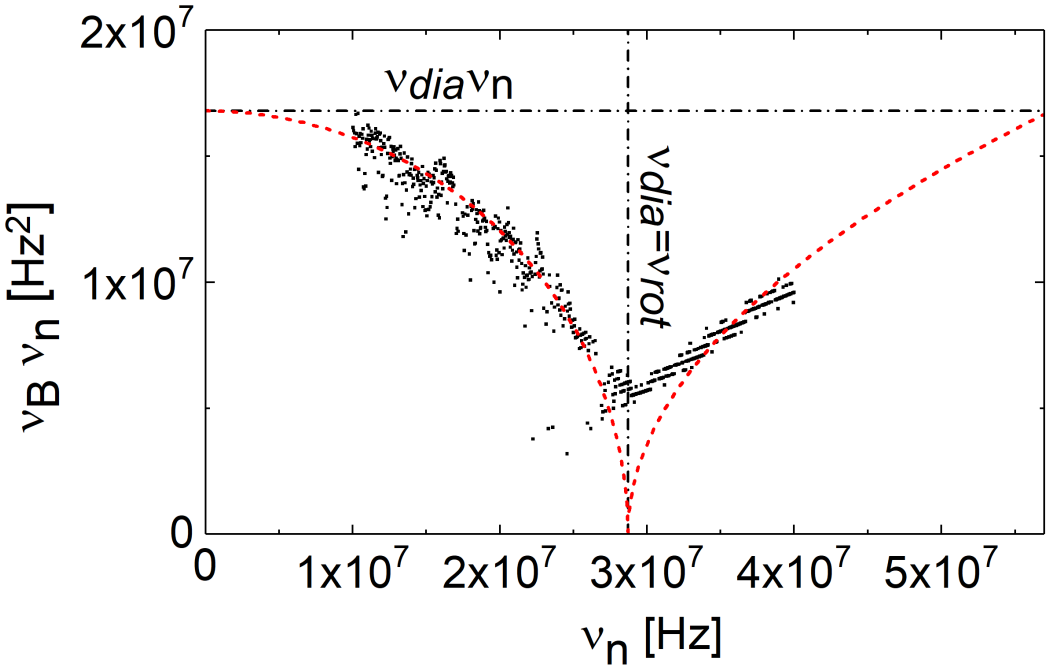

Figure 9.8: Dots represent measurements of the slow oscillation frequency of a spinning platelet, as the rf drive frequency $\nu_0 = \nu_n = \omega_n/(2\pi)$ is varied (at a rate of 400 Hz sec^{-1}) and the oscillation frequency $\nu_B = \omega_B/(2\pi)$ is measured. For this data, the external magnets are fixed at an angle of $+28°$ from the zero defined in Fig. 9.6. The resulting field strength near the platelet is $B \approx 7$ mT. Best-fit curves (red dashed lines) correspond to Eqs. 9.12 and 9.13. The dash-dotted horizontal line marks the constant value of the product $\nu_{dia}\nu_0 = 1.68 \times 10^7$ Hz^2. The dash-dotted vertical line marks the drive frequency $\nu_0 = 2.87 \times 10^7$ Hz at which the contributions to the oscillation frequency from diamagnetism and rotation are equal: $\nu_{rot} = \nu_{dia} = 0.58$ Hz. Deviations of data from theory near the vertical line are to be expected because the potential providing orientational confinement is not simple harmonic near $\beta = 1$ (see Fig. 9.7). Data taken Nov. 2-4, 2016 on sample 101816B.

Table 9.1: Calculated quantities for Sample 101816B. *Top section:* q/m is derived from Eq. 2.3. The measurement of m is described in Sec. 2.5. Ω is derived from Eq. 7.12, measured after platelet has fully reoriented and $\sin(\theta) \approx 1$. p_0 comes from fitting data in Fig. 7.6(b) to Eq. 7.22. $I_\perp$ comes from fitting data in Fig. 7.6(a) to Eq. 7.12. *Middle section:* α_{dia} is derived from Eq. 9.7. α_{rot} is derived from Eq. 9.8. g is derived from Eq. 9.19. *Bottom section:* The platelet area and layer number are estimated in Sec. 7.4. For the last two quantities, I assume that the platelet is circular and uniform in thickness; however, the actual shape is unknown.

Quantity	Value	
q/m	6.1	$\mathrm{C\,kg^{-1}}$
m	3.7×10^{-17}	kg
Ω	1.27×10^{5}	$\mathrm{rad\,sec^{-1}}$
p_0	2.6×10^{-22}	C m
$I_\perp$	1.4×10^{-28}	$\mathrm{kg\,m^2}$
α_{dia}	-7.6×10^{-17}	$\mathrm{J\,T^{-2}}$
α_{rot}	2.9×10^{-27}	$\mathrm{J\,s\,T^{-1}}$
g	7.6	
Area	2.3×10^{-11}	$\mathrm{m^2}$
Number of layers	≈ 2	

9.6.1 Diamagnetic polarizability

I first examine the data in the regime where the diamagnetic contribution is dominant, where $\nu_0 \to 0$. The fit in Fig. 9.8 suggests that in this limit, $\nu_B \nu_0 \to 1.68 \times 10^7$ Hz^2. In the same limit, Eq. 9.12 becomes $\omega_B = \omega_{dia}$, and I can use Eq. 9.7 to obtain $\alpha_{dia} = -7.6 \times 10^{-17}$ J T^{-2}.

This result can be compared with the "magnetic shield" model for graphene diamagnetism developed by Koshino *et. al.* [100]. In this theory, diamagnetic currents attenuate a magnetic field perpendicular to the platelet by a constant factor $1 - f$, where:

$$f = \frac{2\pi g_v g_s e^2 \nu_f}{16 \hbar c^2}. \tag{9.14}$$

g_v and g_s are the valley and spin degeneracies respectively and ν_f is the constant Fermi velocity for graphene. For $g_v = g_s = 2$ and $\nu_f / c \approx 10^{-3}$, $f = 4 \times 10^{-5}$. For a circular disk of such a material[101],

$$\alpha_{dia} = -\frac{8}{3\mu_0} r^3 f, \tag{9.15}$$

where r is the disc radius and $\mu_0 = 4\pi \times 10^7$ H m^{-1}. Exact quantitative agreement with this theory is not expected, for two reasons. First, the experimental sample most likely contains more than a single layer of graphene; second, Koshino's theory assumes that the material is at the Dirac point, which may be untrue for this platelet because it has a net charge.

Most of my calculations have been made without assumptions as to the shape of the particle; however, if I assume that it is a circular disc, then using the mean

square size of the platelet calculated from the moment of inertia in Sec. 7.4, with $r^3 \to (2\langle r_m^2 \rangle)^{3/2}$, Koshino's formula gives $\alpha_{dia} = -1.7 \times 10^{-15} \mathrm{J\,T^{-2}}$, about 20 times larger in magnitude than the measured value listed in Table 9.6. Since I have used the larger of the two size estimates in Secs. 7.4 and 8, this may be an overestimate. Improved measurements of the size and mass of the platelet will be necessary for better comparisons of data and theory.

9.6.2 Rotationally induced magnetic moment

Returning to the data in Fig. 9.8, one can see that the minimum in the product $\nu_B \nu_0$ occurs around a drive frequency of $\nu_{min} = 2.87 \times 10^7$ Hz. I interpret this as the turning point between the diamagnetic and rotational regimes, where the contributions ω_{dia} and ω_{rot} are equal. Combining Eqs. 9.7 and 9.8 gives

$$\frac{\omega_{dia}^2}{\omega_{rot}^2} = \frac{B_0 \left|\alpha_{dia}\right|}{\omega_{min}\alpha_{rot}} = 1, \tag{9.16}$$

from which I obtain $\alpha_{rot} = 2.9 \times 10^{-27}$ J s T^{-1}.

Assuming that the magnetic dipole moment arises from rotation of the charge on the rotating nanoplatelet, the contribution from rotation, $\boldsymbol{\mu}_{rot}$, can be obtained from [102]:

$$\boldsymbol{\mu}_{rot} = \frac{\boldsymbol{\omega_n}}{2} \int da\, r^2 \sigma = \frac{q\boldsymbol{\omega_n} \int da\, r^2 \sigma}{2 \int da\, \sigma} = \frac{q\omega_n}{2} \left\langle r_q^2 \right\rangle \hat{\boldsymbol{n}}. \tag{9.17}$$

Here, the integrals are over the surface of the platelet, r is the distance from the axis of rotation, σ is the local charge density on the platelet surface, q is the total charge on the platelet and $\left\langle r_q^2 \right\rangle$ is the mean square size of the platelet weighted by

the charge density. Thus, $\alpha_{rot} = q\left\langle r_q^2 \right\rangle /2$ and

$$\omega_{rot} = \sqrt{\frac{\Omega^2 B_0 q \left\langle r_q^2 \right\rangle}{2 I_\perp \omega_n}}. \tag{9.18}$$

From the definition of the moment of inertia in Eq. 7.23, and letting $g \equiv \left\langle r_q^2 \right\rangle / \left\langle r_m^2 \right\rangle$, one can obtain an expression for ω_{rot}:

$$\omega_{rot} = \Omega \sqrt{\frac{g}{2\omega_n} \frac{qB_0}{m}}. \tag{9.19}$$

For the data shown in Fig. 9.8, $B_0 = 7$ mT, and thus $qB_0/m = 0.04$ rad sec^{-1}; also, at the turning point, $\omega_{rot} = 3.68$ rad sec^{-1}. Using Eq. 9.19, I obtain $g = 7.6$.

The g-factor that I have inferred from the data is substantially in excess of that which would be expected for a spinning plate with charge fixed on its surface. For a spinning circular disk with evenly distributed charge, $g = \left\langle r_q^2 \right\rangle / \left\langle r_m^2 \right\rangle = 4/3$. If *all* charge is located at the perimeter of a circular disc of uniform mass density, then $\left\langle r_q^2 \right\rangle / \left\langle r_m^2 \right\rangle = 2$. Thus, one expects $g \approx 1 - 2$.

I will now briefly discuss a possible explanation for the unexpectedly large g. A rotating material body can produce a magnetic field, even if it has no net electric charge. This phenomenon was discovered in 1935 by Samuel Barnett, who reasoned that if placing a ferromagnet in a magnetic field can cause it to rotate (the Einstein-de Haas effect), then the reverse should also be true. He derived the following relationship for a rotating solid object [103]:

$$B = \frac{\omega}{\gamma}, \tag{9.20}$$

where B is the emergent magnetic field produced by the rotating object, ω is the angular frequency of rotation, and γ is the gyromagnetic ratio of the object. Re-

cent studies have confirmed the Barnett effect in various materials [104][105]. For electrons of mass m_e and charge e, the effective magnetic field induced by rotation is

$$B_{rot} = \frac{m_e}{e}\omega_n, \tag{9.21}$$

which for $\nu_0 = \omega_n/(2\pi) = 30$ MHz is $B_{rot} = 1.1 \times 10^{-3}$ T. This field is quite comparable to that used in the experiments and is suggestive that the Barnett effect may be important. Revising the value for B_0 in Eq. 9.19 upward would bring the calculated g closer to the expected value.

The sensitivity of a measurement device may be loosely defined as the smallest increment it can detect in the measured quantity. The measurements of α_{dia} and α_{rot} listed in Table 9.6 give a sense of the magnitudes that can be measured in this apparatus. Evaluating the diamagnetic contribution to the magnetic moment gives:

$$\mu_{dia} = \alpha_{dia}B = (-8 \times 10^{-17}\ \mathrm{J\,T^{-2}}) \times (7 \times 10^{-3}\ \mathrm{T}), \tag{9.22}$$

suggesting a magnetic moment sensitivity of order 10^{-20} $\mathrm{J\,T^{-1}}$ or about 10^3 μ_B (where $\mu_B = 9.27 \times 10^{-24}$ $\mathrm{J\,T^{-1}}$). Similarly, evaluating the rotational contribution gives:

$$\mu_{rot} = \alpha_{rot}\omega_n = (3 \times 10^{-27}\ \mathrm{J\,s\,T^{-1}}) \times (2\pi \times 30 \times 10^6\ \mathrm{rad\,s^{-1}}), \tag{9.23}$$

suggesting a torque sensitivity of order 10^{-22} J, not far from $k_BT \approx 4 \times 10^{-21}$ J at 300 K. That torques smaller than the naive thermal limit are measurable is a consequence of the gyroscopic stabilization of the platelet in the experiments [58] and the low damping in the system.

Chapter 10: Conclusions

The overall goal of this thesis was to enable experiments on graphene nanoplatelets maximally decoupled from their environment. To this end, I have demonstrated a method of collecting a nanoplatelet in a quadrupole ion trap and transferring it to a second trap in a chamber that can be pumped down to UHV pressures. I have described a method of locking the rotation frequency of the trapped platelet to a radio frequency electric field and shown that the platelet reliably stays locked when the drive field frequency and amplitude are changed. Finally, I have observed two mechanisms of interaction of the platelet with an applied magnetic field; this data shows qualitative agreement with theory.

The collection and transfer system has shown good reliability. Collection of platelets large enough for convenient study (with estimated diameters on the order of 1 μm) has been reasonably efficient. With a clean system, the median time to collection of such a sample is roughly 15 minutes of electrospraying, with standard deviation 10 minutes. For this size of platelet, the transfer success rate at a pressure of 30 mTorr is nearly 100%, assuming proper alignment of the traps. Smaller platelets are more often lost during transfer; the reason for this is not yet understood, but may be related to the fact that smaller platelets typically have larger charge-to

mass ratios. I have succeeded in transferring platelets with charge-to-mass ratios ranging from 7 C/kg to 52 C/kg.

Further improvements to the transfer procedure may be possible. While desired experimental pressures are 10^{-8} Torr or lower, the current transfer procedure is reliably successful only at pressures of ∼10 mTorr and higher. Fine-tuning of the trap voltages and separation distances may enable transfer at lower pressures, although a limit will be imposed by the fact that the platelet tends to escape from the trap at pressures below ∼1 μTorr in the absence of feedback cooling (which cannot be used during transfer).

An area meriting further study is the graphene suspension recipe. Samples collected had typical thicknesses estimated at ∼10 layers or more, while the ideal platelet would be single-layer. It is possible that a different solvent mixture would achieve better exfoliation of the graphite.

Since platelets are detected purely optically, measurements of characteristics such as size, shape, and thickness must be performed indirectly and involve considerable uncertainty. Improvements in these measurements are necessary to further explore the extent of the agreement of the data with theory. Better mass measurements may be possible by observing discrete changes in the charge of the trapped platelet, as described in Sec. 2.5.1 and in Ref. [19]. Additionally, I and other lab members are developing a method of expelling the platelet from the trap and directing its trajectory onto a substrate where it can be characterized more precisely via conventional microscopy. Kuhlicke and colleagues have recently demonstrated success at a related task, that of depositing silica microspheres from a Paul trap

onto an optical fiber[106].

A final experimental challenge involves control over the charge on the platelets. For most platelets studied, I observe an approximately exponential decrease in the charge-to-mass ratio over the course of several days of exposure to high vacuum pressures. I attribute this to volatile charged molecules detaching from the platelet's surface due to laser heating. For most platelets, the charge number stabilizes after a few days. In future experiments, however, it could be useful to be able to control the amount of charge on the platelet, perhaps by bombarding it with an electron beam[107]. Preliminary experiments by Jacob Murphy and Caroline Horsch have demonstrated success with this technique[108].

Finally, I expect that the graphene suspensions can be replaced with any one of the wide variety of 2D materials that can be generated by liquid exfoliation[10]. In addition, the transfer technique could be used to deliver samples to environments inhospitable to the collection process: for example, to traps inside strong magnets for measurements in the quantum Hall regime.

Bibliography

[1] B. C. Brodie, Philosophical Transactions of the Royal Society of London **149**, 249 (1859). [Cited on page 1.]

[2] A. K. Geim, Physica Scripta **T149**, 014003 (2012). [Cited on page 1.]

[3] K. S. Novoselov *et al.*, Science **306**, 666 (2004). [Cited on page 1.]

[4] C. Lee, X. Wei, J. W. Kysar, and J. Hone, Science **321**, 385 (2008). [Cited on pages 2 and 3.]

[5] J. Zhang *et al.*, Physical Review Letters **104**, 166805 (2010). [Cited on pages 2 and 36.]

[6] C. Faugeras *et al.*, ACS Nano **4**, 1889 (2010). [Cited on page 2.]

[7] A. A. Balandin *et al.*, Nano Letters **8**, 902 (2008). [Cited on page 2.]

[8] *CRC Handbook of Chemistry and Physics 2003-2004*, edited by D. R. Lide (CRC Press, USA, 2003). [Cited on page 2.]

[9] J. H. Los, K. V. Zakharchenko, M. I. Katsnelson, and A. Fasolino, Physical Review B **91**, 045415 (2015). [Cited on page 2.]

[10] V. Nicolosi *et al.*, Science **340**, 1226419 (2013). [Cited on pages 2, 30, and 113.]

[11] S. Z. Butler *et al.*, ACS Nano **7**, 2898 (2013). [Cited on page 2.]

[12] J.-H. Chen *et al.*, Nature Nanotechnology **3**, 206 (2008). [Cited on page 3.]

[13] S. Shivaraman *et al.*, Nano Letters **9**, 3100 (2009). [Cited on page 3.]

[14] K. Matsui *et al.*, Micro and Nano Letters **11**, 670 (2009). [Cited on page 3.]

[15] J. P. Mathew *et al.*, Nature Nanotechnology **11**, 747 (2016). [Cited on page 3.]

[16] B. E. Kane, Physical Review B **82**, 115441 (2010). [Cited on pages 4, 5, 8, 16, 19, and 58.]

[17] L. Lindsay, D. A. Broido, and N. Mingo, Physical Review B **82**, 115427 (2010). [Cited on page 5.]

[18] E. V. Castro *et al.*, Physics Review Letters **105**, 266601 (2010). [Cited on page 5.]

[19] P. Nagornykh, Ph.D. thesis, University of Maryland, 2015. [Cited on pages 8, 24, 26, 29, 59, and 112.]

[20] P. Nagornykh, J. E. Coppock, and B. E. Kane, Applied Physics Letters **106**, 24 (2015). [Cited on pages 8, 19, 21, 24, 26, and 59.]

[21] L. D. Hinkle and B. R. F. Kendall, Journal of Vacuum Science and Technology A **10**, 243 (1992). [Cited on pages 9 and 26.]

[22] O. M. Morago *et al.*, ACS Nano **4**, 7515 (2010). [Cited on pages 9, 10, and 26.]

[23] T. Li and M. G. Raizen, Annalen der Physik **525**, 281 (2013). [Cited on page 9.]

[24] K. G. Libbrecht and E. D. Black, Physics Letters A **321**, 99 (2003). [Cited on page 9.]

[25] L. P. Neukirch and A. N. Vamivakas, Contemporary Physics **56**, 48 (2014). [Cited on page 9.]

[26] R. E. March, Journal of Mass Spectrometry **32**, 351 (1997). [Cited on page 9.]

[27] W. Paul, Reviews of Modern Physics **62**, 531 (1990). [Cited on pages 9 and 15.]

[28] Y. Cai *et al.*, Analytical Chemistry **74**, 232 (2002). [Cited on pages 9 and 36.]

[29] J. F. Spann, M. M. Abbas, C. C. Venturini, and R. H. Comfort, Physica Scripta **T89**, 147 (2001). [Cited on page 9.]

[30] C. E. Pearson *et al.*, Physical Review A **73**, 032307 (2006). [Cited on page 10.]

[31] R. Maiwald *et al.*, Nature Physics **5**, 551 (2009). [Cited on pages 10 and 15.]

[32] C. W. Twombly, J. S. Evans, and I. I. Smalyukh, Optics Express **21**, 1324 (2013). [Cited on page 10.]

[33] O. M. Marago *et al.*, Nature Nanotechnology **8**, 807 (2013). [Cited on page 10.]

[34] A. Ashkin, Physical Review Letters **24**, 156 (1970). [Cited on page 10.]

[35] A. Ashkin and J. M. Dziedzic, Applied Physics Letters **28**, 333 (1976). [Cited on page 10.]

[36] A. Ashkin, J. M. Dziedzic, J. E. Bjorkholm, and S. Chu, Optics Letters **11**, 288 (1986). [Cited on page 10.]

[37] R. Omori, T. Kobayashi, , and A. Suzuki, Optics Letters **22**, 816 (1997). [Cited on page 11.]

[38] V. Jain *et al.*, Physical Review Letters **116**, 243601 (2016). [Cited on page 11.]

[39] T. Li, S. Kheifets, and M. G. Raizen, Nature Physics **7**, 527 (2011). [Cited on page 11.]

[40] J. Gieseler, B. Deutsch, R. Quidant, and L. Novotny, Physical Review Letters **109**, 103603 (2012). [Cited on page 11.]

[41] J. Gieseler, M. Spasenović, L. Novotny, and R. Quidant, Physical Review Letters **112**, 103603 (2014). [Cited on page 11.]

[42] P. Mestres *et al.*, Applied Physics Letters **107**, 151102 (2015). [Cited on page 11.]

[43] J. Gieseler *et al.*, Nature Nanotechnology **9**, 358 (2014). [Cited on page 11.]

[44] L. Rondin *et al.*, Reports on Progress in Physics **77**, 056503 (2014). [Cited on pages 11 and 12.]

[45] L. P. Neukirch *et al.*, Optics Letters **38**, 2976 (2013). [Cited on page 12.]

[46] T. M. Hoang, J. Ahn, J. Bang, and T. Li, Nature Communications **7**, 12250 (2016). [Cited on page 12.]

[47] M. Geiselmann *et al.*, Nature Nanotechnology **8**, 175 (2013). [Cited on page 12.]

[48] M. Aspelmeyer, T. J. Kippenberg, and F. Marquardt, Reviews of Modern Physics **86**, 1391 (2014). [Cited on page 12.]

[49] P. Asenbaum *et al.*, Nature Communications **4**, 2743 (2013). [Cited on page 12.]

[50] S. Kuhn *et al.*, Nano Letters **15**, 5604 (2015). [Cited on page 12.]

[51] S. Kuhn *et al.*, Optica **4**, 356 (2017). [Cited on page 12.]

[52] T. S. Monteiro *et al.*, New Journal of Physics **15**, 015001 (2013). [Cited on page 12.]

[53] J. Millen, T. Deesuwan, P. Barker, and J. Anders, Nature Nanotechnology **9**, 425 (2014). [Cited on page 12.]

[54] J. Millen *et al.*, Physical Review Letters **114**, 123602 (2015). [Cited on page 12.]

[55] P. Fonseca *et al.*, Physical Review Letters **117**, 173602 (2016). [Cited on page 12.]

[56] G. Ranjit, M. Cunningham, K. Casey, and A. A. Geraci, Physical Review A **93**, 053801 (2016). [Cited on page 13.]

[57] T. M. Hoang *et al.*, Phys. Rev. Lett. **117**, 123604 (2016). [Cited on pages 13 and 73.]

[58] Y. Arita, M. Mazilu, and K. Dholakia, Nature Communications **4**, 2374 (2013). [Cited on pages 13 and 110.]

[59] J. E. Coppock *et al.*, Journal of the Optical Society of America B **34**, C36 (2017). [Cited on pages 14, 15, 30, 36, and 49.]

[60] P. Nagornykh, J. E. Coppock, J. P. J. Murphy, and B. Kane, Physical Review B **96**, 035402 (2017). [Cited on pages 14, 65, 84, and 90.]

[61] Waveform generator model: Agilent 33522A. [Cited on page 16.]

[62] Scaling amplifier model: Stanford Research Systems SIM983. [Cited on page 16.]

[63] High voltage amplifier model: Trek Model 2205. [Cited on pages 16 and 56.]

[64] CCD camera information: ProEM 512 (Model No. 7555-0002) thermoelectrically cooled ccd camera. Resolution 512x512 pixels. [Cited on page 22.]

[65] Photodetector information: Hamamatsu MPPC Module C13366-1350GD. The $\sim$20 ns pulses output by this unit are shortened to $\sim$1 ns to increase frequency response to $>$500 MHz. [Cited on page 22.]

[66] D. J. Berkeland *et al.*, Journal of Applied Physics **83**, 5025 (1998). [Cited on page 24.]

[67] A. Härter, A. Krükow, A. Brunner, and J. H. Denschlag, Applied Physics B **114**, 275 (2014). [Cited on page 24.]

[68] D. M. Bell, C. R. Howder, R. C. Johnson, and S. L. Anderson, ACS Nano **8**, 2387 (2014). [Cited on page 29.]

[69] M. Lotya *et al.*, ACS Nano **4**, 3611 (2010). [Cited on pages 30 and 33.]

[70] R. Narayan and S. O. Kim, Nano Convergence **2**, 20 (2015). [Cited on page 30.]

[71] Y. Hernandez *et al.*, Nature Nanotechnology **3**, 563 (2008). [Cited on page 33.]

[72] A. A. Green and M. C. Hersam, Nano Letters **9**, 4031 (2009). [Cited on page 33.]

[73] Commercially-produced graphene nanoplatelets: XG Sciences Product No. x-GnP M-5. [Cited on page 35.]

[74] Commercially-produced graphene nanoplatelets: CheapTubes Grade 4 (Research) Graphene Nanoplatelets. [Cited on page 35.]

[75] M. Yamashita and J. B. Fenn, Journal of Physical Chemistry **88**, 4451 (1984). [Cited on page 36.]

[76] J. B. Fenn, Angewandte Chemie International Edition **42**, 3871 (2003). [Cited on page 36.]

[77] G. M. H. Meesters, P. H. W. Vercoulen, J. C. M. Marijnissen, and B. Scarlett, Journal of Aerosol Science **3**, 37 (1991). [Cited on page 36.]

[78] X. Zhang *et al.*, Journal of Physics D: Applied Physics **46**, 055308 (2013). [Cited on page 36.]

[79] Syringe pump model: Chemyx NanoJet. [Cited on page 41.]

[80] Electrospray emitter needle information: PicoTip TaperTip Emitter, No. MT320-100-3.5-5. [Cited on page 41.]

[81] Pinhole diaphragm information: National Aperture, Standard Round Aperture, No. 1-75. [Cited on page 41.]

[82] Electrospray power supply model: Keithley 247 High Voltage Supply. [Cited on page 42.]

[83] Front chamber photodetector information: Hamamatsu MPPC Module C12661-150. Photon detection efficiency is 35% at 532 nm. [Cited on page 45.]

[84] Silica nanosphere information: www.microspheres-nanospheres.com, Product No. 147070-10. [Cited on page 46.]

[85] Linear translation mechanism information: uhvdesign.com, LSM38-300-H. [Cited on page 51.]

[86] Servo motor model: Teknic, CPM-MCPV-34320-ECN-1-0-1. [Cited on page 51.]

[87] Planetary gear model: Parker Hannifin Co., PX34-010-82. [Cited on page 51.]

[88] He gas source: Matheson Ultra High Purity Helium Gas. [Cited on page 51.]

[89] R. A. Beth, Physical Review **50**, 115 (1936). [Cited on page 58.]

[90] A. I. Bishop, T. A. Nieminen, N. R. Heckenberg, and H. Rubinsztein-Dunlop, Physical Review **92**, 198104 (2004). [Cited on page 58.]

[91] E. M. Purcell, The Astrophysical Journal **231**, 404 (1979). [Cited on page 70.]

[92] H. R. Gordon, Optics Express **15**, 5572 (2007). [Cited on pages 74 and 86.]

[93] Lock-in amplifier model: Zurich Instruments UHFLI, www.zhinst.com. [Cited on page 82.]

[94] R. Schiffer and K. O. Thielheim, Journal of Applied Physics **50**, 2476 (1979). [Cited on page 86.]

[95] D. M. LeVine, R. Meneghini, R. H. Lang, and S. S. Seker, Journal of the Optical Society of America **73**, 1255 (1983). [Cited on page 86.]

[96] J. A. Finnigan and D. J. Jacobs, Journal of Physics D: Applied Physics **4**, 72 (1971). [Cited on page 86.]

[97] Y. Ominato and M. Koshino, Physical Review B **87**, 115433 (2013). [Cited on page 100.]

[98] C. Uyeda, T. Komatsu, M. Sakakibara, and H. Chihara, Journal of the Physical Society of Japan **70**, 1226 (2001). [Cited on pages 100 and 101.]

[99] M. Sepioni *et al.*, Phys. Rev. Lett. **105**, 207205 (2010). [Cited on page 101.]

[100] M. Koshino, Y. Arimura, and T. Ando, Physical Review Letters **102**, 177203 (2009). [Cited on page 107.]

[101] E. Arvas and R. Harrington, IEEE Transactions on Antennas and Propagation **AP-31**, 719 (1983). [Cited on page 107.]

[102] J. D. Jackson, *Classical Electrodynamics*, 3rd ed. (Wiley, New York, 1999), p. 186. [Cited on page 108.]

[103] S. J. Barnett, Reviews of Modern Physics **7**, 129 (1935). [Cited on page 109.]

[104] H. Chudo *et al.*, Applied Physics Express **7**, 063004 (2014). [Cited on page 110.]

[105] M. Ono *et al.*, Physical Review B **92**, 174424 (2015). [Cited on page 110.]

[106] A. Kuhlicke, A. Rylke, and O. Benson, Nano Letters **15**, 1993 (2015). [Cited on page 113.]

[107] S. Schlemmer *et al.*, Applied Physics A **78**, 629 (2004). [Cited on page 113.]

[108] Jacob Murphy and Caroline Horsch, personal communication (2017). [Cited on page 113.]